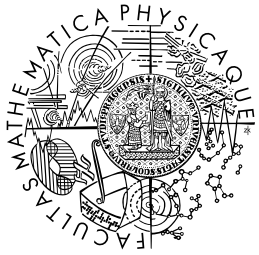

FACULTY
OF MATHEMATICS
AND PHYSICS
Charles University

DOCTORAL THESIS

Camille Landri

Theory and observations of two stars undergoing strong interaction

Institute of Theoretical Physics

Supervisor of the doctoral thesis: doc. Mgr. Ondřej Pejcha, Ph.D.

Study programme: Theoretical Physics, Astronomy and Astrophysics

Study branch: P4F1A

Prague 2024

I declare that I carried out this doctoral thesis independently, and only with the cited sources, literature and other professional sources. It has not been used to obtain another or the same degree.

I understand that my work relates to the rights and obligations under the Act No. 121/2000 Sb., the Copyright Act, as amended, in particular the fact that the Charles University has the right to conclude a license agreement on the use of this work as a school work pursuant to Section 60 subsection 1 of the Copyright Act.

In ..... date ....

Author's signature

To Anthony, my stellar companion

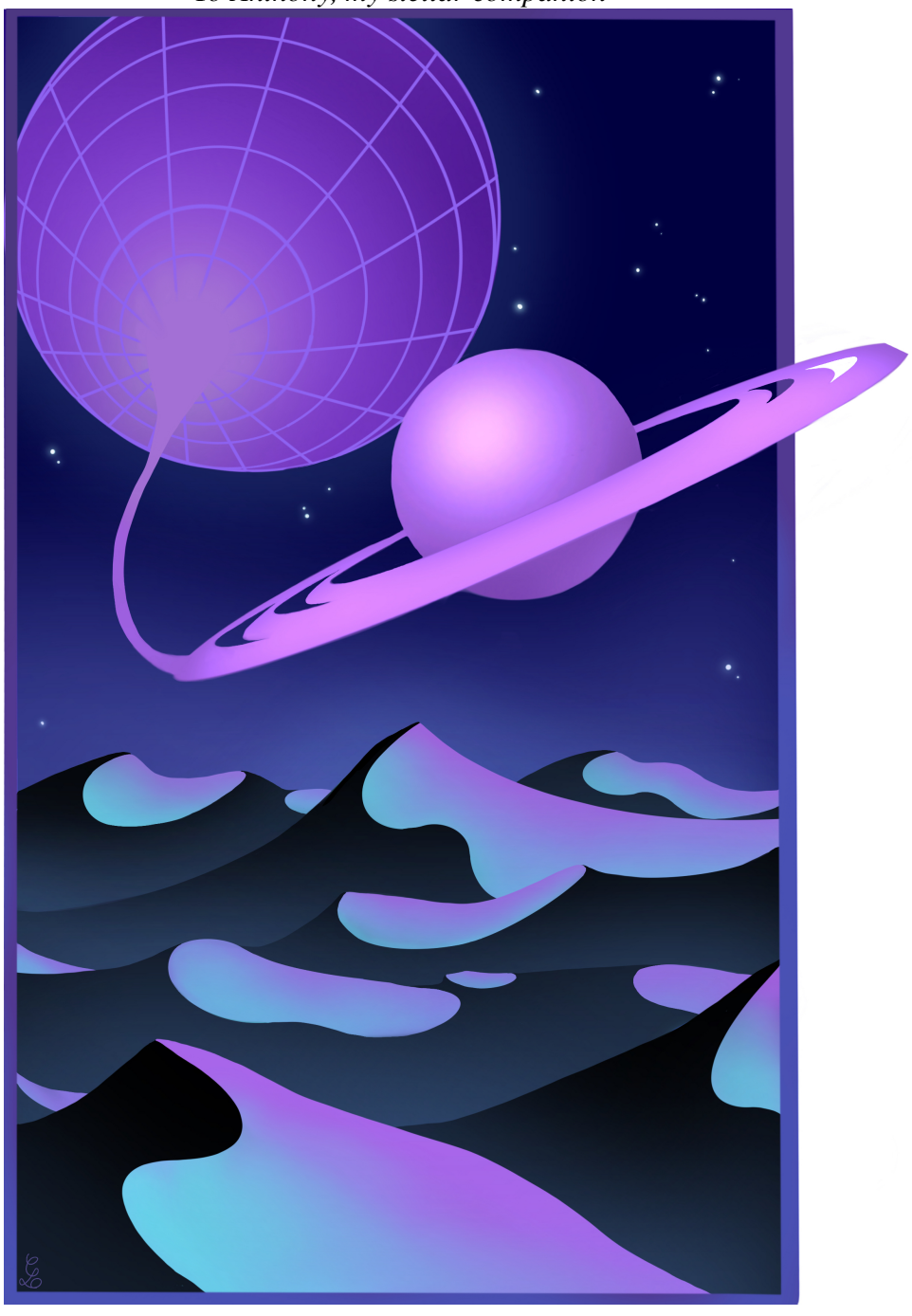

Acknowledgments

Well, this has been quite the journey. These past four years have been hard but rewarding, on many different levels, and I am glad to conclude my studies with this thesis. This work would not have been possible without the support of many people, both inside and outside of academia, and while it is not possible to thank all of them here, I would still like to underline the most important ones.

First, I'd like to thank my supervisor Ondřej, for his guidance and inspiring enthusiasm for transients, which helped me figure out how to become a good astrophysicist. I am also grateful for the support from Charles University and the Institute of Theoretical Physics.

I want to thank everyone who has served as a mentor over the past four years. Paul, for his support and patience, especially during my (rather painful) discovery of grid-based methods. Diego and Damien, for their numerous advice on hydrodynamics methods, endless discussions on the most random topics, and, maybe more importantly, their support in challenging times. I also wish to thank everyone involved in the MPA Kavli Summer Program 2023, the organisers, the advisers, and all the amazing students I met there, as they all immensely contributed to renewing my motivation to pursue a scientific career. I am grateful for my colleagues and all the fellow PhD students I have met, both at my university and abroad, and for the inspiring conversations we had.

J'aimerais, évidemment, remercier ma famille. Mes frères et soeurs, Margaux, Liam, Gabrielle et Jolan, pour leur soutien inconditionnel. Merci a mon père, de continuer a me transmettre ses passions et sa tenacité, et ma mère, de m'inspirer avec son sens de la pédagogie et sa curiosité sans fin. A mon oncle et mon grand-père, a qui j'aurais aimé montrer ce travail avec fierté.

I also wish to thank all my friends for their support at any stage of my life and studies. To Michael, Dany, JF, Val, and many others. But I cannot mention my friends without mentioning Ana. Of all the things I thought I would gain during this PhD, I certainly didn't think I'd gain the most amazing friendship. To this date, I still don't know if they put us in the same dorm room on purpose, but I am so glad they did. I don't think finishing this PhD would have been possible without her and her support, the endless discussions in the middle of the night, and the billion coffees we drank while listening to each other's problems. Thank you, Ana, for being the best friend I could ask for. I look forward to calling you Doctor.

Finally, and most importantly, I am incredibly grateful for my partner, Anthony. I owe them this thesis, as they were the one to push me to take this position despite knowing we would have to live apart for four years. I owe them the little confidence I have, always cheering me on and forcing me to listen to the things I don't want to hear. I owe them the person and scientist I am becoming, thanks to their unconditional acceptance while being unapologetically themself. I dedicate this work to you, my stellar companion. I owe everything to your love and support.

Title: Theory and observations of two stars undergoing strong interaction

Author: Camille Landri

Department: Institute of Theoretical Physics

Supervisor: doc. Mgr. Ondřej Pejcha, Ph.D., Institute of Theoretical Physics

Abstract: Stars, especially massive ones, are commonly found in binary systems with such low separations that the stars are close enough to interact with each other through tidal forces and phases of mass transfer. Binary interactions shape the evolution of numerous stellar systems, producing a variety of exotic stellar objects as well as various transients arising from accretion or stellar evolution. This thesis aims to investigate different types of stellar interactions to constrain new and existing models.
For the first part of this work, we conducted a thorough analysis of the observations of the peculiar cataclysmic variable OGLE-BLG504.12.201843, which exhibits year-long outbursts recurring on average every 973 days. We show that these peculiar outbursts come from an unstable accretion disc, potentially classifying this object as an extreme dwarf nova, which challenges the current knowledge of similar systems.
Secondly, we explore a new scenario in which binary interaction can drive asymmetric winds in red supergiant stars. By performing 3D hydrodynamics simulations of a companion repeatedly grazing the outer envelope of a red supergiant, we show that this scenario allows the formation of dust-driven winds carrying a total of $0.185\,M_{\odot}$ and ends with the two stars entering common envelope evolution.
Finally, we investigate the impact of previous phases of mass transfer on the outcome of common envelope evolution in the case of progenitor systems of double neutron star binaries. We carried out 3D hydrodynamics simulations of common envelope evolution that took into account the effect of mass transfer on the stellar structure of the donor, which shows that the inspiral phase is hastened, the ejected envelope is more asymmetrical, and the amount of ejected mass is reduced.

Keywords: binary stars, stellar evolution, cataclysmic variables, red supergiants, hydrodynamics, photometry, spectroscopy

Contents

[1]This chapter is a pre-copyedited, author-produced version of an article accepted for publication in Monthly Notices of the Royal Astronomical Society following peer review. The version of record [Camille Landri, Onděj Pejcha, Michal Pawlak, Andrzej Udalski, Jose L. Prieto, Manuel Barrientos, Jay Strader and Subo Dong. OGLE-BLG504.12.201843: a possible extreme dwarf nova. MNRAS Volume 517, Issue 2, December 2022, Pages 2746–2756] is available online at https://doi.org/10.1093/mnras/stac2864

[2]This chapter is a pre-copyedited, author-produced version of an article accepted for publication in Monthly Notices of the Royal Astronomical Society following peer review. The version of record [Camille Landri, Ondřej Pejcha. Driving asymmetric red supergiants winds with binary interactions. MNRAS, Volume 531, Issue 3, July 2024, Pages 3391–3405] is available online at https://doi.org/10.1093/mnras/stae1379.

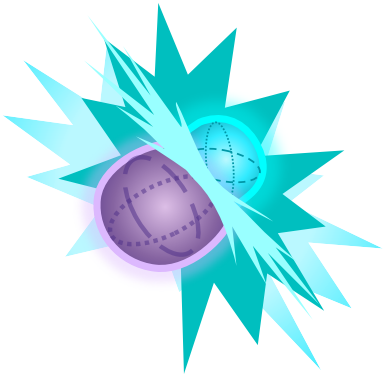

1. Introduction

Contrary to the common perception of stellar evolution, stars do not necessarily evolve in isolation. Many stars are found in clusters or associations, in which they are gravitationally bound to one or more companions. Alternatively, a large fraction of stars evolve within "multiple systems", which can range from binary systems containing two stars to triple or more complex hierarchical arrangements. Such systems can either form through the fragmentation of the same molecular cloud during star formation, yielding tightly bound multiple systems, or through gravitational capture in relatively dense stellar environments.

Several decades of observation show that stars commonly evolve in binary systems (Moe & Di Stefano, 2017). In particular, close binary systems with separation $\lesssim 1$ AU often undergo evolutionary phases during which the two stars interact through tidal forces or mass transfer. Such interactions are expected to significantly affect the evolution of both the binary system and the stars and appear to be especially frequent in binaries composed of one or more massive stars (e.g., Abt et al., 1990; Sana et al., 2012). By altering stellar evolution, binary interactions produce a wide variety of exotic stellar objects, such as stripped stars (Shenar et al., 2020; Drout et al., 2023) or merger products (Schneider et al., 2019; Hirai et al., 2021). They may also result in degenerate binaries containing at least one compact object (white dwarf, neutron star, or black hole), which can produce various astrophysical transients due to accretion processes (e.g., cataclysmic variables, X-ray binaries), exotic supernovae (Chevalier, 2012; Metzger, 2022), or gravitational waves in the case of double degenerate binaries Tauris et al. (2017). Thus, close binaries follow different evolutionary paths that lead to many well-documented astrophysical phenomena, and the study of stellar interactions is extremely important to understand the conditions under which these transients arise.

1.1 Binary system

A binary system consists of two stars orbiting around their common centre of mass. The most straightforward approach to describing a binary orbit is to consider the two stars as point masses that only interact through the gravitational force. The motion of the two stars then obeys Kepler's first law and can be described with two ellipses of semi-major axes a_1 and a_2, the same eccentricity e and a common focal point centred around the centre of mass of the binary, the so-called barycentre. In the rest frame of one of the stars, the companion's motion draws an ellipse of eccentricity $a = a_1 + a_2$, eccentricity e, and one focus centred around the static star. The distance r between the

two stars is given by:

$$r(\theta) = \frac{a(1-e^2)}{1+e\cos\theta}, \tag{1.1}$$

where θ is the true anomaly, the angle between the position of the star and its position of closest approach (the periastron). The orbital period of the system $P_{\rm orb}$ is then related to a and the mass of the stars M_1 and M_2 according to Kepler's third law:

$$\frac{a^3}{P_{\rm orb}^2} = \frac{G(M_1+M_2)}{4\pi^2}, \tag{1.2}$$

where G is the gravitational constant. Thus, the dynamics of binaries are tightly related to the mass of their components, and it is possible to constrain the nature of the two stars using their orbital parameters.

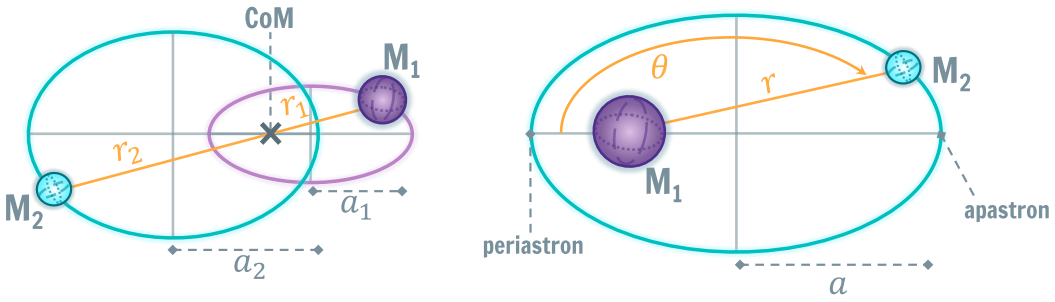

Figure 1.1: Illustration of the orbital motion of a pair of stars with masses M_1 and M_2. Left: Binary orbit in the reference frame of the observer, the centre of mass is indicated with a cross. Right: Binary orbit in the rest frame of the star of mass M_1.

To determine the orbital and stellar parameters of a binary, it is necessary to resolve the time evolution of the system through repeated observations. Since binary systems exist in a broad range of configurations, different observational methods may be more or less adapted to each specific case, which leads to a natural classification of binaries based on their observability:

1. Visual binary: the orbital motion of the two stars is sufficiently wide to be spatially resolved by a telescope. After enough measurements, one can obtain the projection of the stars' orbits onto the celestial sphere, from which one can deduce the masses of the stars.

2. Astrometric binary: a special case of visual binaries where one of the stars is too faint to be observed or outshined by its companion. The brighter star appears to orbit empty space, but the motion of the two stars can be derived using precise astrometric measurements.

3. Spectroscopic binary: the orbit is too small to be resolved visually, but the high orbital velocities of the stars are measurable in their spectra. Except in cases where the orbital plane is perpendicular to the observer's line of sight, the motion of each star has a radial component, which translates into periodic Doppler shifts in their spectral lines.

4. Eclipsing binary: the system inclination is such that the two stars obscure one another during their orbit. The periodic decreases in brightness due to the eclipses can be observed through photometric measurements, and allow to constrain the orbital properties of the binary. In particular, the shape of the eclipse in the light curve also yields constraints on the relative size of the two stars and the ratio of their surface brightness.

Of course, some binary systems can be observed using multiple methods, in which case the orbital parameters of the system can be more accurately derived. It is, for example, relatively frequent for spectroscopic binaries to also show eclipses.

While most stars in wide binaries are expected to evolve in similar ways to isolated stars, this is not necessarily true for stars in close binary systems, which have separation $\lesssim 1$ AU. For stars with stellar radii of magnitude comparable to the binary separation, Kepler's laws (equation 2.3) do not hold anymore. For instance, the significant tidal forces in such systems may cause the precession of the axis defined by the periastron and apastron (apsidal precession), or of the spin axis of a star if it is misaligned with the orbital rotation (axial precession). Close binaries are also expected to experience phases of mass transfer, which drastically influence the stars. Thus, the point mass approximation does not hold for close binary stars: they can no longer be estimated as spherically symmetric, and the whole geometry and structure of the stars must be accounted for.

1.1.1 Tidal interactions

Since the gravitational force varies with the distance to the attracting body, the gravitational pull on a star exerted by its companion does not have the same strength across the body of the star. This is particularly important for stars in close orbits, as the tidal force from this gravitational gradient can significantly deform the stellar surface. The part of the star that is closest to the companion experiences the strongest pull, so the star elongates along the star-companion axis to reach its gravitational equilibrium shape and forms so-called "tidal bulges". Since the star is distorted along one direction only, the phase lag between the bulge and the rotation of the star results in variations in the observed shape according to the orbital phase of the binary. When the elongated star has its longest axis perpendicular to the line of sight, it has a larger projected area, and the received photometric flux from the star is higher. On the other hand, the star appears smaller and dimmer when its elongation is aligned with the line of sight. Therefore, the photometric flux of the binary is at its maximum when the elongated star is observed "side on", while it shows minima when it is observed "face on". This effect, which we illustrate in Fig. 1.2, is called "ellipsoidal variability" and results in sinusoidal modulations of the observed flux of the binary.

The deformation of the star has several other effects. The gravitational equilibrium shape of the distorted star constantly changes as it progresses in its orbits, and the star must continuously rearrange. This adjustment cannot be instantaneous since the star is not fully elastic, resulting in frequent misalignment between the tidal bulge and the star-companion axis. The companion then exerts a net torque on the displaced bulges, causing the rotational angular velocity of the star to slowly increase (or decrease if the star was rotating faster than it was orbiting its companion) until it matches the orbital angular velocity of the binary. The star then orbits its companion with the same side facing the barycentre, and the tidal bulge remains aligned with the star-companion axis.

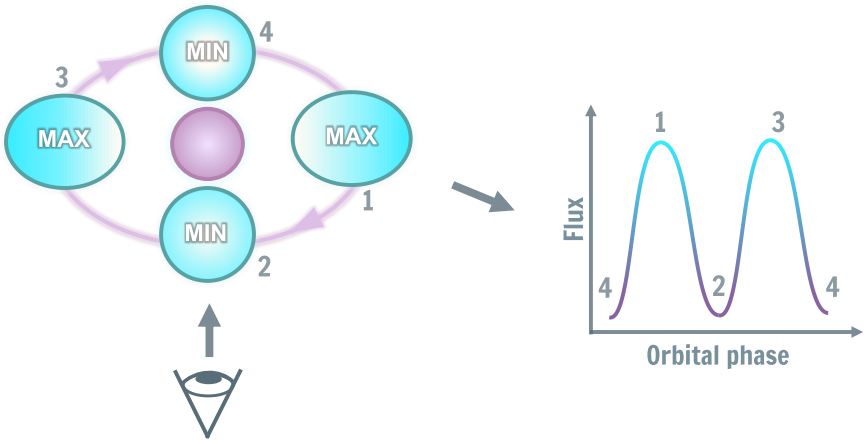

Figure 1.2: Illustration of the effect of tidal distortion of a star in a binary system. Left: Shape of the tidally distorted secondary depending on the orbital phase of the system. The elongation of the star is apparent when observed side-on but inconsequential when viewed from the front or back. Right: Ellipsoidal variations in the system's flux due to the distortion of the star. The minima corresponds to when the distorted star is seen from its front or back, and the maxima when it is observed side-on.

Additionally, the orbit of the binary has to widen or shrink according to the loss or gain of rotational angular momentum of the distorted star to conserve the system's total angular momentum.

If the binary system has an eccentric orbit, the orbital and rotational velocities of the star can only be synchronised on average. Due to this eccentricity, the orbital angular velocity of the system is not constant: it is slower at the apastron of the orbit (point of furthest binary separation) and gets faster as it approaches the periastron. Therefore, stellar rotation cannot be continuously synchronous with the orbit, leading to frequent lags between the orbital and rotational velocities of the star. Around the apastron, the torque on the non-spherical star will slow down its rotation but increase its orbital angular velocity, which reduces the eccentricity but widens the periastron distance. The opposite effect applies when the binary is at periastron, effectively decreasing the apastron distance and further circularising the orbit. Similarly, a deformed star with a misalignment between its spin axis and orbital rotation axis experiences gravitational torques that may bring it to co-planar rotation.

The timescales of tidal effects are strongly dependent on the ratio between the size of the orbit and the stellar radii, as well as the nature of the stellar envelope of the two stars (Zahn, 1977). Turbulent friction in convective regions of stars is by far the most efficient source of tidal friction and thus drives the tidal interaction in close binaries. For stars with significantly convective envelopes, such as low-mass main sequence (MS) stars or post-MS stars (e.g., red giants, AGB stars, and red supergiants), the circularisation timescale of the binary is highly dependent on the ratio of the semi-major axis to the stellar radius:

$$\tau_{\rm circ} \simeq \frac{1}{1.7f}\left(\frac{T_{1,\rm eff}}{4500\ \rm K}\right)^{-4/3}\left(\frac{M_{1,\rm env}}{M_\odot}\right)^{-2/3}\frac{M_1}{M_\odot}\frac{M_1}{M_2}\frac{M_1}{M_1+M_2}\left(\frac{a}{R_1}\right)^8 \rm yr, \tag{1.3}$$

where $T_{\rm eff}$ is the effective temperature of the distorted star of mass M_1 and radius R_1, $M_{1,\rm env}$ is its envelope mass, M_2 is the mass of the companion, a is the separation of the binary, and f is a dimensionless parameter that depends on the convective and

viscous processes and is of the order of unity. On the other hand, some stars have a radiative envelope and convection only occurs in their core, such as massive MS stars. In this case, the radius dependence of the circularisation timescale increases and can be approximated with:

$$\tau_{\rm circ} \propto (a/R_1)^{13/2}(R_1/R_{\rm core})^7, \tag{1.4}$$

where $R_{\rm core}$ is the radius of the core.

1.1.2 Mass transfer

Let's consider a test particle orbiting a binary system composed of two stars of masses M_1 and M_2 separated by a distance a. Assuming the binary has reached circular and synchronous rotation, and neglecting the Coriolis force, the forces exerted on the particle can be estimated in the co-rotating frame of the binary using the Roche potential:

$$\Phi_R(\vec{r}) = -\frac{GM_1}{|\vec{r}-\vec{r_1}|} - \frac{GM_2}{|\vec{r}-\vec{r_2}|} - \frac{|\vec{\omega}\times\vec{r}|^2}{2}, \tag{1.5}$$

where the first two terms are the gravitational potential from the two stars, and the third term is due to the centrifugal force appearing in the rotating frame. Here, $\vec{r_1}$ and $\vec{r_2}$ describe the position of the centres of mass of the stars, $\vec{r}$ is the distance between the particle and the rotation axis of the binary, and ω is its orbital angular velocity of the binary:

$$\vec{\omega} \equiv \frac{2\pi}{P_{\rm orb}}\hat{n} = \sqrt{\frac{G\,(M_1+M_2)}{a^3}}\hat{n}, \tag{1.6}$$

where $\hat{n}$ is a unit vector perpendicular to the orbital plane. To determine how the test particle behaves around the binary, one can find the surfaces of constant Φ_R by scaling all the variables in equation 1.5 in terms of total mass $M_1 + M_2$ and separation a. The shape of the Roche equipotentials only depends on the mass ratio of the binary $q = M_1/M_2$, but their scale relative to the size of the stars is determined by the binary separation. We show an example of the Roche geometry for $q = 3$ in Fig 1.3, where we can distinguish different equipotential shapes depending on the distance to the binary. Far from the system, the equipotentials draw a simple closed surface encompassing both stars. Closer to the binary, the equipotentials become more complicated and draw two regions of maximum potential on each side of the binary, while the potential describes a peanut-shaped region when the particle gets closer to the two stars. At a critical value of Φ_R, the equipotential draws two tear-drop lobes centred around each star, called Roche lobes, which connect through one point along the axis connecting the two stars. Inside these two regions, the equipotentials draw closed surfaces around each star.

The Roche geometry also describes five points of null Roche potential gradient, the Lagrange points, which are saddle points where the gravitational forces balance the centrifugal force. The first Lagrange point, L1, is found at the intersection of the two Roche lobes, L2 and L3 are positioned along the axis connecting the two stars, on each side of the binary, and L4 and L5 are found on each side of the axis connecting the two stars.

For binary systems, the regions of greatest interest in the Roche geometry are those described by the Roche lobes. The motion of the gas inside each Roche lobe is

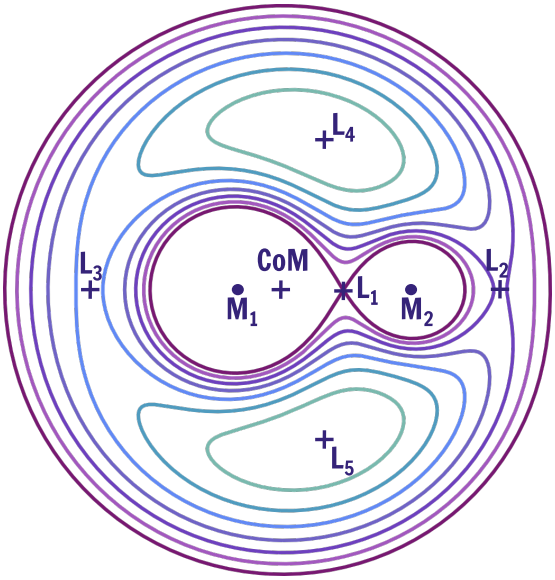

Figure 1.3: Roche equipotential in the orbital plane of a binary system with stars of mass M_1 and M_2 such that the mass ratio is $q = 3$. The colour gradient represents different values of the Roche potential Φ_R, from small values ($\Phi_R \gg 0$) in dark purple to values close to 0 ($\Phi_R \lesssim 0$) in light blue.

dominated by the gravitational potential of the star at the centre of the lobe, but if a parcel of gas approaches the critical surface, it may leave its Roche lobe. In particular, matter approaching the L1 point may flow from one lobe to the other instead of leaving the inner region. Therefore, if matter from a star in a binary somehow reaches the surface of the Roche lobe, it is generally predicted that the system will undergo a phase of mass transfer.

Roche lobe overflow

A star can overfill its Roche lobe when it expands during its evolution or if the orbit of the binary shrinks as it loses angular momentum. Stars generally evolve while maintaining their hydrostatic equilibrium: the inward gravitational force is balanced by the outward pressure gradient, such that surfaces of constant potential match surfaces of constant pressure and the stellar surface always coincides with an equipotential surface. Similarly, a star in hydrostatic equilibrium in a binary system has a stellar surface coinciding with a Roche equipotential. However, hydrostatic equilibrium cannot be maintained once the stellar surface reaches the equipotential defining its Roche lobe, as the equipotential surface around L1 allows matter to leave its current lobe and flow to the adjacent one. At this point, matter from the overflowing star (the donor) flows through the L1 point to the second Roche lobe and may be accreted by the second star (the accretor). This mechanism of mass transfer is known as Roche lobe overflow (RLOF).

To estimate whether a star is under or overfilling its Roche lobe, one can compare the volume of the star and its Roche lobe. For simplicity, the volume of the Roche lobe is often estimated using a sphere of equivalent volume defined by a Roche lobe radius R_L, which can be empirically fitted to the real Roche lobe volume. There exist several methods to determine R_L depending on the mass ratio of the system, though the

most common, and the one used in this thesis, was derived by Eggleton (1983a) and is accurate to a least 1% for any mass ratio:

$$R_{L,1} = \frac{0.49a}{0.6 + q^{-2/3} \ln\left(1 + q^{1/3}\right)} \quad \text{or} \quad q \equiv \frac{M_1}{M_2}. \tag{1.7}$$

Thus, mass transfer through RLOF is mostly relevant for close binaries where the size of the Roche Lobe and the stellar radii are comparable. One can classify binaries according to their tendency to undergo RLOF, distinguishing three types of systems (Kuiper, 1941; Kopal, 1955):

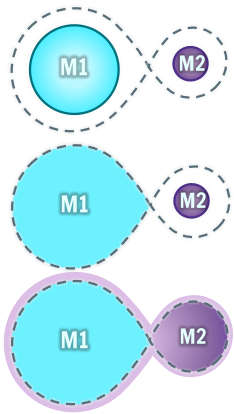

- Detached binaries: Both stars underfill their Roche lobes ($R_1 \ll R_{L,1}, R_2 \ll R_{L,2}$)
- Semi-detached binaries: One star fills its Roche lobe while its companion remains inside its Roche Lobe ($R_1 \gtrsim R_{L,1}, R_2 \ll R_{L,2}$)
- Contact binaries: Both stars fill their Roche lobe and share an envelope ($R_1 \gtrsim R_{L,1}, R_2 \gtrsim R_{L,2}$)

As it was derived here, mass transfer through RLOF is a fairly idealised process: it can conserve mass and momentum and requires that the orbit has been tidally synchronised and circularised. In reality, it is unlikely to be an exactly conservative process, and one should expect mass and angular momentum loss during mass transfer. For instance, it is possible for the transferred mass to not be fully accreted by the second star and leave the second Roche lobe (e.g., Lu et al., 2023): it may be re-emitted through isotropic winds or a spiral stream flowing out of the system through the vicinity of the L2 point.

The donor might also exhibit stellar winds, which can drive the mass transfer process. If the winds are fast enough to escape the potential of the binary, part of these winds can be accreted by the companion through wind-fed accretion (Bondi-Hoyle-Lyttleton accretion). This process is generally inefficient at transferring mass: much of the wind escapes the system without being accreted by the secondary star, also leading to considerable losses of angular momentum. On the other hand, some stellar winds are not fast enough to escape the potential of the binary and stay mostly confined within the Roche lobe of the donor. In such cases, the wind is focused towards the orbital plane of the binary and beamed towards the companion (Mohamed & Podsiadlowski, 2007), transferring matter to the secondary through the L1 point. This mechanism, which we illustrate along with regular RLOF in Fig 1.4, is called wind-RLOF and is mostly relevant for binaries containing AGB stars, which drive slow and dense dusty winds, especially when the binary separation is too large for regular RLOF to be efficient.

1.2 Evolution of close binaries

Tidal interactions and phases of mass transfer both have a significant impact on the evolution of close binaries. Tidal interactions mostly affect the orbital evolution of the system, as they tend to synchronise the stellar rotation with the orbit and circularise

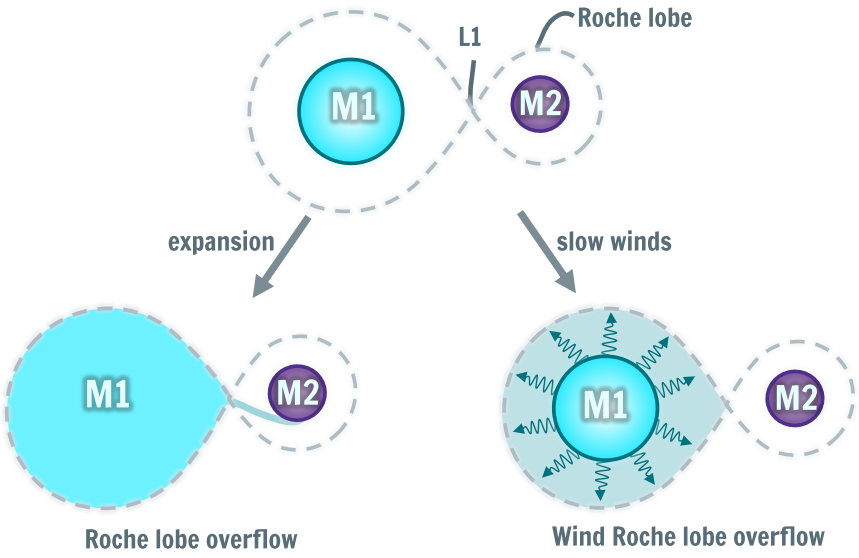

Figure 1.4: Main processes through which mass can be transferred from one Roche lobe to the other through the L1 point. Left: RLOF, the donor star fills its Roche lobe through evolutionary processes. Right: Wind-RLOF, the slow winds of the donor fill its Roche lobe and are focused on the orbital plane and beamed towards the accreting star.

eccentric orbits. However, tidal synchronisation may impose high stellar rotation, which can mix the envelope layers and reduce the chemical gradient inside the rotating star, thus impacting its evolution. In cases of extreme mixing, the star may evolve as approximately chemically homogeneous, with no distinction between the core and the envelope, and contract as it burns Hydrogen across its whole interior. Such stars experience a different evolution than a single star of the same mass and are more compact, hotter, and more luminous (Maeder, 1987). On the other hand, mass transfer is known to strongly impact both the orbital and stellar evolution of the binary. The effect of mass transfer strongly depends on the stability of the process as well as the phase of stellar evolution of the affected stars. Additionally, the ensuing accretion by the companion star is expected to affect the structure of the accretor and often involve accretion discs, which are common sources of astrophysical transients.

1.2.1 Mass transfer stability

The stability of mass transfer through RLOF depends on the evolution of the radius of the donor R_d and its Roche lobe radius R_L throughout the phase. While it becomes much more complicated for non-conservative mass transfer, one can derive standard stability criteria for RLOF by comparing the change in R_d and R_L during mass transfer. We can parameterise the reaction of R_L to the mass loss through:

$$\zeta_{\rm L} \equiv \frac{d \log R_{\rm L}}{d \log M_d}, \tag{1.8}$$

so that $\zeta_{\rm L}$ is positive for a shrinking Roche lobe. $\zeta_{\rm L}$ is only dependent on changes in the binary separation a and mass ratio q, which are described by the orbital evolution

of the system:

$$2\frac{\dot{J}}{J} = \frac{\dot{a}}{a} + 2\frac{\dot{M}_1}{M_1} + 2\frac{\dot{M}_2}{M_2} - \frac{\dot{M}_1 + \dot{M}_2}{M_1 + M_2} - \frac{2e\dot{e}}{1 - e^2}, \tag{1.9}$$

here J is the angular momentum of the binary, and we have neglected the spin of the stars. In the case of conservative mass transfer, we set $\dot{J} = 0$ and $\dot{M}_a = -\dot{M}_d$, and the orbital evolution is described with:

$$\frac{\dot{a}}{a} = 2\left(\frac{M_\mathrm{d}}{M_\mathrm{a}} - 1\right)\frac{\dot{M}_\mathrm{d}}{M_\mathrm{d}}. \tag{1.10}$$

Using a simplified formulation of equation 2.4 we can derive:

$$\zeta_\mathrm{L} = 2.13q - 1.67, \quad \text{for } R_\mathrm{L} \approx 0.44a\frac{q^{0.33}}{(1+q)^{0.2}} \tag{1.11}$$

for $q = M_\mathrm{d}/M_\mathrm{a} < 10$. Therefore, the change in R_L during RLOF can be reduced to a mass ratio dependence, and the Roche lobe generally shrinks for mass ratios above unity. Of course, this simplification does not apply to non-conservative mass transfer, where equation 1.9 and ζ_L become more complicated functions of the mechanisms of mass and angular momentum loss. Estimating the change in donor radius R_d requires a more careful approach because it is dictated by the response of the donor to the perturbation of its equilibrium. The mass loss during RLOF perturbs the hydrostatic equilibrium (HE) of the donor, which then adjusts its structure over its dynamical timescale τ_dyn. This timescale is generally much shorter than the timescale over which the star undergoes thermal readjustments, so the donor should recover its HE without significantly changing its thermal structure. The response of the donor to the perturbation of its HE can thus be approximated as adiabatic (e.g., Soberman et al., 1997) and be defined as:

$$\zeta_\mathrm{ad} \equiv \left(\frac{d\log R}{d\log M}\right)_\mathrm{ad}. \tag{1.12}$$

ζ_ad mostly depends on the structure of the donor, particularly on the dominant mechanism of energy transport in the envelope. As mass transfer suddenly removes the outer layers of the envelope, the layers underneath are decompressed and expand adiabatically to reach HE. Convective envelopes, by definition, have a nearly adiabatic structure, so the expansion of the uncovered layer is expected to increase the radius of the donor (Hjellming & Webbink, 1987), yielding $\zeta_\mathrm{ad} \lesssim 0$. On the other hand, radiative envelopes have steeper density gradients at the surface, and the uncovered layers are relatively denser than for convective envelopes. As a result, the adiabatic response of a radiative envelope leads to a more compact structure and a smaller radius, and $\zeta_\mathrm{ad} \gg 0$. We note that these simple estimations rest on the assumption that the donor will respond adiabatically to mass loss, which is not necessarily true and can lead to unnecessarily restrictive conditions for stable mass transfer (e.g., Passy et al., 2012; Pavlovskii & Ivanova, 2015a; Temmink et al., 2023). Using the assumption of adiabatic response for the donor, one determines the stability of the mass transfer by simply comparing ζ_ad and ζ_L:

- $\zeta_\mathrm{ad} \gtrsim \zeta_\mathrm{L}$: the donor either shrinks faster or expands slower than the Roche lobe does, and the mass transfer phase is considered to be dynamically stable. The mass transfer can then be driven by the slow expansion of the donor on its nuclear timescale or be regulated by thermal readjustments of the star.

- $\zeta_{ad} < \zeta_L$: the donor is unable to stay inside its Roche lobe, starting a phase of runaway mass transfer. This can happen in binaries with very large mass ratios or when the donor has a deep convective envelope (e.g., red giants and red supergiants). Dynamically unstable phases of mass transfer are generally thought to result in a phase of common envelope evolution, during which the accretor plunges into the donor's envelope.

Common envelope evolution

Common envelope evolution (CEE) is a phase of binary evolution where one of the stars is engulfed and spirals into the envelope of its companion (Paczynski, 1976). It can be broadly divided into four stages, from the initial loss of orbital stability to the formation of the post-CEE system.

CEE starts with a steepening decay of the orbit, which is generally triggered by a dynamically unstable phase of mass transfer where the donor cannot stay contained in its Roche lobe. This is most common for donors expanding in the giant phase, with a convective envelope, but can also happen for donors with radiative envelopes in high mass ratio binaries, where the Roche lobe shrinks faster than the donor. CEE can also arise in asynchronous binaries where the Darwin instability occurs and tidal forces dramatically shrink the orbit. This instability is relevant for binaries where the rotation angular momentum of the more massive star is greater than one-third of the orbital angular momentum of the system (Darwin, 1879a; Hut, 1980b), which generally occur in binaries with very large mass ratios.

As the orbit tightens, the companion eventually plunges into the envelope of the donor star and orbit its core. The drag between the companion and the gas in the envelope decreases the orbital angular momentum of the companion, which further tightens the orbit and causes the companion to spiral in the envelope. The release of gravitational energy heats the surrounding envelope which then expands and can become fully or partly unbound from the system. The inspiral phase is therefore driven by a mechanical transfer of energy and essentially occurs on the dynamical timescale of the envelope. Depending on the nature of the system, this phase can eject the whole envelope of the donor and result in a tight binary composed of the companion and the core of the donor, or the inspiral phase can transition to a slower inspiral or a merger. In case of a merger, the mass ejection during the inspiral appears to cause an increase in luminosity of the system, which is commonly called luminous red nova (e.g., Soker & Tylenda, 2006; Ivanova et al., 2013a; Pejcha et al., 2016a; Ivanova et al., 2013b)

If the rapid inspiral does not eject the whole envelope of the donor, it is possible that the envelope is sufficiently expanded to slow down the inspiral, and the envelope close to the binary might start co-rotating with the binary, further reducing the orbital energy dissipation. Then, the non-ejected envelope has time to thermally adjust to a new equilibrium, so that energy is radiated away at its surface at the same rate as orbital energy is released by the inspiral. The slower inspiral is then kept stable by the equilibrium between the heat released by the orbital decay and the energy loss at the surface. This phase, called "self-regulated inspiral" (Meyer & Meyer-Hofmeister, 1979), occurs on the thermal timescale of the common envelope, and is therefore much slower than the previous phases of CEE. It is expected to end either in a merger, if the quasi-steady state of the inspiral is perturbed, or in a short-period binary if the system was able to eject the rest of the envelope, e.g. through pulsations and winds (Clayton et al., 2017a; Glanz & Perets, 2018a).

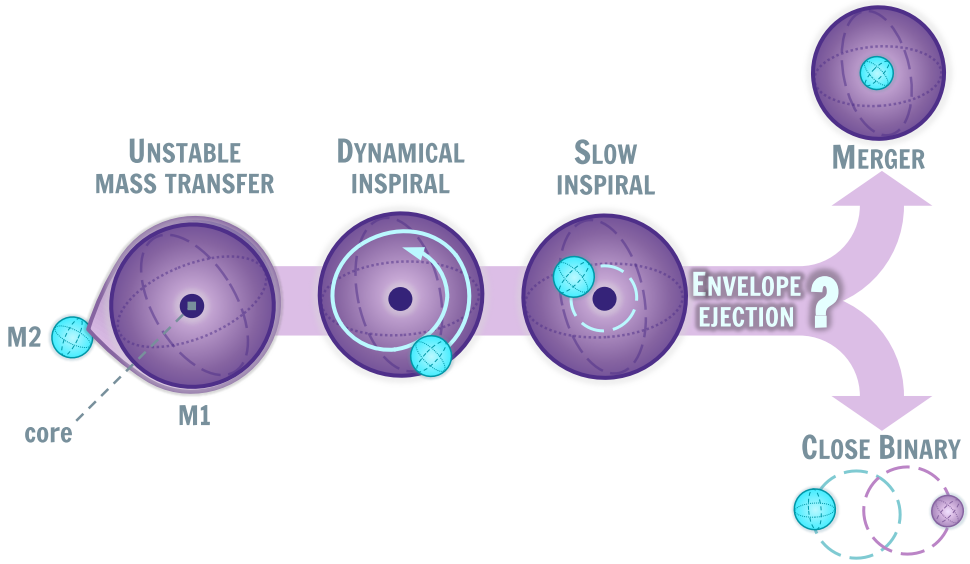

Figure 1.5: Illustration of a system undergoing common envelope evolution starting from unstable mass transfer. The accretor plunges into the envelope of the companion, starting a phase of dynamical inspiral, until the orbit stabilises. The outcome of the ensuing slow inspiral phase depends on the amount of envelope ejected during the process, it should generally result in a merger or a close binary.

CEE is not always expected to follow these phases specifically, e.g. a second phase of dynamical inspiral might happen after the self-regulated inspiral or the self-regulated phase might not occur at all. But overall, CEE has two possible outcomes, which we summarise in Fig 1.5: the donor core and companion can merge, or the envelope is fully ejected and leaves a short-period binary behind. Thus, CEE can produce a wide variety of tight binary systems, which can later produce transients (e.g., cataclysmic variables, X-ray binaries), become gravitational waves sources (e.g., Klencki et al., 2021a; Marchant et al., 2021a) or produce exotic supernovae (e.g., Chevalier, 2012). As such, CEE is an important process of binary evolution, and large efforts have been put into constraining its outcomes and the envelope ejection efficiency.

The outcome of CEE is often approximated through simple formalisms, for instance by parametrising the efficiency of the transfer of orbital energy to unbind the envelope ("α-formalism", van den Heuvel 1976; Webbink 1984) or the difference of angular momentum due to mass loss between pre- and post-CEE states ("γ-formalism", Nelemans et al. 2000). While these approximations of CEE are useful for quick binary evolution estimates, e.g. for population models, it is clear that they widely neglect the details of the physical interaction between the two stars, which are still fairly unconstrained and strongly dependent on the initial conditions of the CEE. CEE is therefore best studied through 1D and 3D numerical simulations. However, due to the enormous range of time and length scales involved, numerical studies of CEE are always restrained to specific phases of the CEE process and often involve considerable assumptions.

In particular, it is still unclear which physical processes play a significant role in the envelope ejection and tightening of the orbit. For instance, the contribution of recombination energy to the unbinding of the envelope is still an open question (Ivanova, 2018; Soker et al., 2018, e.g.,), and the relevance of dust formation for the ejection of the envelope and the ensuing transient is uncertain (González-Bolívar et al.,

2022; Bermúdez-Bustamante et al., 2024). Similarly, the evolution of the binary and ejected envelope after the dynamical inspiral is fairly unconstrained (Gagnier & Pejcha, 2023, 2024). Thus, despite considerable effort in constraining the initial conditions and the relevant physical processes involved in the envelope ejection, the evolution of the ejecta and the associated transient, CEE is far from being understood (e.g., Röpke & De Marco, 2023).

1.2.2 Impact on stellar evolution

Interacting binaries do not necessarily follow a well-defined evolutionary path, as the effect of mass transfer and tidal interactions depends on a variety of parameters and physical processes (e.g., metallicity, rotation, convection). We can, however, estimate the effect of the different phases of mass transfer on both stellar components separately from relatively simple assumptions on stellar structure and evolution.

Since stars can expand and fill their Roche lobe on multiple occasions during their lifetime, mass transfer can occur at different stages of stellar evolution. The structure of the donor changes as it evolves, which affects its response to mass loss, therefore we can distinguish three cases of mass transfer depending on the phase of stellar evolution they disturb. Case A mass transfer corresponds to when the donor undergoes RLOF during its MS, Case B occurs when the Hydrogen in its core is depleted, and Case C after the end of core Helium burning. A binary system can undergo several phases of mass transfer at different stages of their stellar evolution, e.g., stars can undergo Case B mass transfer after Case A mass transfer. Additionally, the accretor of the mass transfer phase may later evolve and overfill its Roche lobe, becoming the donor of a new phase of mass transfer.

The convective processes in the envelope of the donor play a significant role in determining its response to mass loss, so Case B is generally separated into early Case B and late Case B to distinguish evolutionary phases where the star is only starting to develop its convective envelope from phases where the envelope is fully convective. During late Case B and Case C mass transfer, the donor has a deep convective envelope that expands in response to mass loss (Hjellming & Webbink, 1987). Conservative mass transfer is therefore expected to be unstable according to the criteria derived in Section 1.2.1 and commonly lead to CEE. On the other hand, Case A and early Case B occur when the donor has a significantly radiative envelope, and the binary is expected to undergo stable thermal timescale mass transfer that can be assumed to be broadly conservative.

Case A mass transfer is generally expected to first occur rapidly on the thermal timescale of the donor, during which the radiative envelope of the donor contracts and its luminosity decreases in response to the mass loss. This fast phase of mass transfer continues until the donor becomes less massive than the accretor, and can then relax into TE and fit within its Roche lobe. Afterwards, the binary transitions to a slower phase of mass transfer driven by the expansion of the donor on its nuclear timescale, until the end of the MS phase of the donor. Due to its much longer evolution timescale, most detached binaries are expected to be observed in the slow phase of Case A mass transfer, in which case they are referred to as Algol-type systems. After experiencing Case A mass transfer, the donor is expected to appear more luminous and expanded than an isolated star of the same mass.

Early Case B mass transfer generally starts when the donor leaves the MS phase and

expands to regain the TE lost when the core stopped burning Helium. The expansion of the envelope substantially decreases its thermal timescale, yielding a rapid thermal mass transfer phase that is faster than during Case A mass transfer. Furthermore, the donor expands on timescales much faster than the nuclear timescale, so Case B mass transfer does not show a second slower phase and instead continues after the mass ratio has been reversed at a high rate until most of the donor's envelope has been transferred. At this point, the fast stripping of the radiative envelope drastically reduces the radius of the star, which severely perturbs its TE. The donor needs to re-expand to regain TE, so the energy produced by the H-burning shells is used in the expansion rather than being radiated away at the surface, which results in a dramatic decrease in luminosity. The mass transfer continues stripping the donor of its envelope until it is reduced to a Helium core surrounded by a thin H-rich layer, He-burning starts in the core and the star contracts, detaching from its Roche lobe and effectively stopping the mass transfer phase. Case B mass transfer is therefore expected to produce stripped Helium stars (Drout et al., 2023; Götberg et al., 2023), which is mostly relevant for massive stars of initial masses $\leq 25 M_{\odot}$, in which case stellar winds are not efficient enough to strip the star of its envelope. Such stars are of high importance since they are high ionisation sources and the best progenitors for H-poor core-collapse supernovae (e.g., Eldridge et al., 2013). Case B mass transfer is very short-lived and thus less likely to be observed than Case A mass transfer. However, it produces systems that are expected to be long-lived and observable (e.g., Shenar et al., 2020), because the conservative mass transfer should widen the orbit once the mass ratio is reversed, and the stars are not expected to interact anymore.

Conservative stable mass transfer thus significantly impacts the stellar structure of the donor, and its long-term evolution strongly diverges from single-star evolution. We illustrate these effects in Fig 1.6, where we sketch the evolution of binary stars undergoing different phases of mass transfer. Naturally, the evolution of systems undergoing mass transfer becomes much more complicated when considering non-conservative processes, e.g. stellar winds or a Roche lobe overflowing accretor, or effects arising from different properties of stellar evolution, such as stellar rotation and mixing (Maeder, 1987) or metallicity (Klencki et al., 2022).

Response of the accretor

Mass transfer also affects the secondary star, as it gains mass and angular momentum when accreting matter from the donor star, impacting both its structure and evolution.

As the accretor gains mass, its envelope is compressed by the newly added layers. This compression can bring the star out of TE if it occurs on timescales shorter than the thermal timescale of the star because the release of gravitational energy due to the compression is out of balance with the energy radiated away at the surface of the accretor. Similarly to the response of the donor to mass loss, the rearrangements of the accretor to regain TE are dependent on the nature of the envelope: a convective envelope contracts in response to mass gain, while a radiative envelope expands. The luminosity of the accretor will also increase due to the mass gain and deviate from the value appropriate for its mass and age according to single-star evolution. Furthermore, if a MS accretor has a high enough mass accretion rate, it might substantially expand and overfill its own Roche lobe, resulting in the formation of a contact binary and potential mass loss through the L2 point.

Besides gaining mass, the accretor also gains angular momentum from the accreted

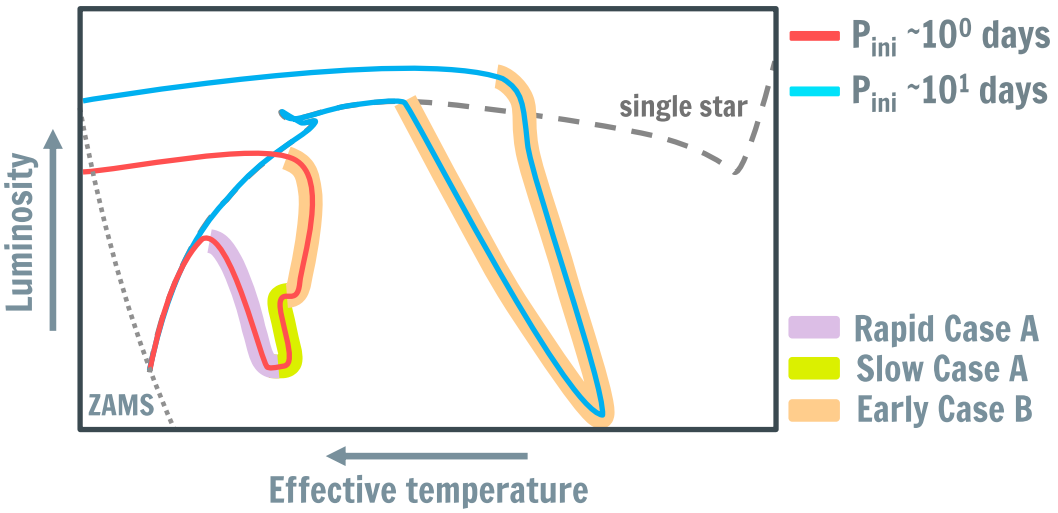

Figure 1.6: Illustration of the evolution of donor stars in two binary systems composed of massive stars ($M \gtrsim 8\,M_\odot$): a system with an initial period of the order of days undergoing Case A then early Case B mass transfer (blue line), and a system with a period of the order of 10 days undergoing early Case B mass transfer (red line). The donor evolution starts from the zero-age main sequence (ZAMS, dotted line), and the evolution of an isolated star of the same initial mass is shown as a grey dashed line. Phases of fast and slow Case A mass transfer are denoted by thick purple and green lines respectively, and early Case B is shown as thick orange lines.

material, which can bring the star close to critical rotation (e.g., Packet, 1981). Therefore, there needs to be a mechanism that regulates the spin of the accretor to prevent it from reaching break-up rotation. This can generally be achieved through tidal interactions, which transfer some spin angular momentum into orbital angular momentum, or through stellar winds, which can be significantly enhanced when the star is close to critical rotation. The spin-up of the star can also strongly affect its structure, for instance by giving rise to strong convective motion that alters the density profile of the envelope (e.g., Renzo & Götberg, 2021). Mass transfer is therefore thought to be an important mechanism through which rapidly rotating massive stars such as Be stars are produced (e.g., de Mink et al., 2013; Shenar et al., 2020).

Depending on when the mass transfer is taking place, the gas accreted by the companion star might not be only composed of H. In the case of relatively evolved donors, the convective motion in their envelope has brought up material from the deeper layers of the star, which has been processed by H-burning cycles (CNO or p-p processes) in the core and H-burning shells. Thus, if a system undergoes case B or C mass transfer, it is likely that a fraction of the transferred mass is chemically enriched, and the surface composition of the accretor can be altered by the accretion process (e.g., Renzo & Götberg, 2021; El-Badry et al., 2022).

Finally, in the case of MS accretors with convective cores, the large increase in mass has a strong consequence for their long-term evolution. In such stars, the convective core grows in mass and radius as the star gains mass and gets access to new hydrogen layers that have not been previously processed by H-burning (Neo et al., 1977). While the H-content of the core increases, it also has to burn Hydrogen faster to maintain the TE of the accretor, since an increase in mass results in an increase in energy radiated

away. However, the effect of the increased H-content dominates, and this process, called "rejuvenation", effectively increases the lifetime of the MS phase of the accretor.

1.3 Accretion discs

In the case of wind-fed mass transfer, the mass accretion can be described using Bondi-Hoyle-Lyttleton accretion(Bondi & Hoyle, 1944). However, during phases of stable mass transfer through RLOF and possibly wind-RLOF (e.g., El Mellah et al., 2019), the material flowing through the L1 point has significant angular momentum due to the orbital motion, and thus cannot flow radially towards the secondary star. Instead, it should start orbiting the companion. If the accretor has a radius larger than the periastron distance of the orbit, the gas will form a direct accretion flow to the star. However, for smaller accretors the stream flows around the star and eventually collides with itself as it completes one orbit. The shocked gas cannot efficiently dissipate angular momentum, and the infalling matter piles up and starts forming an accretion disc. The gas in the disc slowly falls in and is either accreted when it reaches the stellar surface or when it interacts with the magnetic field of the star and is accreted trough the poles.

1.3.1 Evolution of the disc

Matter in an accretion disc approximately follows circular Keplerian orbits, so that its velocity v and angular momentum ℓ both depend on the distance to the accretor according to:

$$v(r) = \sqrt{\frac{GM_2}{r}},\ \ell(r) = \sqrt{GM_2 r}, \tag{1.13}$$

where M_2 is the mass of the accretor and r is the distance between the parcel of gas and the accretor. This is mostly accurate for the innermost sections of the disc, where the potential of the accretor is the strongest influence by far, however in outer regions, the potential of the companion and the self-gravity of the disc also contribute and the Keplerian approximation is less adequate. The Keplerian rotation causes a tangential velocity gradient along the radial direction of the disc, and the velocity difference between fluid parcels in the disc drives viscous processes, which transport angular momentum outwards. According to equation 1.13, the decrease of angular momentum of the innermost regions of the disc brings them closer to the central star, which in turn increases their velocity, and conversely, its outer regions spread further away from the accretor when gaining angular momentum. The transport of angular momentum through viscous processes allows matter from the disc to eventually reach the star to be accreted and thus drives the evolution of the accretion disc.

The origin of viscosity in accretion discs is not well understood. The usual dynamical viscosity due to collisions between microscopic components of the gas is inefficient in accretion discs because they are too dense ($\sim 10^{15}$ cm^{-3}) and the stream velocity is much greater than the thermal velocity of the gas. Instead, flows in accretion discs are thought to be very turbulent, which can drive an effective viscosity that allows the transport of angular momentum. The source of this turbulent viscosity is unknown, but the best candidate is the magneto-rotational instability (MRI) (Balbus & Hawley, 1991) resulting from weak magnetic fields and differential rotation. If we consider two

parcels of fluid in the disc on the same magnetic field line, the Keplerian motion of the disc causes the parcel closest to the accretor to move faster than the one further away, which stretches the field line connecting the two parcels. Magnetic tension acts to restore the field line by slowing down the inner parcel and accelerating the outer parcel, effectively transporting angular momentum outward. If the magnetic field is weak, it cannot balance the loss/gain of angular momentum of the inner/outer parcels, leading to further acceleration/deceleration and the growth of the instability. On the other hand, strong magnetic fields can bring the parcels back onto similar orbits and keep the disc stable against MRI.

While the mechanism for angular momentum transport in discs is still an open question, accretion disc simulations can be performed by making several key assumptions, such as axisymmetry, stationarity, hydrostatic equilibrium, and Keplerian rotation. The most utilised formalism for accretion disc models is the α-disc, introduced by Shakura & Sunyaev (1973), which assumes a geometrically thin disc in which the viscosity is described with a simple parameter α according to $\nu = \alpha H c_s$, where c_s is the sound speed, and the heat generated by viscous processes is immediately radiated away. This model can be further complicated by including relativistic effects (Novikov & Thorne, 1973), cooling via advection Ichimaru (1977), or different assumptions on disc geometry such as thick discs Abramowicz et al. (1978).

1.3.2 Transients from accreting binaries

As matter is transferred through the accretion disc and then accreted by the central object, part of its energy is dissipated as heat, which can be partly radiated away. The bolometric accretion luminosity of the system can be estimated as:

$$L_{\rm acc} \simeq G M_2 \frac{\dot{M}_2}{R_2}, \tag{1.14}$$

for an accretor of mass M_2 and radius R_2 accreting at a rate of $\dot{M}_2$. In total, half of $L_{\rm acc}$ should be radiated away by the accretion disc and the other half by the accretion onto the star itself. Since smaller accretors cause a much stronger release of potential energy when matter gets closer to the stellar surface, the luminosity of the accretion process is determined by the mass accretion rate and the accretors' radius. In reality, the efficiency of the radiative processes during accretion is more complicated than equation 1.14: it relies on the opacity and thermal structure of the disc, as well as the nature of the accretor. For instance, it is necessary to account for relativistic effects in systems with black holes and neutron star accretors. The most radiatively efficient disc models generally assume geometrically thin discs with high optical depth (e.g., α-discs) and can predict that up to 42% of the rest mass of the gas accreted by a rapidly rotating black hole is radiated away (Thorne, 1974).

Overall, the observability of a disc in an accreting binary strongly depends on the nature of the system. For instance, systems undergoing Case A mass transfer (Algol binaries) may form an accretion disc, but the MS accretor generally has a large enough radius that the accretion luminosity is relatively low and thus not always distinguishable from the other components of the system. On the other hand, very evolved interacting binaries in which the accretor is a compact object are more likely to have observable accretion luminosities. Binary systems containing at least one massive star may undergo more phases of mass transfer after the massive star collapses as a neutron star (NS) or

black hole (BH) if the binary was not unbound by the natal kick of the compact object. In such cases, the companion may transfer mass through RLOF, wind-RLOf or direct wind-fed mass transfer, and the compact object accretes through an accretion disc. Due to the small size of the accreting compact object, the disc emits strong X-ray radiation, such systems are thus called X-ray binaries (e.g., Tauris & van den Heuvel, 2006).

Cataclysmic Variables

Cataclysmic variables (CVs) are a relatively common type of close binaries of periods $P \leq 0.5$ days composed of a white dwarf (WD) accreting matter from a low-mass MS star overfilling its Roche lobe (Warner, 2003a). The WD generally accretes through an accretion disc, the matter can either be directly transferred to the surface of the WD through the disc or be accreted through the magnetic poles of the WD if it has a significant magnetic field ($B \geq 10^5$ G, polar and intermediate polar CVs, e.g., Cropper, 1990). The mass of the WD is generally slightly larger than that of the companion, and mass transfer proceeds stably at very low accretion rates ($\dot{M} \sim 10^{-10} M_\odot/\mathrm{yr}$). Beyond the usual variability attributed to close binaries, these systems undergo one or several sudden increases in brightenings, called outbursts, hence their classification as "cataclysmic" variables. The nature and properties of these outbursts vary, giving rise to various sub-classes of CVs, although they are always a consequence of accretion processes. For instance, classical novae are bright outbursts of amplitude $6 - 19$ mag caused by the flash ignition of Hydrogen on the surface of the accreting WD. H-rich matter accumulates on the surface layers of the WD until the pressure and temperature conditions are suitable for H-burning, resulting in a thermonuclear runaway reaction that ejects material and results in a strong brightening of the system (Starrfield et al., 2016). Beyond removing the accreted H-layer, the outbursts do not perturb the system much and mass can start to accumulate again on the WD surface until the next outburst. Considering the slow accretion rates of CVs, classical novae are generally expected to recur over very long time scales, beyond 10^4 years (Shara et al., 2018). Several systems do show more frequent nova outbursts, on timescales of tens of years, with lower amplitude than classic novae (≤ 9 mag), in which case the outbursts are called recurrent novae Schaefer (2010).

Another common class of CV is the dwarf nova type (DN), which exhibits fainter outbursts of amplitude ≤ 9 mag recurring semi-periodically over $10 - 100$ days periods originating from thermal instabilities in the accretion disc. DNe outbursts are commonly described using the disc instability model (DIM, e.g. Meyer & Meyer-Hofmeister, 1981; Smak, 1982; Cannizzo et al., 1982; Faulkner et al., 1983; Mineshige & Osaki, 1983), describing a non-stationary α-disc oscillating between cold and hot thermal equilibria linked by a thermally unstable region. The left panel of Fig. 1.7 shows the S-curve of such a disc, which describes the evolution of surface density and effective temperature in the disc. During quiescence, the accretion disc is cold and can be described with a low viscosity parameter $\alpha_{\mathrm{cold}} \sim 0.02 - 0.04$. As mass accumulates, the local densities and temperatures gradually increase until a local critical value is reached somewhere in the disc to trigger the thermal instability. This critical value is defined by the ionisation temperature of Hydrogen (10^4 K), as the change in H^- abundance strongly impacts the local opacities, and the vertical structure suddenly shifts from being convective in the cold state to being radiative in the hot state. Once the critical point is reached, any increase in density brings the local disc into its hot radiative state, triggering the outburst, greatly increasing the local mass transfer rate and the viscosity to $\alpha_{\mathrm{hot}} \sim 0.1 - 0.2$, and

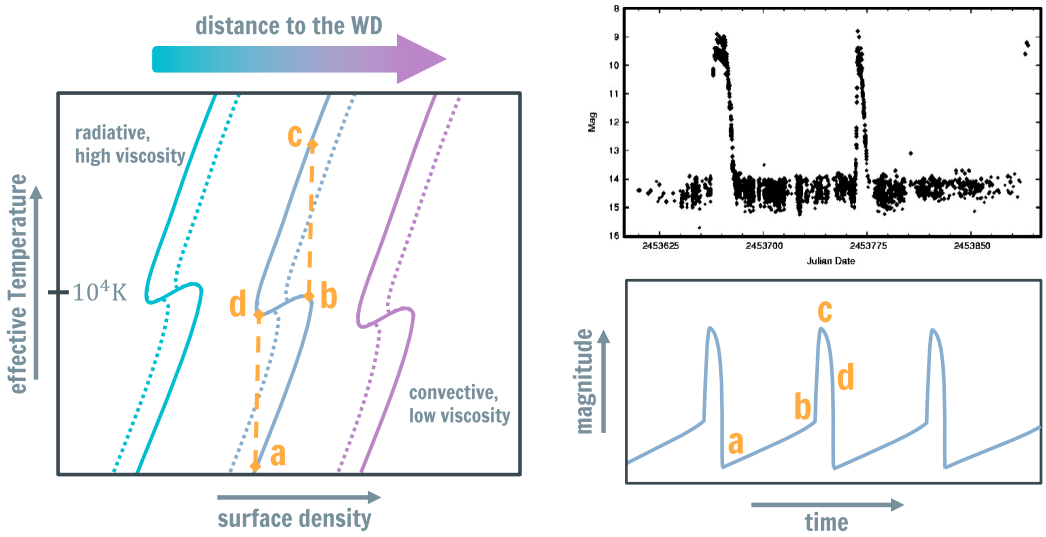

Figure 1.7: Illustration of the evolution of a DN through disc thermal instabilities. Left: Simplified plot of effective temperature vs surface density (S-diagram) of a DN accretion disc described by a disc with two α values depending on the local temperature. Solid lines show the actual S-curve of the disc, while dotted lines show the S-curve described by one value of α. The gradient in line colour shows the distance from the region in the disc described by the S-curve to the WD accretor, with the bluer line being the closest to the accretor and the purple lines the farthest. The branches with a positive slope describe thermal equilibrium, while the branches with negative slopes are thermally unstable. The orange lines show the evolution through the instability, starting from the quiescent disc (a) with a convective vertical structure until a region in the disc reaches the critical mass transfer rate (b). The disc is then brought to a hot viscous state by the outburst (c), after which the mass transfer rate decreases again until it reaches a minimum value (d) and can transition back to its cold state (a). Upper right: Optical light curve of a typical DN, U Gem, showing two outbursts separated by $\sim$ 100 days (credit: AAVSO). Lower right: Illustration of a synthetic light curve obtained from the disc models described by the S-curves on the left. The optical brightness of the system is shown in blue, while the corresponding phases of evolution of the unstable disc are shown in orange.

hence propagating the instability throughout the disc. From this point, the enhanced mass transfer rate starts decreasing until most of the mass within the disc has been transferred to the accreting WD, and the disc eventually returns to its cold convective state. This cycle occurs on the timescales of days and is generally expected to repeat almost periodically every 10 – 100 days. The photometric signature of the DIM is illustrated in the lower right panel of Fig 1.7 and is compared with observations of U Gem, a typical DN. The DIM successfully reproduces the frequency and amplitude of DN outbursts, but there are still inconsistencies. A particularly problematic issue arises during the quiescent phase, where the DIM predicts a slow but significant rise in luminosity as mass accumulates in the disc and the temperature increases before the outburst is triggered. This feature is completely absent from observed light curves of DNe, which instead remain completely quiescent until the outburst suddenly appears (Smak, 2000). Furthermore, the DIM is a relatively simple mechanism, so current

models are often accompanied by additional physical processes relevant to accretion disc evolution, such as disc irradiation by the WD and the secondary, self-irradiation, disc winds, and tidal instabilities. These improvements, which are reviewed in great detail by Hameury (2020), also allow to better model sub-types of DNe that exhibit additional features, such as the superoutbursts of SU UMa-type DNe or the long standstills interrupting the outbursts of Z Cam-type DNe. Overall, DNe outbursts strongly depend on viscous processes in the disc, so they are important probes of angular momentum transport in accretion discs. Thus, their observations are very valuable and provide great tests for accretion disc models. Currently, the DIM is based on the assumption of α disc, which relies on an empirical parametrisation of viscosity rather than physical estimations. Therefore, progress on constraining angular momentum transport in accretion discs, such as MRI, is necessary to improve the predictions of the DIM.

1.4 Studying binary evolution

While observations of binary populations, exotic stellar objects, and transients provide a strong test for the theories of binary evolution, they do not necessarily allow to constrain the complex physical processes involved in binary interactions. Since it is not possible to reproduce the details of binary evolution through experiments in a lab, we instead rely on numerical simulations aiming to reproduce stellar interactions as accurately as possible to obtain predictions that can be tested on observations. These simulations are performed by evolving in time complex sets of differential equations across a whole domain, which are defined by the various physical processes involved in the model.

The general accuracy of astrophysical models, not just in the case of binary evolution, suffers from great limitations due to the spatial and temporal scales on which the simulations must be performed. The former is very obvious when simply investigating the relevant length scales in stars: their envelopes generally extend beyond several solar radii, while the atoms composing the star have a size of the order of an Ångström. The timescale discrepancy arises from the different temporal scales of the physical processes occurring in the simulation, for instance, stars evolve over their nuclear timescales, but their thermal and mechanical equilibria are regulated on thermal and dynamical timescales, respectively. In the case of the Sun, the dynamical timescale is around 1100 seconds, while its thermal timescale reaches 3×10^7 years, and its main sequence evolution lasts about 7×10^9 years. Thus, it is often necessary to compromise by choosing to evolve the model over reduced ranges of length and time or to resolve only a subset of the physical processes involved based on their relevance to the process studied.

Numerical simulations are an important tool to investigate and constrain astrophysical processes, but the assumptions made to perform the simulations do not necessarily yield the most accurate predictions. It is thus necessary to understand the details of the numerical methods used and determine how the results could be impacted under different assumptions. In this thesis, we performed different 3D hydrodynamics simulations using the open source codes PHANTOM (Price et al., 2018) and FLASH4.5 (Fryxell et al., 2000; Dubey et al., 2008), and thus we need to elaborate on hydrodynamics methods.

1.4.1 Hydrodynamics simulations

When simulating matter in stellar environments, one generally approximates it as a fluid to ignore smaller-scale effects such as atomic or molecular interactions. This alleviates part of the spacial scale issues, although the relevant scales to properly resolve the motion and gradients of the fluid remain considerably smaller than the domain, and further simplifications may be needed (e.g., reducing the number of dimensions). Using the fluid approximation, one can model and evolve the system by solving the equations of ideal hydrodynamics, given as:

$$\begin{aligned} \frac{\partial \rho}{\partial t} + \nabla \cdot (\rho \vec{v}) &= 0 \\ \frac{\partial (\vec{v})}{\partial t} + \vec{v} \cdot \nabla \ \vec{v} + \frac{\nabla P}{\rho} &= 0 \\ \frac{\partial e}{\partial t} + \vec{v} \cdot \nabla e + \frac{P}{\rho} \nabla \ \cdot \vec{v} &= 0. \end{aligned} \tag{1.15}$$

Here, ρ, p, e, and $\vec{v}$ are the local density, pressure, specific energy, and velocity of the fluid. The specific energy is given as the sum of the local internal and kinetic energies of the fluid $e = u + v^2/2$. These equations are derived from the conservation of mass, momentum, and energy in their Eulerian form, i.e., as observed from a fixed reference frame. Alternatively, one can derive these equations using a reference frame that follows the flow of the fluid, simply by setting the convective derivative:

$$\frac{D}{Dt} = \frac{\partial}{\partial t} + \vec{v} \cdot \nabla. \tag{1.16}$$

Applying the convective derivative to equation 1.15 yields the Lagrangian hydrodynamics equations:

$$\begin{aligned} \frac{D\rho}{Dt} + \rho \nabla \cdot \vec{v} &= 0 \\ \frac{D\vec{v}}{Dt} + \frac{\nabla P}{\rho} &= 0 \\ \frac{De}{Dt} + \frac{\mathrm{P}}{\rho} \nabla \cdot \vec{v} &= 0. \end{aligned} \tag{1.17}$$

Each form of the hydrodynamics equations can be used to perform hydrodynamics simulations, but they have to be solved using different methods that each have upsides and downsides. The best choice thus mainly depends on the nature of the problem at hand.

The equations of hydrodynamics are a set of 2+D equations, with D the number of dimensions of the problem, but they contain 3+D unknowns. Therefore, one needs an additional equation to close the system of equations, guaranteeing a unique solution per set of initial conditions. Generally, one adds an equation of state (EoS), which describes how the system behaves thermodynamically by defining how the state variables ρ, p, and e depend on one another and other state quantities such as the temperature T and mean molecular weight μ. Since there does not exist a single EoS that can describe all substances under all conditions, the choice of EoS depends on the model and how much microphysics one wants to include. One of the simplest options is the ideal gas EoS, which in terms of ρ, p, and u is given by:

$$P = (\gamma - 1)\rho u, \tag{1.18}$$

where γ is the adiabatic index. This form of EoS is easily solved and thus a very efficient option, though it greatly approximates the thermodynamics of the system. For more precision, one generally complicates this equation of state by adding extra terms; e.g., for stellar interiors, it is often useful to account for radiation pressure, ions, and relativistic electrons and positrons. However, such complicated EoS require a lot more time to solve and are instead often included in tabulated forms to maintain high efficiency (e.g., Helmholtz EoS from Timmes & Swesty 2000, OPAL EoS from Rogers et al. 1996). In such cases, the exact value describing a specific thermodynamic state is derived by interpolating from the table instead of exactly solving the equation.

Discretisation

Once the system of equations to solve is determined, the fluid has to be discretised. The sets of equations 1.15 and 1.17 are given in a continuous form, both in time and space, however, due to the limitations of computational work, it is not possible to simulate a system described by continuous functions. Instead, one has to represent these functions through a set of points in space and solve the equations at regular time intervals. This discretisation can be done in different ways, which can generally be defined as grid-based and gridless methods. Gridless (or mesh-free) methods can be achieved through different formalisms. In spectral methods, the solutions to the hydrodynamics equations are expressed as a superposition of basis functions (e.g., Fourier series, Jacobi polynomials). Although rarely used in computational astrophysics due to strong geometry requirements and the complicated treatment of shock, they have been used, for example, to model stellar evolution (e.g., Rieutord et al., 2016). Particle-based codes are another, more common, type of mesh-free method which aims to discretise the fluid as a set of point particles and then construct the continuous functions by integrating the particle contributions according to a kernel function defined by a characteristic smoothing length. The most commonly used particle scheme is called smoothed particle hydrodynamics, which is a very popular formalism in astrophysics. We detail this method in Section 1.4.2 and expand on its benefits as well as its disadvantages. In grid-based methods, the fluid is discretised according to a grid according to a specific scheme. The grid can be structured, where you can refer to the location of any cell in the grid using integer indices in the spatial dimensions, or unstructured, defined by a tessellation where the ordering of the elements in the grid is not straightforward (e.g., triangular or tetrahedral cells). Such grids are very useful for representing irregular domain geometries but require complicated data structures. These grids can be Eulerian, by fixing the cells to specific points in space, or Lagrangian, e.g., following the fluid by defining the cells according to non-spatial coordinates. The equations of hydrodynamics can be discretised onto the grid according to different schemes, such as the finite-difference, finite-volume, or finite-element methods, though the finite-volume formalism is the most standard in computational astrophysics. We discuss finite-volume methods further in Section 1.4.3. Once the fluid is discretised in space, it is evolved through time at regular discrete intervals, often called timesteps. Time-stepping can be achieved through different methods, broadly categorised into implicit and explicit schemes. Implicit time integration methods determine the state of the system at the next timestep from both the current state and the state at the next step, while explicit schemes determine the next step from the current state only. Implicit time-stepping methods are thus more expensive and their implementation is not necessarily straightforward, since they require solving an additional equation through multiple iterations. However, these

methods are more stable than explicit time integration schemes, which are restricted by the Courant–Friedrichs–Lewy (CFL) condition (Courant et al., 1967), stating that the scheme can only be stable if the timestep is smaller than the crossing time of the fastest wave over the smallest resolvable length (e.g., cell size for grid-based codes, smoothing length for particle methods). In some cases, the CFL condition may dramatically decrease the length of a timestep, increasing the cost of the simulation to the point where an implicit time-stepping scheme would be favourable. Nevertheless, explicit time integrators are more common due to their speed and ease of implementation, the most popular schemes being the 4$^{\text{th}}$ order Runge-Kutta integrators for grid-based methods and leapfrog algorithms for particle-based methods.

1.4.2 Smoothed particle hydrodynamics

Smoothed particle hydrodynamics (SPH) is a formalism originally developed by Lucy (1977) and Gingold & Monaghan (1977) for astrophysical purposes, which solves the Lagrangian form of the equations of hydrodynamics (equation 1.17). Since then, it has become a widely used technique in computational astrophysics with diverse applications, and a great number of open-source codes are available nowadays (e.g., Phantom Price et al. 2018, Gadget-4 Springel et al. 2021, Gasoline-2 Wadsley et al. 2017). We used this technique and the code Phantom to perform the simulations presented in Chapter 3.

Formalism

To solve the Lagrangian equations of hydrodynamics, SPH relies on a particle-based discretisation scheme that approximates the density around a particle a as the weighted sum of the masses of the neighbouring particles m_b:

$$\rho_a = \sum_b m_b W\left(\vec{r}_a - \vec{r}_b, h_a\right), \tag{1.19}$$

where the weighting function W is called the smoothing kernel and its strength falls off with the distance to the central particle according to a characteristic length h called the smoothing length. The size of the neighbourhood of each particle is determined by the smoothing kernel and the smoothing length, which thus define the accuracy of the density estimate. The density estimate in equation 1.19 can be used to derive the equations of hydrodynamics, which yield the SPH equations for each particle:

$$\begin{aligned}
\rho_a &= \sum_b m_b W\left(\vec{r}_a - \vec{r}_b, h_a\right); \quad h = h(\rho), \\
\frac{\mathrm{d}\vec{v}_a}{\mathrm{d}t} &= -\sum_b m_b \left[\frac{P_a}{\Omega_a \rho_a^2}\nabla_a W_{ab}\left(h_a\right) + \frac{P_b}{\Omega_b \rho_b^2}\nabla_a W_{ab}\left(h_b\right)\right], \\
\frac{\mathrm{d}u_a}{\mathrm{d}t} &= \frac{P_a}{\Omega_a \rho_a^2}\sum_b \; m_b\left(\vec{v}_a - \vec{v}_b\right)\cdot\nabla_a W_{ab}\left(h_a\right),
\end{aligned} \tag{1.20}$$

where Ω_a is a term accounting for the gradient of the smoothing length:

$$\Omega_a \equiv \left[1 - \frac{\partial h_a}{\partial \rho_a}\sum_b m_b \frac{\partial W_{ab}\left(h_a\right)}{\partial h_a}\right]. \tag{1.21}$$

These equations have the very important property of exactly conserving energy and linear and angular momentum. We note that equation 1.20 is for ideal hydrodynamics, but additional terms may appear if one considers extra physical processes, such as gravitational forces or magnetic fields. Additionally, one may want to add a form of artificial viscosity to this system to treat discontinuities, for instance, in fluids with high Mach numbers where shocks are common. It is thus common for SPH schemes to introduce a shock-capturing term to keep stable solutions around shock waves, and this is achieved by introducing artificial dissipative terms in the momentum equation and a conductivity term in the energy equation. Since SPH solves a discrete form of the equations of hydrodynamics, the fluid quantities need to be reconstructed from the particle quantities so that they can be evaluated at any point in space. This is done by interpolating the quantities of interest in the same way the density was estimated in equation 1.19, such that the value of a scalar $A(r)$ is given by:

$$\langle A(\mathbf{r}) \rangle \approx \sum_{b=1}^{N_{\text{neigh}}} m_b \frac{A_b}{\rho_b} W\left(\vec{r} - \vec{r}_b, h\right) . \tag{1.22}$$

This interpolation also works for fields and gradients, although the interpolated gradients generally contain large errors and require a thorough error analysis to correct their estimates (see section 4.3 of Price, 2012). Overall, the basic accuracy of SPH simulations is affected by two choices: the number of particles, the smoothing length, and the kernel. The impact of the number of particles is fairly evident, resolving the same fluid with a larger amount of particles allows to resolve the smaller-scale motion of the fluid, so ideally one wants a high number of particles. On the other hand, choosing the proper smoothing length and smoothing kernel is less straightforward.

Smoothing kernels and smoothing length

The choice of smoothing kernel is, in principle, left at the discretion of the user. However, good kernels should satisfy several conditions. First, they should have smooth derivatives and be symmetric (i.e., $W(\vec{r_a} - \vec{r_b}), h_a) = W(\vec{r_b} - \vec{r_a}, h_a)$). They also need to be relatively flat around their centres so that small position fluctuations in the close neighbourhood do not strongly impact the fluid quantities estimate. Finally, these kernels should have a "compact support", i.e., they are truncated at a finite radius R_{kern} to limit the number of neighbours entering the density calculation. This is essential to maintaining the efficiency of SPH calculations since the contribution from distant particles is very insignificant, and including them in the density calculation increases the cost of the interpolation calculations unnecessarily. There exist several functions that are well-suited for smoothing kernels, such as B-splines (Schoenberg, 1946) and Wendland functions (Wendland, 1995). The most commonly used kernel is the M_4 spline, given by:

$$w(q) = \sigma \begin{cases} \frac{1}{4}(2-q)^3 - (1-q)^3, & 0 \leqslant q < 1 \\ \frac{1}{4}(2-q)^3, & 1 \leqslant q < 2 \\ 0. & q \geqslant 2 \end{cases} , \tag{1.23}$$

which is truncated at $R_{\text{kern}} = 2h$. Here, σ is a normalisation constant and we simplified the notation so that $W\left(\left|\vec{r}_a - \vec{r}_b\right|, h_a\right) \equiv \frac{1}{h^d} w(q)$, and $q = \left|\vec{r}_a - \vec{r}_b\right| / h_a$. An important property of smoothing kernels is that their truncation radius is defined by the smoothing

length, thus, the accuracy of the density calculation also depends on the choice of smoothing length h. In principle, the smoothing length can be chosen to be constant, which was the case for early SPH simulations. However, it is preferable to be able to resolve areas of both high and low density of particles evenly and thus allow the smoothing length to vary according to the local number density of particles n_a:

$$h_a = h_{\text{fact}}\, n_a^{-1/3} = h_{\text{fact}} \left(\frac{m_a}{\rho_a}\right)^{1/3}, \tag{1.24}$$

where h_{fact} establishes the proportionality between the mean particle separation and the smoothing length. This is only valid for equal mass particles, however, using unequal mass particles often yields problems when particles of different masses mix (e.g., Monaghan & Price, 2006) so most SPH codes are restricted to equal masses. The choice of h_{fact}, or equivalently the smoothing length, is generally borne out of numerical considerations. For instance, it has to remain below a certain threshold for B-spline kernels to avoid pair instability, which arises at a high number of neighbours (e.g., Morris, 1996). For Wendland kernels, which are insensitive to pair instability, it has to be sufficiently large because these functions generally show large density errors at a low number of neighbours (Dehnen & Aly, 2012). Therefore, the choice of smoothing length has to satisfy the stability and accuracy requirements of the smoothing kernel. Using the formulation of the smoothing length in equation 1.24, one can find the average number of neighbours around a particle depending on R_{kern}:

$$\bar{N}_{\text{neigh}} = \frac{4}{3}\pi \left(R_{\text{kern}} h_{\text{fact}}\right)^3 . \tag{1.25}$$

Thus, a kernel with larger compact support will naturally increase the average number of neighbours, which can be further increased by the kernel restrictions on h_{fact}. An overall increase in the mean number of neighbours generally results in more accurate but expensive fluid quantity estimates, thus, the choice of smoothing length and kernels impacts the precision of SPH simulations as well as their computational expense. There are many types of smoothing kernels, though it is difficult to find the best option: it is often case-dependent, and the cost increase of more accurate kernels is not necessarily matched by the difference in results. Thus, it is generally encouraged to test different kernels in their simulations to establish the kernel bias and opt for a better, more expensive kernel if the changes are significant.

Applications

SPH is a popular hydrodynamics method in computational astrophysics, mostly due to its capacity to handle large ranges of spatial scales. The resolved domain in SPH is defined by the particles, which means that any vacuum in SPH is a true vacuum, i.e., empty space has a density of exactly 0 g cm^{-3}, and any vacuum is not resolved by the code. Thus, SPH is particularly suited for simulation with clumps of fluid separated by vacuum over large distances, or where the fluid has to travel across large distances during the simulation since no amount of computation is going into resolving the empty space separating groups of particles. With this naturally adaptive resolution and the ability to cover broad length scales, SPH schemes are a prime choice for simulations of galaxy formation and evolution, dynamical collisions of stars, and star formation. When studying binary interactions, SPH is useful when considering large-scale problems,

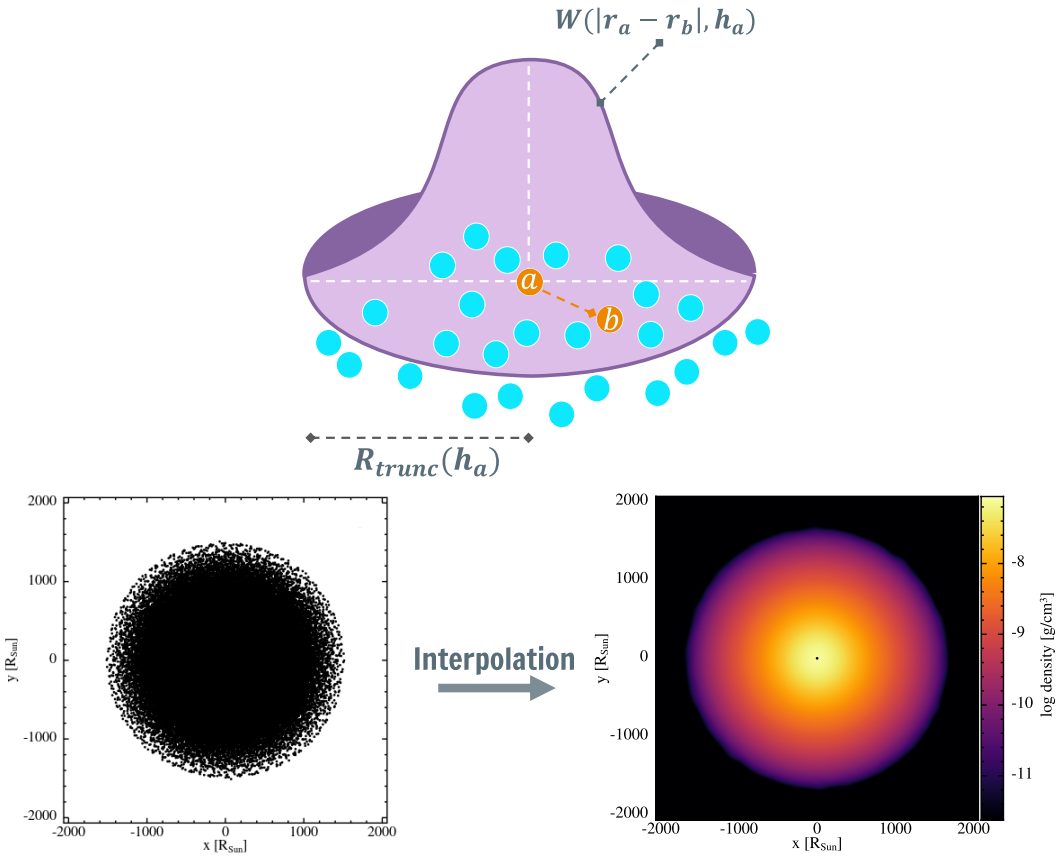

Figure 1.8: Top panel: Illustration of the SPH formalism, fluid quantities are computed as the sum of particle contributions weighted by a smoothing kernel W. The smoothing kernel falls off proportionally with the smoothing length h_a and is truncated at a radius $R_{trunc}(h_a)$ defined by the nature of the kernel and smoothing length. Bottom left panel: Example of a spherical distribution of SPH particles. Bottom right: Fluid density snapshot resulting from the interpolation of the particle distribution on the left.

such as CEE with very large donors (i.e., red supergiants) or wind interactions. SPH also has the advantage that the discretisation scheme exactly conserves energy and linear and angular momentum (to machine precision), no matter the choice of kernel and smoothing length. The time integration of the SPH equation itself is not exactly conservative, though in the ideal fluid case, the conservation remains extremely good (typically conserves to round-off error). Furthermore, the particle-based formalism and the naturally ensuing advection mean that SPH is well-suited to treat multi-phase fluids, e.g., different equations of state and/or chemical composition. The SPH method also comes with many significant drawbacks, the most well-known being its poor convergence rate (e.g., section 5 of Springel 2010). In the best-case scenario, with the proper choice of kernel and smoothing length, SPH can theoretically reach second-order convergence. However, the shock-capturing scheme used to treat discontinuities in the fluid tends to cause unnecessary dissipation in regions far away from discontinuities, which lengthens the convergence rate of the simulations, typically lowering it to first-order convergence. This artificial viscosity term is also the cause of another important disadvantage of the SPH methods: it tends to cause dynamical instabilities in the fluid, and the way it is parameterised is not borne out of physical considerations and

thus often results in excessive smearing of shocks. Another issue with SPH is that adaptive particle resolution (i.e., unequal particle masses) leads to instabilities. This is problematic for simulations with steep density gradients, such as the one at the surface of stars, in which case one has to dramatically increase the number of particles in the simulation to properly resolve such gradients. Moreover, the resolution cannot be dynamically adapted during the simulation, which means regions in the fluid with a low particle count will remain badly resolved until there is a significant inflow of particles, even if it is a region of interest. Efforts to add adaptive refinement in SPH are ongoing, e.g., Vacondio et al. (2016) developed a method where large mother particles split into smaller daughter particles to increase the local resolution.

1.4.3 Grid-based methods

In hydrodynamics methods based on structured grids, the discretisation of the hydrodynamics equations may be done through different schemes, such as the finite-difference or the finite-volume methods. The finite-difference method discretises the data as specific points in space (e.g., the edge or the centre of each cell) and solves the differential form of the hydrodynamics equations to obtain changes in cell quantities. On the other hand, the finite-volume scheme discretises the data as averages over the cell volume and calculates fluxes over cell surfaces by solving the integral form of the hydrodynamics equations instead of directly computing the change in cell quantities. The integral formulation of finite-volume methods has the advantage of being conservative by construction, while finite-difference methods are not locally conservative and require smooth solutions due to their differential formulations, meaning they tend to smooth out discontinuities even at very high resolutions. Since discontinuities are common in astrophysical fluids, finite-volume schemes are a better choice for hydrodynamics simulations of stellar environments and numerous open-source finite-volume codes have been developed for astrophysical purposes (e.g., Athena++ Stone et al. 2020, Pluto (Mignone et al., 2007), Ramses Teyssier (2002)). In Chapter 4 of this thesis, we performed 3D hydrodynamics simulations with the finite-volume code Flash4.5 (Fryxell et al., 2000).

Finite-volume method

Let's examine, for simplicity, a finite-volume grid in one dimension with N_x cells of size Δx. Functions are discretised in time through timesteps of Δt and in space by their average value over the interval $[x_{i-1/2}, x_{i+1/2}]$, where i goes from $[0, N_x - 1]$, and integer indices indicate the centre of a cell while half-integers define the cell edges. Thus, spatial coordinates are defined as:

$$x_i = \left(i + \frac{1}{2}\right) \Delta x \tag{1.26}$$

and any fluid quantity $q(x, t_n)$ is discretised in space as q_i^n according to:

$$q_i^n = \frac{1}{\Delta x} \int_{x_{i-1/2}}^{x_{i+1/2}} q(x, t_n) dx. \tag{1.27}$$

In 1D, the Euler equations can be expressed as:

$$\frac{\partial q}{\partial t} + \nabla \cdot \boldsymbol{F}(q, t) = 0 \tag{1.28}$$

where

$$q = \begin{cases} \rho \\ \rho u_x \\ \rho E \end{cases} \tag{1.29}$$

and

$$\boldsymbol{F}(q) = \begin{cases} \rho u_x \\ \rho u_x^2 + P \\ (\rho E + P) u_x \end{cases} \tag{1.30}$$

Integrating any of the Euler equations describes the time evolution of each cell as:

$$q_i^{n+1} = q_i^n - \frac{\Delta t}{\Delta x} \left(F_{i+1/2}^n - F_{i-1/2}^n \right) \tag{1.31}$$

where $F_{i+1/2}$ is the average of the flux $f(q)$ across $x = x_{i+1/2}$:

$$F_{i+1/2}^n = \frac{1}{\Delta t} \int_{t_n}^{t_{n+1}} f\left(q\left(x_{i+1/2}, t\right)\right) dt. \tag{1.32}$$

Thus, fluid quantities are updated at every timestep according to the fluxes across the cell boundaries. However, the fluid quantities are defined at the centre of the cells, and it is thus necessary to extrapolate their central values to reconstruct the fluxes at the edges of the cells. This extrapolation is generally done using a Godunov scheme by attributing a polynomial for each cell, e.g., constant functions (Godunov's method, Godunov 1959) or higher-order polynomials, thus approximating the function $q(x, t_n)$ as a set of N piecewise polynomials. The extrapolation in each cell results in different states at each side of the cell interfaces, e.g., in the case of a piecewise constant approximation to $q(x, t_n)$ we can express the extrapolated value $\tilde{q}^n(x, t_n)$ as:

$$\tilde{q}^n(x, t_n) = \begin{cases} q_i^n, & \text{if } x < x_{i+1/2} \\ q_{i+1}^n, & \text{if } x \geq x_{i+1/2}. \end{cases} \tag{1.33}$$

Since the extrapolated fluid quantities must be conserved according to:

$$\frac{\partial}{\partial t} \tilde{q}^n + \frac{\partial}{\partial x} f_{\tilde{q}^n} = 0, \tag{1.34}$$

the discontinuities at each cell interface define a Riemann problem. This Riemann problem can be solved exactly, which then allows the construction of the flux across the cell interface and provides a natural shock-capturing scheme. We illustrate the piecewise extrapolation of fluid quantities and the ensuing Riemann problem in Fig 1.9. Since it utilises piecewise constant extrapolation, Godunov's method only yields first-order accuracy, thus, higher-order schemes are often preferred, such as the piecewise parabolic method (PPM, Colella & Woodward 1984). Additionally, the slopes of the polynomials used to interpolate the fluid quantities are arbitrary and may introduce oscillations, so the implementation of a slope-limiting scheme is often necessary for first-order methods to avoid nonphysical effects. Once the fluxes are computed at the cell interface, the new fluid quantities q_i^{n+1} are updated by inserting the new fluxes in equation 1.31. Overall, the finite-volume method is divided into three steps: first, the initial values of the fluid quantities at the cell boundaries are estimated as piecewise polynomials, then the ensuing Riemann problem is solved to construct the fluxes across each cell, which are then finally used to update the fluid quantities.

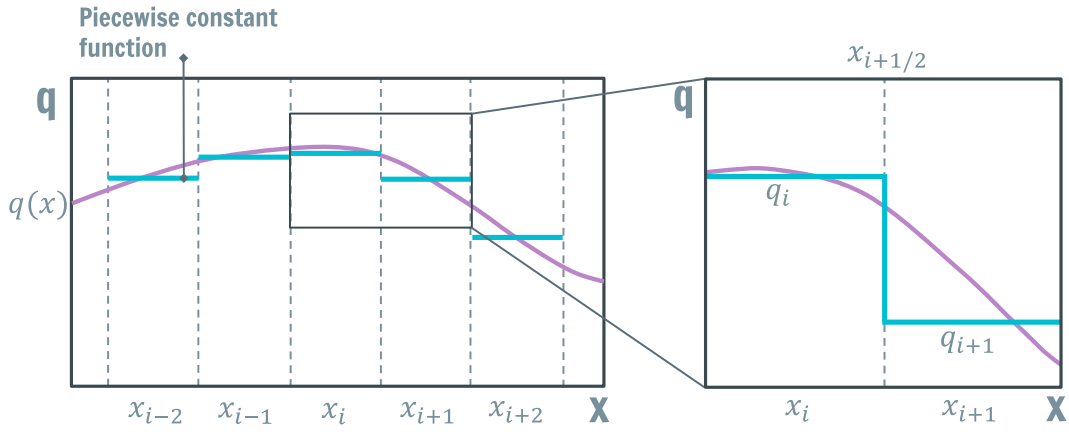

Figure 1.9: Construction of the flux of a fluid quantity q in the finite-volume method on a grid of N cells using Godunov's method. Grid cells are indicated as x_i with $i \in [0, N-1]$, the continuous form of the quantity $q(x)$ is shown as a purple line, and the piecewise constant extrapolation is shown as blue lines. Left: general view of the extrapolation. Right: zoom in on a cell interface $x_{i+1/2}$ and the discontinuity formed at the boundary. Solving the Riemann problem formed by the different values of the discretised q(x) on each side of the boundary allows to compute the flux across the cell interface.

Boundary conditions

An important specificity of grid-based discretisation schemes is that they require boundary conditions at the edges of the grid. These conditions are typically imposed through the use of ghost cells, which are set around the boundary of the domain to update the cells at the edge of the grid, since otherwise they would have no neighbours in one direction and could not be updated according to the discretisation scheme. The content of these ghost cells is set at each timestep, independent of the integration scheme, according to the physical type of boundary set for the problem at hand. There are many types of boundary conditions relevant to different physical problems, the main ones used in computational astrophysics are:

- Periodic boundary: the fluid solution is a periodic function of the domain. If we consider the fluid quantities on the edge cells on the opposite sides of the grid, q_0^n and q_N^n, then the state of the ghost cell q_{-1}^n which is used to find q_0^{n+1} is set to the same value as q_N^n.

- Outflow boundary: allows material to flow out of the domain but prevents waves from entering from this boundary. This is typically done by extrapolating fluid quantities from edge cells to ghost cells and computing fluxes at the boundary.

- Inflow boundary: allows material to flow in by imposing velocities in the ghost cells pointing towards the domain.

- Reflecting boundary: used to impose solid surfaces or symmetry axes by reflecting the fluid quantities of edge cells into the ghost cells.

Applications

Finite-volume methods are broadly used across all fields of astrophysics, mostly because they are more versatile than particle-based methods while having better energy conservation than other grid-based methods. The grid discretisation is well-suited to include most physical processes, and the natural presence of boundary conditions allows to easily excise or approximate part of the physical domain to focus on specific processes at a lower cost. These methods can also reach a high level of accuracy, allowing the resolution of steep gradients, and the implicit numerical diffusion from the reconstruction schemes allows for satisfactory treatment of discontinuities and turbulence in the fluid. They are thus more appropriate to study small-scale instabilities than particle-based methods, although it generally comes at a significant cost. The high cost of grid-base simulations is typically alleviated through the refinement of the grid, which allows for the study of the regions of interest at optimal resolution while simulating the areas of low interest at a reasonable cost. In particular, schemes that temporarily refine the mesh allow for major improvements in the accuracy-to-cost ratio. This is commonly achieved by using adaptive mesh refinement (AMR, Berger & Oliger 1984; Berger & Colella 1989), which locally and temporarily adapts the grid spacing to finer cell sizes according to criteria set by the user. The ability to refine and de-refine a mesh permits, for instance, to resolve with high accuracy a travelling shock wave without needing a constant finer mesh along its predicted path. While AMR and other refinement methods can significantly decrease the cost of grid-base simulations, they also add a layer of complexity to the simulation structure, increasing the potential sources of error. Furthermore, the cost of adaptively refined simulations remains high, which constitutes a major drawback when simulating fluids on large dynamical ranges. In such cases, the grid resolves a considerable amount of empty or relatively low-density space at a high cost, which can still be very costly despite using a coarser mesh. Thus, grid-based methods are generally limited in domain-to-cell size ratio and can become unreasonably expensive for simulations of stellar mergers or galaxy formation. Other, maybe less significant, disadvantages of grid-based methods include the potential kinks and artificial symmetries in the fluid due to the mesh. These grid artefacts may significantly affect the fluid in non-physical ways and thus should be kept under control. Finally, computational limitations mean that there will always be small numerical errors, and thus it is simply impossible to simulate a real vacuum on a grid. Grid-based methods therefore require setting up a pseudo vacuum, or "fluff", based on numerical or physical considerations in regions where a real vacuum is expected. This requirement may be seen as an advantage, for instance, stars do not evolve in a perfect vacuum and this pseudo-vacuum can be set to be physically closer to the reality of stellar environments. Moreover, stellar interiors are often hard to keep in HE since it is not possible to resolve the tail of the density and pressure gradients at the surface, and thus the pseudo-vacuum may be used to help with hydrodynamic stability when simulating stars.

1.4.4 Beyond hydrodynamics

Equations 1.15 and 1.17 describe only ideal hydrodynamics, but the ideal fluid approximation is often too far from the reality of stellar environments. It is thus often necessary to improve the accuracy of astrophysical models to include more physical processes that are relevant to stellar environments. Of course, this generally increases

the complexity of the simulations and requires additional numerical schemes to solve the new equations. A detailed review of these implementations is beyond the scope of this work, instead, we broadly discuss the most relevant processes and the challenges of their numerical treatments. Different changes to the ideal fluid approximations can be made depending on the problem at hand. For instance, viscosity has to be included in accretion disc simulations, in which case a viscous stress tensor is added to the momentum and energy equations. It is also possible to extend the hydrodynamics equations to special relativistic hydrodynamics in scenarios where parts of the fluid are expected to move with velocities close to the speed of light (e.g., relativistic jets). One may even wish to couple the Einstein equations to the hydrodynamics equations to take into account general relativistic effects around compact objects, which is especially relevant for simulations of neutron star mergers. When investigating stellar atmospheres and winds, chemical reactions can be accounted for by supplementing the hydrodynamics equations with the relevant chemical reaction networks. In the case of stellar interactions, the most relevant processes to include are gravitational forces, interactions with radiation fields, and possibly electric and magnetic fields. Nowadays, it is fairly common for hydrodynamics codes made for astrophysics to include a treatment of Newtonian gravity. Gravitational forces appear as a source term in the momentum equation of hydrodynamics, such that it becomes:

$$\frac{\partial(\vec{v})}{\partial t} + \vec{v} \cdot \nabla \ \vec{v} + \frac{\nabla p}{\rho} = \nabla\phi, \tag{1.35}$$

in the Eulerian form, where ϕ is the gravitational potential. The specific energy of the system is also modified to include gravitational energy and becomes $e = u + v^2/2 + \phi$. ϕ can describe the potential of an external source excluded from the computational domain or the self-gravity of the fluid, and it must satisfy the Poisson equation:

$$\nabla^2\phi(\mathbf{x}) = 4\pi G\rho(\mathbf{x}). \tag{1.36}$$

A natural approach to the calculation of ϕ for a fluid element (particle or cell) within a self-gravitating fluid is to do a direct summation of the contributions of all the other fluid elements, but this method requires $O(N^2)$ operations for N particles which makes it extremely expensive. To speed up the calculation, one can group close fluid elements (particles or cells) to treat them as one source. This can be achieved through the use of tree algorithms (e.g., Barnes & Hut, 1986), which decompose the domain as a tree, allowing to approximate the gravitational interaction as a combination of short and long-range interactions and reduce the cost of the force calculation to $O(N \log N)$. Short-range interactions can then be computed as direct summations, while long-range interactions are approximated using multipole expansions. Tree-based solvers are particularly compatible with SPH methods because their neighbour search can be done through the same algorithm. There are other types of Poisson solvers, for instance, based on solving the continuous form of the Poisson equation by applying Fourier transforms or multipole expansions, depending on the boundary conditions and matter distribution. It is also common for grid-based codes to use multigrid solvers, which are relaxation methods that achieve faster convergence by coarsening the grid. We note that while it is important in astrophysics in general, self-gravity is not always the most relevant process in astrophysical problems and the cost of computing self-gravity might not be compensated by the higher realism. This is especially true in situations where the self-gravity of the fluid is negligible compared to some external influence, e.g.,

accretion discs surrounding compact objects, in which case computational resources are better spent on other issues such as magnetic fields or relativistic effects. Aside from gravity, an important aspect of the evolution of gas in stellar environments is its interaction with the surrounding radiation field: the absorption or emission of radiation can increase or decrease the temperature and pressure of the gas, while the density and temperature of the gas affect the transport of the radiation. This is particularly important when modelling the radiation from accretion discs or energy transport inside stars, which is relevant for thermal readjustments of the donor during stable mass transfer and possibly CEE Ricker et al. (2018). Additionally, including a treatment of radiation transport in a model allows to obtain theoretical predictions that can be directly compared to observations, such as synthetic light curves or spectra. To model the interactions between gas and radiation, one needs to couple the equations of ideal fluid dynamics to the equations of radiation transfer to obtain the radiation hydrodynamics (RHD) equations. The equations of radiative transport define how photons are scattered, absorbed, and emitted by the gas, which drastically increases the dimensionality of the problem by introducing many new quantities that strongly depend on local densities and the wavelength of the radiation. RHD thus requires a lot more computational resources than ideal hydrodynamics, both in terms of memory and computational power, and is challenging to implement. The choice of implementation depends on the problem at hand, for instance, low optical depth environments, such as stellar winds (e.g., Townsend, 2009), may be well modelled by approximating the coupling of radiation and matter with a radiative cooling term. On the other hand, radiation transport in optically thick environments may be approximated as a diffusion problem by taking the 0^{th} moment of the radiative transfer equation. In such cases, the most common RHD scheme is flux-limited diffusion (Levermore & Pomraning, 1981), which includes a limiter to prevent signals from propagating faster than the speed of light. More complicated methods are required to accurately treat both high and low optical depth regions in the same model, for instance, one may include higher-order moments of the radiative transfer equation (e.g., Gnedin & Abel, 2001; Hayes & Norman, 2003). Other possible methods include using Monte Carlo schemes to discretise the radiation field in packets and propagate them stochastically through the medium (e.g., Lucy, 2005), or using ray-tracing to solve the radiative transfer equation along characteristic rays that cross the domain (e.g., Razoumov & Scott, 1999). Finally, the fluid approximation also neglects the presence of electric and magnetic fields, which are especially important for accretion discs and systems containing highly magnetised stars. Adding a treatment of magnetic fields requires coupling the hydrodynamics equations to Maxwell equations to obtain the equations of magnetohydrodynamics (MHD), most often assuming perfect conductivity (i.e., no electrical resistance) to describe ideal MHD. MHD schemes are based on regular hydrodynamics solvers, with a few subtleties introduced by the magnetic field. One of the main difficulties comes from the physical condition $\nabla \cdot \vec{B} = 0$ that arises from the induction equation (solenoidality of the magnetic field). Since this is only an initial condition, solving the MHD equations does not guarantee that the condition will remain true, potentially yielding unrealistic effects such as the formation of magnetic monopoles. Thus, a divergence-free magnetic field has to somehow be enforced after solving the MHD equations. This can be achieved through different schemes, which depend on the type of discretisation of the simulation. For grid-based codes, three main methods yield satisfactory results. Constrained transport defines the magnetic field on the faces of the

mesh, which is then calculated using the sum of the electric field on the edges of the cell face while naturally retaining a divergence-free magnetic field down to machine precision if it is introduced as an initial condition (e.g., Evans & Hawley, 1988). The projection method solves a Poisson equation to project the magnetic field newly obtained from the MHD solver onto the initial field satisfying $\nabla \cdot \vec{B} = 0$ (Brackbill & Barnes, 1980), and the 8-wave scheme adds extra source terms to the MHD equations (Powell, 1994). For particle-based methods, maintaining a divergence-free field is done through divergence cleaning, which enforces $\nabla \cdot \vec{B} = 0$ by removing or dissipating energy (e.g., Tricco & Price, 2012).

1.5 Summary of the results

The goal of this thesis is to study various types of binary interactions to constrain new and existing models by analysing photometric and spectroscopic observations as well as performing hydrodynamics simulations. Each chapter of this thesis is centred around a different type of binary interaction, aiming to explore known issues in binary and stellar evolution.

Cataclysmic variables and thermally unstable accretion discs

Chapter 2 is dedicated to CVs, and more specifically the peculiar system OGLE-BLG504.12.201843 (O-201843), which is a peculiar CV exhibiting year-long outbursts with an average recurrence period of 973 days. This study aimed to characterise this system and the origin of these outbursts by performing a thorough analysis of existing optical photometry and new optical spectroscopy. After investigation of the orbital variability of the system across the outburst cycle, we find that the outbursts likely originate from a thermally unstable accretion disc, suggesting that O-201843 is a DN with extreme properties. Additionally, the shape of the outbursts indicates that this system is likely a U Gem type DN. Beyond the unusual length of the outburst cycles, the photometry of O-201843 shows two uncommon features in DNe: a slow brightening of 0.75 mag in the I band over a period of 600 days preceding the outbursts, and small flares with amplitude $\lesssim 0.2$ mag in I band detected during quiescence. We suggest that the flares correspond to small outbursts that fail to propagate throughout the disc, while we attribute the pre-outburst brightening to a slow rise in temperature, which is predicted by the disc instability model despite being rarely observed. In the spectra of the system, we find Balmer absorption lines that may either come from an early F secondary or the accretion disc. We do not find any signatures of the accreting WD, nor do we observe the usual features of a thermally unstable accretion disc: there are no emission lines or cores in quiescence and no new Balmer absorption lines in outburst. We interpret the lack of typical disc signatures as unusually low disc temperatures, indicating weak or absent irradiation of the disc by the WD. During the outburst, the spectra show emission lines, though they lack the double-peaked profile expected from accretion discs, favouring a low inclination of the system. We found that the DN V1129 Cen be similar to O-201843, as it has a similar orbital period and location in the HR diagram, but significantly smaller outburst cycle length and amplitude. O-201843 might not be a DN and instead, be the prototype of a new type of CV that possesses thermally unstable accretion discs like DNe. To further characterise this system, it would be ideal to obtain time-resolved spectroscopy of the system. This would help

to understand the lack of double-peaked signals from the disc and accurately constrain the mass ratio and inclination of the system, and possibly get insights into the nature of the primary and secondary stars. Due to its numerous peculiarities, O-201843 provides important tests to our current knowledge on thermal-viscous instabilities and outbursts in accretion discs and is a great target for studies of CVs and DNe.

Asymmetric winds in red supergiant stars

In Chapter 3, we investigate asymmetric winds around red supergiant (RSG) stars and the potential role of binary interactions in driving such winds. This study introduces a new scenario in which a companion on an eccentric orbit grazes the envelope of a RSG at periastron. At each periastron passage, the companion ejects part of the outer envelope, which radiatively cools, eventually reaching adequate conditions for dust condensation and dust-driven winds. To study this scenario, we perform 3D SPH simulations of a $2\,M_\odot$ star on a highly elliptical orbit around a $20\,M_\odot$ RSG with an envelope extending to $1500\,R_\odot$ such that the companion grazes the surface of the RSG at periastron. These simulations are performed with the code Phantom and are meant as proof-of-concept, thus, we use simple treatments for radiative cooling and dust-driven winds to maintain reasonable computational expenses. Our models show that each periastron passage ejects gas from the outermost envelope, which later results in a dense semi-circular outflow. Furthermore, each consecutive grazing interaction decreases the orbital period by $\sim 3-4$ years, resulting in a smaller periastron distance which enhances the mass loss during subsequent interactions. Thus, the density and frequency of the outflows increase as the system evolves, and the mass of the outflows grows from $3\times10^{-4}\,M_\odot$ during the first orbit to $\sim 10^{-2}\,M_\odot$ when the system enters CEE after 13 orbits (~200 years). We stop our simulations after 14 orbits, at which point the total ejecta mass is about $0.185\,M_\odot$ spreading beyond $r \gtrsim 1000$ au from the system, with 80% of this mass situated in the innermost region ($r \lesssim 100$ au). The final ejecta is strongly asymmetrical, with a clear shell-like structure born from the shocks driven by the grazing interaction. We cannot resolve the evolution of our system beyond this point, and thus the outcome of the CEE phase is uncertain: it may result in either a merger or a short-period binary. The initial conditions of our system may seem rather uncommon, especially with such high eccentricity, but we find that there are several evolutionary pathways leading to this scenario. The binary may be composed of a massive MS star and a low-mass MS companion on a relatively large and eccentric orbit that started interacting when the massive star stopped burning Hydrogen. Alternatively, we find that the typical evolution channel for double NS binaries allows for the formation of an eccentric binary with an evolved RSG and a NS companion. This grazing interaction should produce several observable signatures, for instance, the dusty ejecta should be observable at millimetre/sub-millimetre wavelengths, and the rich chemistry in the outflows should yield observable molecular lines. Furthermore, the accretion from the companion is expected to yield X-ray emission or highly ionised lines, especially in the case of a NS companion. We compared our simulations with observations of the ejecta surrounding the RSG VY CMa and found that the grazing interaction may be the cause of an increase in mass loss that occurred about 1000 years ago, or it may be the origin of recent 100 year-old ejections. In particular, some of these recent outflows resemble the results of our simulations, however, the grazing interaction is insufficient to explain the complex morphology of the surrounding outflows, which require the interplay of multiple processes such as magnetic activity, convection, and pulsations. Since our

simulations were only meant as a proof of concept and were performed using simple implementations of radiative cooling and winds in the outflows, we plan to incorporate more accurate prescriptions in follow-up studies. By increasing the accuracy of our simulations, we will be able to study the morphology of the outflows in greater detail and produce synthetic observables that will provide a strong test for our hypothetical scenario. We can also add more physical processes, such as convection, to study the interplay between the grazing interaction and other relevant outflow mechanisms.

Accounting for previous binary evolution in common envelope evolution

Finally, Chapter 4 is centred around common envelope evolution and how it may be impacted by previous phases of binary evolution. In particular, we study the effect of a previous phase of mass transfer where the accretor later becomes the donor of a common envelope phase. Such an accretor undergoes several changes to its stellar structure: new material is added to its outer layers, increasing the steepness of the density profile in the envelope, and its core undergoes a rejuvenation process. The rejuvenation process is particularly interesting because it lowers the binding energy of the layers surrounding the stellar core, which may then ease the unbinding of the envelope during common envelope evolution. We aim to study this effect through 3D hydrodynamics simulations where we investigate the dynamical inspiral of the common envelope evolution of an 18 $M_\odot$ red supergiant and a 1.4 $M_\odot$ companion. We perform two sets of simulations with rejuvenated and non-rejuvenated donors with the AMR grid-based code FLASH4.5, and compare the results to characterise the effect of the rejuvenation on the outcome of the common envelope phase. We find that the past phase of mass transfer does impact the speed of the inspiral, the amount of unbound mass, and the shape of the ejecta. The main consequence of the previous phase of mass transfer is a decrease in the duration of the inspiral phase by a factor of two due to the denser outer layers of the rejuvenated donor, which increases the gravitational drag exerted on the companion. We also found that the orbit of the binary does not stabilise in both rejuvenated and non-rejuvenated cases, though this result is bound to the resolution of our simulations and may change with a resolution increase. The impact of rejuvenation on the mass loss of the system is less evident, mostly because the unbinding efficiency of the system is overall very low, with up to 6% and 8% of the envelope mass ejected in the rejuvenated and non-rejuvenated cases, respectively. We still found a difference in ejection efficiency, though different unbinding criteria yield very different results: there is a 50% increase in unbound mass with the rejuvenation when considering only the gravitational and kinetic energy of the gas, but a 25% decrease when including the internal energy of the gas. Finally, the two sets of simulations show a significant difference in the final morphology of the ejecta. We found that the rejuvenated ejecta is more concentrated around the equatorial plane, and overall more spherically asymmetric than its non-rejuvenated counterpart. This change mostly impacts observations of future transients arising from the merger of the binary, for instance, the luminous red nova arising from the merger or a later supernova explosion of the merger product will interact with the circumstellar medium, thus their light curve will likely change with the mass distribution of the ejecta.

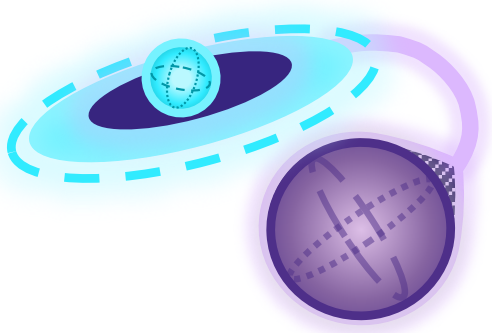

2. OGLE-BLG504.12.201843: A possible extreme dwarf nova [1]

Camille Landri, Ondřej Pejcha, Michal Pawlak, Andrzej Udalski, Jose L. Prieto, Manuel Barrientos, Jay Strader and Subo Dong

Monthly Notices of the Royal Astronomical Society, Volume 517, Issue 2, December 2022, Pages 2746–2756

Abstract

We present the analysis of existing optical photometry and new optical spectroscopy of the candidate cataclysmic variable star OGLE-BLG504.12.201843. As was shown previously, this object has an orbital period of 0.523419 days and exhibits year-long outbursts with a mean period of 973 days. Using digitized photographic archives, we show that the earliest recorded outburst occurred in 1910. We propose that this object is a U Gem-type dwarf nova with extreme properties. The orbital variability of the system in outburst shows clear signs of an accretion disc, from which the outburst likely originates. During quiescence, the object slowly brightens by up to 0.75 mag in the I band over 600 days before the outburst and exhibits small flares with amplitude $\lesssim 0.2$ mag in the I band. We interpret the gradual brightening as an increase in the luminosity and temperature of the accretion disc, which is theoretically predicted but only rarely seen in DNe. The origin of small flares remains unexplained. The spectra shows Balmer absorption lines both in quiescence and outburst, which can be associated with a bright secondary star or a cold accretion disc. During outbursts, emission lines with FWHM of about 450 km s^{-1} appear, but they lack typical double-peaked profiles. We suggest that either these lines originate in the disc winds or the orbital inclination is low, the latter being consistent with constrains obtained from the orbital variability of the system. Due to its extreme properties and peculiarities, OGLE-BLG504.12.201843 is an excellent object for further follow-up studies.

[1]This chapter is a pre-copyedited, author-produced version of an article accepted for publication in Monthly Notices of the Royal Astronomical Society following peer review. The version of record [Camille Landri, Ondřej Pejcha, Michal Pawlak, Andrzej Udalski, Jose L. Prieto, Manuel Barrientos, Jay Strader and Subo Dong. OGLE-BLG504.12.201843: a possible extreme dwarf nova. MNRAS Volume 517, Issue 2, December 2022, Pages 2746–2756] is available online at https://doi.org/10.1093/mnras/stac2864

2.1 Introduction

OGLE-BLG504.12.201843 (hereafter O-201843) is a candidate cataclysmic variable discovered by Mróz et al. (2015) with the *Optical Gravitational Lensing Experiment* (OGLE, Udalski et al. 2015) in the field BLG504.12 and is located at RA=17:57:19.65, Dec.=-28:08:15.7 (J2000). Mróz et al. (2015) found that O-201843 undergoes 300-days long outbursts that repeat every 950 to 1020 days. The outburst amplitude is 1.75 mag in the *I* band. Mróz et al. (2015) also detected a photometric variability with a period of 0.523419 days, which they interpret as the orbital period. In quiescence, the orbital light curve has a double-hump profile, but as the system gets brighter the minima change shape and depth. At maximum brightness, the orbital light curve shows a single hump. Additionally, Mróz et al. (2015) noticed an initially very slow brightening to the maximum, which abruptly accelerates. They speculated that the long cycles are caused by interactions with a tertiary star, but no sign of tertiary orbit was detected in the O-C analysis. Overall the photometry of the system is reminiscent of dwarf novae (DN), albeit with extreme properties. Motivated by these intriguing features and especially the slow rise from the quiescence, we selected O-201843 for more detailed analysis. If O-201843 indeed is a DNe, studying its extreme properties could lead to a better understanding of the mechanisms responsible for DN outbursts.

DNe are a type of CVs that undergo semi-periodic outbursts (Warner, 2003b). These systems are composed of a White Dwarf (WD) accreting matter from a secondary star, typically located on the main sequence. The accreting material forms a disc, which can become thermally unstable and develop outbursts. Some DNe only undergo regular 2-5 mag outbursts (U Gem type) while others display additional features. Examples of these features are longer and less recurrent outbursts called superoutbursts (SU UMa type) or standstills that interrupt a sequence of outbursts (Z Cam type).

The outbursts of DNe are currently best explained by the Disc Instability Model (DIM, e.g. Meyer & Meyer-Hofmeister, 1981; Smak, 1982; Cannizzo et al., 1982; Faulkner et al., 1983; Mineshige & Osaki, 1983). This model is based on a Shakura-Sunyaev disc (Shakura & Sunyaev, 1973) supplemented with additional physical processes, such as mass transfer variations, inner disc truncation, disc winds and irradiation of the disc, which have been reviewed by Lasota (2001) and Hameury (2020). For such a disc, the effective temperature as a function of the surface density (S-curve) describes cold and a hot stable branches and a viscously and thermally unstable region between them.

In DNe, the disc has local mass transfer rates that lie in the instability range. During quiescence, matter accumulates until the mass transfer reaches the upper critical value and heat fronts propagate both inwards and outwards. The temperature rises until the peak of the outburst, then a cooling front starts propagating from the outside of the disc and the disc goes back to quiescence. The radius at which the heating front starts has an impact on the duration and shape of the outburst. If it starts far from the inner edge of the disc (i.e. the disc is almost stable), the outburst is asymmetrical: the decline is slow at first and then accelerates to reach values similar to the rise. This outside-in outburst involves a large part of the mass of disc. Alternatively, the heating front can develop close to the inner edge of the disc, which leads to more symmetric outburst shapes. One prediction of the DIM is the critical mass transfer rate that separates DNe and Nova-like CVs which seems to match the observations (Dubus et al., 2018).

DN outbursts are never strictly identical because there are differences in parameters

that control the outburst, such as the radius at which the outburst is triggered, the distribution of material after the last outburst, among others. However one can find correlations between some of the characteristics of the outbursts. The two most probable relations are the Kukarkin-Parenago relation between the amplitude and the average recurrence time of outbursts (Kukarkin & Parenago, 1934) and the Bailey relation between the rate of brightness decay and the orbital period (Bailey, 1975). Recently, Otulakowska-Hypka et al. (2016) presented a statistical analysis of the measurable properties of a large sample of DNe outbursts in order to find possible correlations between the different characteristics. They were not able to verify the Kukarkin-Parenago relation but confirmed the Bailey relation as well as other connections, e.g. the correlation between outburst duration and orbital period.

In this paper, we aim to better constrain the nature of O-201843 by analyzing its optical photometry and spectroscopy. In Section 2.2, we describe our photometric and spectroscopic dataset. In Section 2.3, we discuss the different features of the system. In Section 2.4, we speculate about the origins of these features, compare O-201843 to DNe and try to find similarities that would allow to characterise the system. In Section 2.5, we summarize our results.

2.2 Observations

2.2.1 Photometry

In Figure 2.1, we show available optical time-series measurements of O-201843. We use I band observations from OGLE, which cover 2001–2021. The data up to year 2015 were published by Mróz et al. (2015), the later data are presented here for the first time. As seen in Figure 2.1, the system was irregularly observed between 2001 and 2009 and then monitored from 2010 to 2019 at a roughly regular 1-day cadence with several interruptions. A total of six bright outbursts were recorded, with a recurrence timescale of roughly 1000 days. The system has a brightness of $I = 15$ mag in quiescence and peaks at $I = 13.25$ mag during the outbursts; we discuss the outburst properties in Section 2.3.1. From the photometric variability of the system, Mróz et al. (2015) detected an orbital period of 0.523419 days, we discuss the orbital variability in Section 2.3.2. We see in the left panel of Figure 2.1 that small $\Delta I = 0.2$ mag flares appear during quiescence, a feature that was not discussed by Mróz et al. (2015). We provide more details on the flares in Section 2.3.3.

Additionally, we looked for archival data from the Digital Access to a Sky Century @ Harvard (DASCH) catalog (Laycock et al., 2010). The DASCH project digitizes plates from the Astronomical Photographic Plate Collection and converts them to photometry, allowing the study of the sky on 100 years timescales. Observations from photographic plates roughly correspond to B band photometric measurements. We found a total of 154 detections made between 1903 and 1951 which are shown in the top panel of Figure 2.1 along with the non-detections. The system displays five distinguishable peaks in 1911, 1940, 1943, 1948 and 1950, showing that this system has gone through these outbursts in the past. The time elapsed between the outbursts seems to roughly match the periodicity of the recent observations. The peak magnitude of the outburst averages around 14 mag but one peak goes up to 11 mag, however, we do not know if this peak was extraordinary or if the other peaks were only partly recorded.

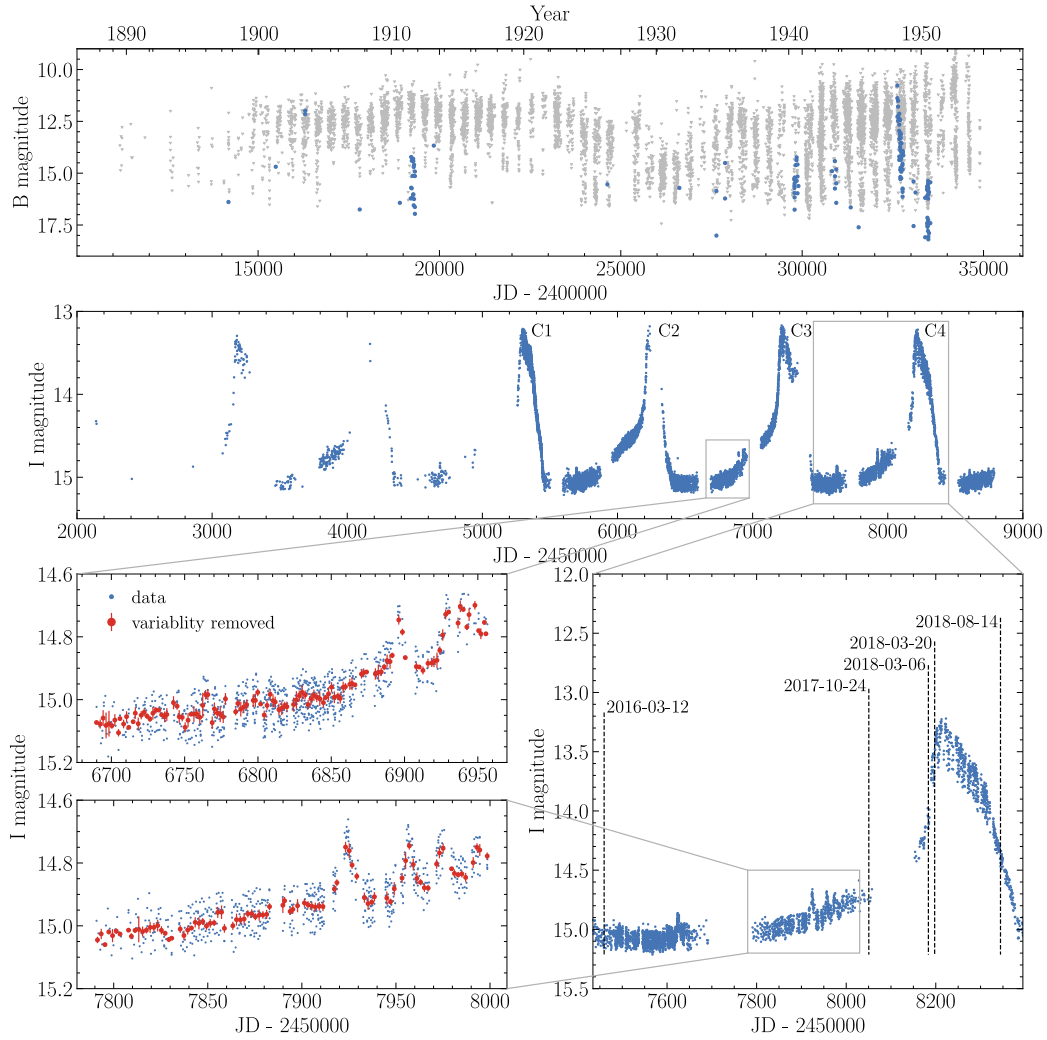

Figure 2.1: Photometry of OGLE-BLG504.12.201843. The first panel shows data from DASCH, with detections in blue and non-detections in grey. The middle panel shows data from OGLE, we denote the cycles of interest as C1, C2, C3 and C4. The right panel shows one outburst cycle with dates at which spectra were obtained, which correspond to three out of the four phases of the light curve. The left panels show the small flares appearing in OGLE data in more details. The data is shown in blue and the phase-averaged brightness is shown in red. The latter was obtained by subtracting a fit of the variability (made with with Fourier series) from the data and averaging the result over bins of 2 days (in red).

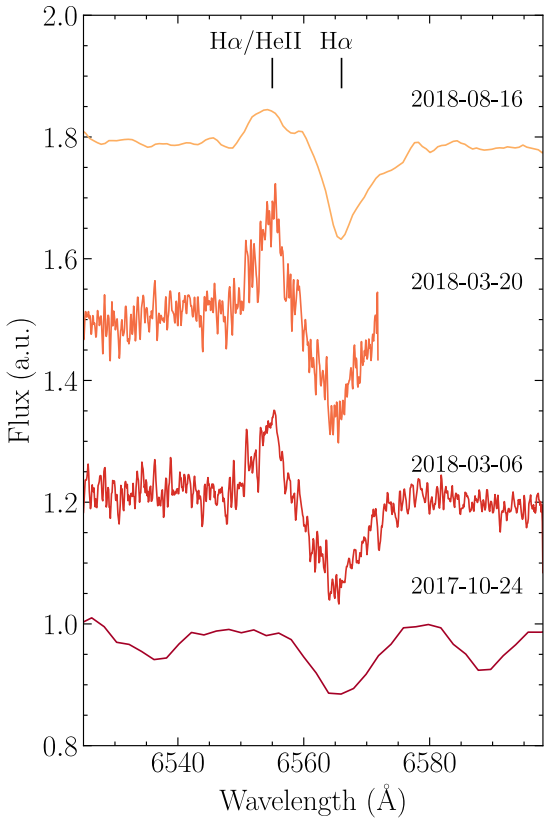

Figure 2.2: Evolution of the Hα absorption line and the 6560 Å emission line at different epochs. The spectrum taken on the 2017-10-24 corresponds to the quiescence of the system while the three other spectra were taken during an outburst.

2.2.2 Spectroscopy

We obtained six spectra of O-201843 between March 12 2016 and August 14 2018. To our knowledge, these are the first spectra of O-201843. Four spectra are Echelle spectra and were taken with the MIKE Spectrograph on the Clay telescope at the Las Companas Observatory (LCO). The two others were obtained with the Goodman High Throughput Spectrograph at the Southern Astrophysical Research Telescope (SOAR) (see Table 2.1). The bottom right panel of Figure 2.1 shows when the spectra were taken in the context of the outbursts. Two spectra were taken during the quiescence of the light curve, three during the rise and the last one during the decline. The data were reduced using IRAF and after removal of the continuum we performed Gaussian fits on the well-defined lines. The results are listed in Table 2.2 and the evolution of the most prominent feature is shown in Figure 2.2. Larger portions of our spectra with lines identified in Table 2.2 are shown in Appendix 2.5.

Table 2.1: Log of spectroscopic observations of O-201843.

Time of observation		telescope	instrument	wavelength coverage	spectral resolution	observer	reduction
Date	Time (UT)			(Å)			
2016-03-12	10:08	Magellan	IMACS	3650-9740		Dong, S	Prieto, JL
2017-10-24	00:22:03	SOAR 4.1m	Goodman Spectrograph	3200-9000	1850	Strader, J	Strader, J
2017-10-24	00:22:03	SOAR 4.1m	Goodman Spectrograph	3200-9000	1850	Strader, J	Strader, J
2018-03-06	13:52:22	Magellan	MIKE-Blue	3350-5000	83000	Barrientos, M.	Prieto, JL
2018-03-06	13:52:25	Magellan	MIKE-Red	4900-9500	65000	Barrientos, M.	Prieto, JL
2018-03-20	13:51:00	Magellan	MIKE-Red	4900-9500	65000	Barrientos, M.	Prieto, JL
2018-08-14	02:41:27	SOAR 4.1m	Goodman Spectrograph	3200-9000	5880	Strader, J	Strader, J

Table 2.2: Most prominent spectral lines of O-201843 and their evolution. The parameters of each lines are obtained by fitting a Gaussian profile.

Date	Wavelength	Line	Type	FWHM		Eq. Width
	(Å)			(Å)	(km/s)	(Å)
2016-03-12	6557.8	Hα	Absorption	10.61 ± 1.25	485 ± 57	3.77 ± 0.45
2017-10-24	4342.7	Hγ	Absorption	7.90 ± 1.31	545 ± 90	2.41 ± 0.38
	6565.9	Hα	Absorption	9.63 ± 1.63	440 ± 74	1.11 ± 0.18
2018-03-06	4341.3	Hγ	Absorption	8.05 ± 0.19	556 ± 13	1.52 ± 0.04
	4680.3	HeII - 4686	Emission	7.02 ± 0.82	450 ± 53	1.21 ± 0.19
	4862.8	Hβ	Absorption	7.56 ± 0.19	466 ± 11	1.32 ± 0.03
	6554.2	HeII - 6560 or Hα	Emission	5.21 ± 0.89	238 ± 41	0.71 ± 0.11
	6565.8	Hα	Absorption	8.47 ± 0.61	387 ± 28	1.37 ± 0.10
2018-03-20	6554.2	HeII - 6560 or Hα	Emission	6.34 ± 0.42	290 ± 19	0.94 ± 0.06
	6565.5	Hα	Absorption	7.24 ± 0.33	331 ± 15	1.07 ± 0.05
2018-08-14	6554.1	HeII - 6560 or Hα	Emission	5.81 ± 1.7	266 ± 77	0.37 ± 0.09
	6567.2	Hα	Absorption	8.59 ± 0.4	392 ± 18	1.36 ± 0.06

2.3 Results

In this Section, we examine the photometric and spectroscopic features of O-201843. We discuss the outburst shapes and periodicity in Section 2.3.1 and study the evolution of the phased light curves during the outbursts in Section 2.3.2. In Section 2.3.3, we look at the newly identified flares. Finally we investigate the spectroscopy and its evolution during the outbursts in Section 2.3.4.

2.3.1 Outbursts

We first investigate the general shape of the outburst cycles. The middle panel of Figure 2.1 shows the six outbursts that were recorded during the 18 years of observation. They are not strictly periodic but happen approximately every 1000 days and they display a 1.75 mag increase in the I band. Looking at the right panel of Figure 2.1, we estimate the outburst duration to be around 300 days. We also see an intermediate state where the luminosity slowly increases by about 0.75 mag before the outburst starts, i.e. almost half of the total luminosity increase of the system. We choose to consider it as a part of the quiescence of the system, which makes the low state 700 days long. In order to investigate the periodicity of the outbursts we performed an $O - C$ analysis of the light curve. The maxima of outbursts were obtained using spline fits of the light curve. We improved the average period obtained from this analysis by correcting it with the change in period and reapplying the $O - C$ fit, until this change becomes negligible. This yields an average recurrence time of $P_{\rm cycle} = 973.16$ days. We checked the timings of maxima from OGLE data and we did not find any significant trend. Unfortunately, the data from DASCH are too sparse to allow meaningful fits of maxima.

To check if the shape of the outburst evolves, we fold the light curve over the recurrence time using

$$JD = 2451601.62 + 973.16 \times E, \tag{2.1}$$

where E is the epoch. We show the results in Figure 2.3 and we see that the shape of the outburst does not change significantly from one cycle to another. This is emphasised by the consistence of the rise and decline rates throughout the cycles. In fact, the outbursts show slow and fast decline rates that remain around 0.006 and 0.014 mag/day, while the quiescence and outburst rise vary between 0.0017 to 0.0019 mag/day and 0.016 to 0.021 mag/day, respectively.

2.3.2 Orbital variability

Following the orbital period found by Mróz et al. (2015) (0.523419 day), we show the evolution of the orbital variability of the system in Figure 2.4. This was obtained by fitting the general trend of the light curve using splines and subtracting the fit from the data. The result is folded over the orbital period following

$$JD = 2452141.23 + 0.523419 \times E, \tag{2.2}$$

and is repeated over two periods for readability purposes. We show the variability of the light curve for 20 orbital periods around the time at which a specific phase of the outburst is reached. These phases correspond to different values of brightness, i.e

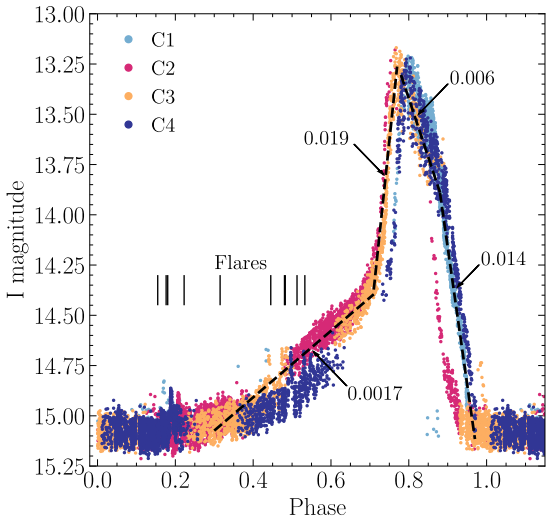

Figure 2.3: Light curve folded over the recurrence of the outburst (973.16 days) using Equation (2.1). We show four cycles which are each denoted by a different colour. We indicate the time at which the flares discussed in Section 2.3.3 were recorded with black vertical lines. The average slopes of the different phases of the cycle are plotted in black with the values (in mag.day^{-1}) indicated next to each phase.

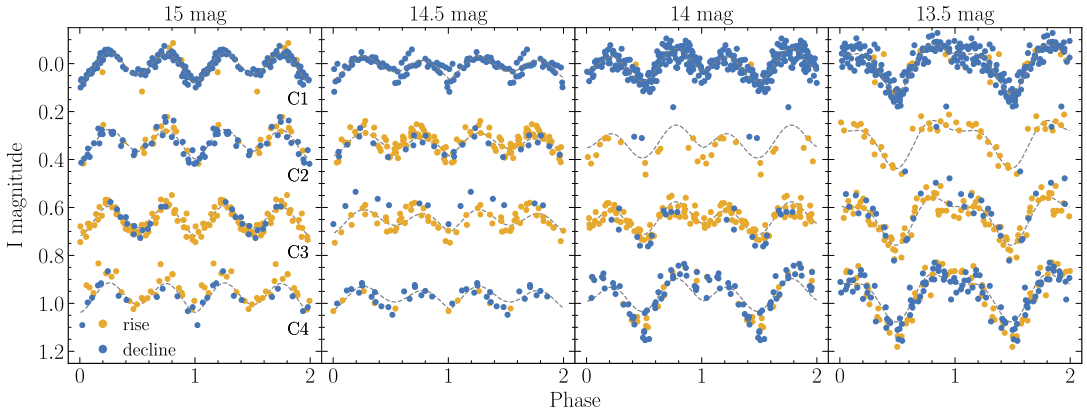

Figure 2.4: Photometry of OGLE-BLG504.12.201843 during cycles C1, C2, C3 and C4 folded around its orbital period (0.523419 days) using Equation (2.2). We separated the data in 4 magnitude bins (15, 14.5, 14 and 13.5 mag) and removed the effect of the outburst on the photometry to single out the orbital variations of the system. We also separate each bin in "rise" and "decline" phases of the outburst, shown in yellow and blue respectively. For each bin, we plot a fit of the cycle with the clearest shape in grey for comparison with the other cycles.

13.5 mag is the peak of the outburst, 15 mag is the low quiescence, 14 and 14.5 mag are intermediate states. The data are also split in rising and declining phases of the light curve in order to evaluate differences in shape. We overplotted a fit of the cycle with the most data for comparison purposes.

As shown by Mróz et al. (2015), the variability shape is different during quiescence and outburst. During quiescence, an orbital period shows two maxima and two minima due to the tidal distortion of the secondary. Additionally, the two minima of the light curve are not equal, which can be caused by different mechanisms. A possible explanation is the irradiation of the secondary by the primary, which brightens the side of the secondary that faces the primary. An other possibility is gravity darkening: the distortion of the secondary lowers the surface gravity on the side that faces the primary, changing the temperature and pressure conditions for hydrostatic equilibrium and darkening of the area (Lara & Rieutord, 2012). This results in the dimming of the side of the secondary that is facing the primary. These ellipsoidal modulations also mean that the secondary star contributes significantly to the observed flux.

During the outburst, the minimum at phase 0.5 becomes deeper and sharper while the minimum at phase 0 is absorbed by the brightness of the outburst. The deeper minima is likely caused by the secondary eclipsing the component of the system from which the outburst originates. The eclipse at phase 0.5 means that the corresponding minimum in quiescence occurs when the back of the secondary is observable and the deeper minimum at phase 0 occurs when we observe the side facing the primary. Therefore, the difference in minima during quiescence seems to be caused by gravity darkening rather than irradiation.

We note that during the second part of the outburst decay, the shape of the variability has already switched back to the quiet state, so the outbursting component is not luminous enough to hide the tidal distortion of the secondary. We also look for changes in the variability between the rise and the decline as well as between different outbursts. We do not find significant differences and conclude that the brightness contribution of the different components of the system does not change from one outburst to the other or from rise to decline.

2.3.3 Flares

Another peculiar feature of O-201843 are the small flares with amplitudes up to $\Delta I = 0.2$ mag appearing during the quiescence which were not discussed by Mróz et al. (2015). They are often barely apparent due to their very small amplitude. The most distinct ones appear in the last outburst recorded, shown in the bottom right panel of Figure 2.1.

The flares last around ten days, and in some instances they recur every five to twenty days in a 100-days interval. To distinguish the flares from the orbital variability, we fitted the orbital variations using third order Fourier series and subtracted the fit from the light curve. We averaged the result over bins of two days to remove the scatter of the data around the fit. This method confirmed ten flares, which are indicated in Figure 2.3, and some of the light curves are shown in detail in the bottom left panels of Figure 2.1. Some flares are too hard to unambiguously identify because the observations are too sparse and the flare amplitude is comparable to the variability of the system. Additionally, they seem to only occur during quiescence, which is unfortunately never fully covered due to occultation by the Sun. A significant amount of flares might have

not been detected, but from the observations it seems the flares happen at any phase of the quiescence.

2.3.4 Spectral analysis

For each spectrum of O-201843, we fitted the interesting lines of the system with simple Doppler broadening in order to loosely quantify their evolution, we show the results in Table 2.2.

During quiescence, the spectra are mostly featureless. They show a slightly blue continuum with broad Balmer absorption, and Na and Ca II lines coming from the interstellar medium. From comparison with other spectral types (see Fig. 2.8) we see that the Balmer lines might come from a late A-type or early F-type star. We note that the Balmer lines are relatively shallow compared to those of stellar spectra. Although the photometry of the system shows two stars, we see no signatures of an other star, which could be hidden by the brightness of its companion. The contribution of the secondary to the brightness of the system is significant enough to cause ellipsoidal modulations in the photometry (see Sec. 2.3.2). We therefore expect the brighter star to be the secondary. Since it is not possible to conclude on the nature of the primary star, we assume the usual primary of a CV, a WD, hidden by the bright secondary.

The three spectra obtained during outburst are Echelle spectra, from which we are unable to recover the shape of the continuum. We can therefore only use spectral lines to estimate the behaviour of the system in outburst. In these spectra, we find the same Balmer absorption lines as the one observed in quiescence. Considering the differences in resolution of the different spectra, the FWHM and equivalent width of these lines do not appear to change significantly during the outburst. We also find a He II emission line at 4680 Å and an emission line at 6555 Å that could correspond to either He II or Hα. Due to the limited range of our spectra, we only detect the He II line at one epoch. The evolution of the 6555 Å line presented in Figure 2.2 shows that it is the strongest near the peak of the outburst and fades away during the decline.

2.4 Discussion

The origin of the outbursts of O-201843 is unclear and is examined in this Section. The light curve of O-201843 is consistent with the predictions of the DIM, i.e. a thermally unstable accretion disc, comparable to those of DNe.

The DIM predicts that the brightness of the system should rise slowly before the outburst is triggered. This is a consequence of the gradual increase of the local mass transfer rate and temperature before reaching the critical values for stability. We can also use the DIM to explain the evolution of the orbital modulations. During quiescence, the disc is very dim, and the variability detected is due to the secondary. Mass starts to build up in the disc, it slowly brightens and starts to hide the effects of the distortion of the secondary. The brighter fraction of the disc is small at first but its extent grows as matter accumulates, affecting the two minima of the variability differently. One becomes shallower as the disc outshines the secondary and the other becomes deeper when the secondary obscure a small part of the disc. This effect is best seen when the disc is at its brightest, at the peak of the outburst (see the right panel of Figure 2.4). The shallow eclipse indicates that the inclination of the system is moderate, a higher

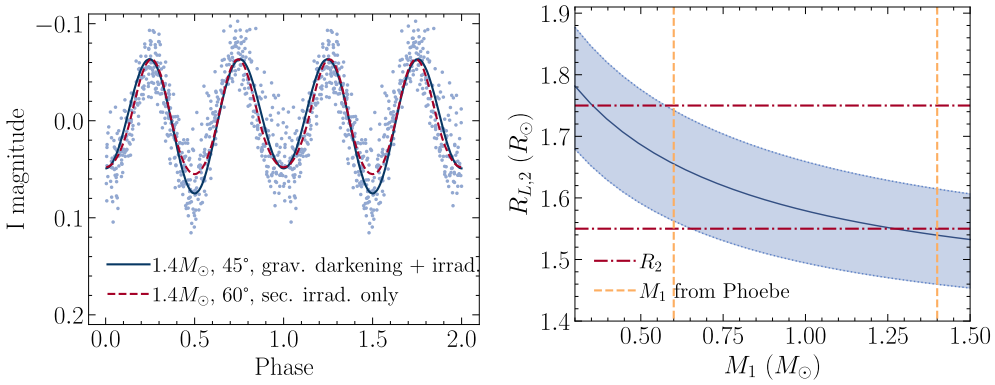

Figure 2.5: *Left*: Phase-folded photometry of OGLE-BLG504.12.201843 during the quiescent state compared with two Phoebe2 models. Data are shown in blue and two different models are overplotted. The blue line shows an early F companion of $1.6M_\odot$ with a WD of $1.4M_\odot$ and $i = 45°$, with gravity darkening and irradiation of the secondary. The red line shows an early F companion of $1.6M_\odot$ with a WD of $1.4M_\odot$ and $i = 60°$, with only irradiation of the secondary. In both models the primary has a temperature of 3×10^4K. *Right*: Estimation of the Roche lobe radius of the secondary $R_{L,2}$ using Equation (2.4) with different primary masses M_1 and a secondary mass $M_2 = 1.6 \pm 0.2M_\odot$. The constraints on M_1 obtained with Phoebe2 are shown as yellow vertical dashed lines and the range of possible secondary radii R_2 is indicated as red horizontal dashed lines.

inclination would deepen the eclipse as seen in eclipsing systems like IP Peg (Bobinger et al., 1999) or OY Car (Nicholson, 2009).

We note that if the outbursts can be explained by the DIM, then the high amplitude of the outbursts translates into a high critical disc mass transfer rate $\dot{M}_{\rm crit}$. Since $\dot{M}_{\rm crit}$ increases with the disc radius (Smak, 1983), we expect the extent of the disc to be large, which is consistent with the large dimensions of the system. The timescales of the outbursts also suggests that the quiescent disc is likely cold. Since the disc is usually expected to be irradiated by the WD, the low temperature of the disc would mean that the WD is relatively cold as well.

While the DIM can account for most of the photometric features of O-201843, the spectroscopy of the system differs from the spectra of thermally unstable accretion disc. We discuss this issue in Section 2.4.1 and we constrain the system geometry in Section 2.4.2. We consider the ensuing conditions on the mass transfer between the secondary and the primary in Section 2.4.3. Finally, in order to contextualise the nature of O-201843 we compare it with known DNe in Section 2.4.4.

2.4.1 Spectra of unstable accretion discs

The growth of emission lines observed in the outburst spectra (see Figure 2.2) could be explained by an accretion disc: the lines grow in intensity as temperature increases in the optically thin parts of the disc. However, these lines are not double-peaked, which is generally expected from an accretion disc. This could be related to a moderate inclination of the system or some other physical process. For instance some Nova-like CVs show single-peaked disc emission that are well reproduced by disc winds (Inight et al., 2021a). There are also high inclination Nova-like CVs, called SW Sex

systems (Dhillon et al., 2013), that only show double-peaked signals for a small portion of their orbital period.

Even though the accretion disc provides a crude explanation for the emission lines in outbursts, we see strong differences between the spectra of O-201843 and those of known systems with thermally unstable accretion discs. Efforts in identifying the spectroscopic signatures of DNe show that one should generally expect Balmer emission cores with absorption wings in quiescence and Balmer absorption lines in outburst. This behaviour seems to be explained by a change in optical thickness as temperature increases in the disc. Yet there seem to be a substantial amount of systems that deviate from this rule, showing no or barely perceptible emission cores in quiescence and some emission lines during the outburst (Han et al., 2020; Morales-Rueda & Marsh, 2002). Thus, the lack of emission lines in the quiescence spectra of O-201843 is concerning but does not invalidate the hypothesis of an outbursting disc.

The most straightforward explanation for the absence of emission cores is that they might be undetectable in our spectra. Given the low signal-to-noise ratio and resolution of the spectra, along with the brightness of the secondary, it is possible that small emission cores are hidden. This might also account for the shallowness of the stellar absorption lines. O-201843 could then have a bright secondary similarly to the unusual CV V1129 Cen, which shows faint 0.6-0.8 mag outbursts in the V band with a recurrence timescale of roughly a year (Walter et al., 2006). This system does not show the usual emission lines caused by the accretion disc and Bruch (2017) hypothesised that this system could be a DN with a bright type F secondary star that outshines the disc. The issue with this hypothesis lies in the lack of change in absorption line profiles during the outburst, when the disc outshines the rest of the system. As stated before, one expects to detect absorption lines originating from the disc during the outburst. In the case of a bright secondary, these lines could blend with the stellar absorption lines, but it is unclear why we do not observe any significant change in the profile of these lines when the disc undergoes an outburst.

Another possible explanation for the lack of emission lines during quiescence is given by Idan et al. (2010). They modelled the spectra of cold accretion discs using the DIM and found an optically thick disc with Balmer absorption lines and no emission lines. They argue that optically thin regions in quiescence should only appear in the disc photosphere or in winds (Matthews et al., 2015), which would only appear during outbursts or if there is significant irradiation of the disc by the WD. In the case of O-201843, the long timescales of the outburst seem to suggest that the disc is initially cold and the irradiation from the WD is minimal. So the quiescent spectra could be dominated by absorption lines, and consequently the Balmer lines we observe would be a blend of the lines from the disc and the secondary. As the temperature increases during the outburst, some regions of the disc might become optically thin and cause the emission lines.

Additionally, we tried to fit the outburst spectra taken by the MIKE spectrograph with The Payne spectral models (Ting et al., 2019) to see if we could extract some stellar parameters. No good fit was found because the spectra are too smooth and the few absorption lines that were detected are uncharacteristically shallow. This could mean that the profile of the absorption lines is indeed modified by the accretion disc, either with undetectable emission cores or blends of absorption lines.

Altogether, the spectra of O-201843 do not exclude the presence of an accretion disc despite not showing the expected features. Additional information could be obtained

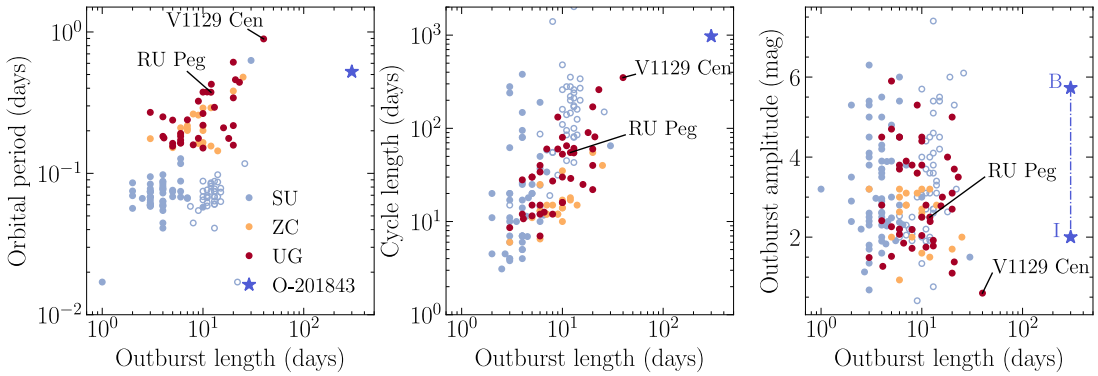

Figure 2.6: Comparison of the properties of OGLE-BLG504.12.201843 with the catalog of DNe compiled by Otulakowska-Hypka et al. (2016). The parameters of O-201843 are shown with a blue star, the catalog in DNe is separated in SU UMa (blue), Z Cam (yellow) and U Gem (red) systems. We also indicate the properties of V1129 Cen and RU Peg. Left panel: orbital period vs outburst length. Middle panel: average cycle length vs outburst length. Right panel: outburst V amplitude vs outburst length, the outburst amplitude of O-201843 coming from DASCH (in the B band) is denoted with "B" and the one coming from OGLE (in the I band) is denoted with "I". For SU UMa systems, the parameters of regular cycles are denoted with full points while circles indicate the properties of supercycles.

by examining the evolution of the continuum during the outburst, however, as stated in Section 2.3.4, this is not possible with the current data. It is therefore important to get more spectra of the system during outbursts.

2.4.2 Geometry of the system

The constraints on the nature of the secondary obtained with the spectra of O-201843 require an unusually bright companion for a CV. It is thus necessary to check whether these configurations are consistent with the known parameters of the system.

First, we use the orbital variability in Figure 2.4 to estimate some of the properties of the binary, specifically the mass ratio q and inclination i. We try to reproduce the ellipsoidal shape of the quiescent light curve using Phoebe2 (Prša et al., 2016). We set up the system as a semi-detached binary with a period of 0.523419 days with an early F secondary star ($M_2 = 1.6 M_\odot$). We vary the mass of the WD primary M_1 and inclination of the system i, and set the radius of the WD to follow the relation $R \propto M^{-1/3}$. We run the models with either gravity darkening, secondary irradiation or both to see which combination is able to reproduce the orbital variability.

We find that secondary irradiation alone fails to induce a difference in the two minima observed in the quiescent variability of the system for primary temperature below 3×10^4 K. The effect of irradiation is still small at higher temperatures, which is likely due to the large separation between the secondary and the primary. The insignificance of irradiation by the primary means that the observations are consistent with a relatively cold primary. Conversely, gravity darkening manages to replicate both the shape and minima difference of the variability. The only difference we observe when changing M_2 is a lower i for a higher M_2, which is likely due of the degeneracy between i and mass ratio $q = \frac{M_2}{M_1}$. For an early F star, the most successful models

have M_1 between 0.7 and 1.4 $M_\odot$ ($1.29 \lesssim q \lesssim 2.57$) with i between 45° and 50°. We show an example of a successful model in the left panel of Figure 2.5 for the case of $M_2 = 1.6 M_\odot$, as well as an example of the contribution of secondary irradiation. The moderate inclination is consistent with the lack of eclipse in quiescence, and might contribute to the lack of double-peaked signals in the disc spectra.

An early F secondary is unusually young and large for a CV. We check how such a secondary fits within the orbit parameters by calculating the semi-major axis a of the system:

$$a^3 = \frac{GMP_{\rm orb}^2}{4\pi^2}, \tag{2.3}$$

where $M = M_1 + M_2$. Under the early F secondary assumption ($M_2 \simeq 1.6 M_\odot$), this equation yields $a = 3.7 R_\odot$ for $M_1 = 0.7 M_\odot$ and $a = 3.9 R_\odot$ for $M_1 = 1.4 M_\odot$. Thus an early F secondary with $R_2 \simeq 1.7 R_\odot$ would fit within the system orbit. A study of population synthesis of CVs by Goliasch & Nelson (2015) shows that CVs can form with companions of spectral type earlier than K. Using MIST isochrones (Dotter, 2016; Choi et al., 2016), we estimate that the maximum main-sequence age of a $1.6 M_\odot$ star is around 1.8×10^9 years. According to the WD cooling tracks from Fontaine et al. (2001), this leaves enough time for a WD primary to cool to temperatures as low as 10000 K. We note however that accretion onto the WD primary should increase its temperature. Therefore, depending on the mass transfer rate of the system, the WD temperature might significantly diverge from the low temperatures mentioned above.

Overall, an early F secondary seems to fit within the observed parameters of the system. The next step is to establish whether such a companion is consistent with the observed outbursts, especially the long timescales and the corresponding mass transfer rates.

2.4.3 Mass transfer

If the outbursts of O-201843 originate from a thermally unstable accretion disc, then the mass transfer from the secondary and in the disc should fulfill certain criteria.

Firstly, an accretion disc requires that the secondary overfills its Roche lobe. Using the Roche lobe radius approximation from Eggleton (1983a):

$$\frac{R_L}{a} = \frac{0.49 q^{2/3}}{0.6 q^{2/3} + \ln(1 + q^{1/3})}, \tag{2.4}$$

together with Equation (2.3) allows to estimate the Roche lobe radius of the secondary $R_{L,2}$ given a specific mass ratio. We evaluate $R_{L,2}$ over all possible primary masses in the cases of an early F-type main sequence secondary with mass $M_2 = 1.6 \pm 0.2 M_\odot$. In the right panel of Figure 2.5, we compare $R_{L,2}$ to the range of possible secondary radii $R_2 = 1.6 \pm 0.15 R_\odot$ for an early F companion. We also indicate the constraints on the primary mass M_1 obtained with Phoebe2. According to these estimations, it seems possible that an early F companion overflows its Roche lobe. We checked these estimations for cases of smaller secondary stars and found that in this system, a main sequence secondary of type later than late type F cannot overfill its Roche lobe. This is to be expected since the dimensions of the system are quite large for a CV, and thermally unstable accretion discs seem to mainly occur in binaries with much closer orbits and smaller secondary stars. We therefore conclude that in the case of a main sequence companion, the presence of an accretion disc requires the secondary star to be

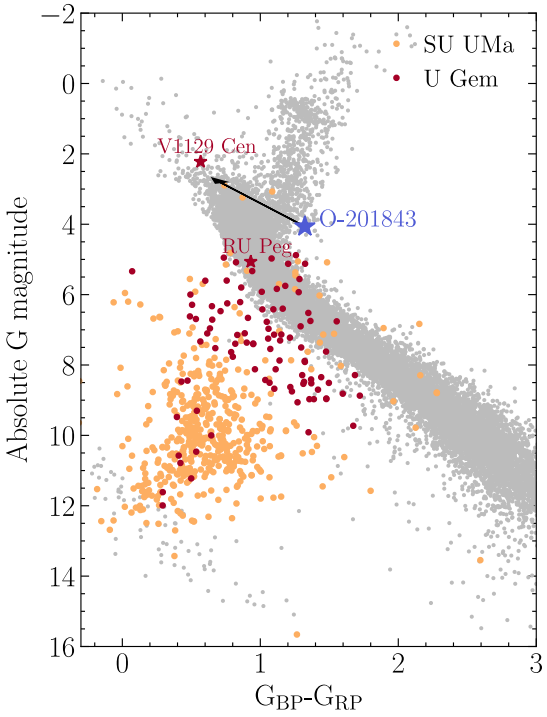

Figure 2.7: OGLE-BLG504.12.201843 in the HR diagram with a catalog of DNe obtained by merging the "Gold" sample of CVs from Inight et al. (2021b) with the CV sample from Abril et al. (2020). O-201843 is denoted with a blue star and DNe are separated in SU UMa (yellow) and U Gem (red) systems. The black arrow shows the effect of a reddening of $E(B-V) = 0.5$ mag. Points in grey are data selected from the Gaia Early Data Release 3 (EDR3, Gaia Collaboration 2021) by requiring that the sources have parallax errors lower than 10% of their parallax. This criterion allows to compute the absolute magnitudes with the distance as inverse of the parallax.

of type no later than F. We note however that in the case of a more evolved secondary, the requirement derived above does not hold anymore.

Secondly, the recurrent outbursts in the disc should be explained by the DIM, in which the stability of the disc depends on the local mass transfer rate. Kalomeni et al. (2016) studied the evolution tracks of CVs, in particular they included the treatment of unstable accretion discs using the critical mass transfer rates inferred by the DIM. Their results show that for the orbital period of O-201843, an early F companion allows for the formation of thermal-viscous instabilities in the disc. However, they also show that the average mass transfer rate $\langle \dot{M} \rangle$ of such a system would be above $10^{-8.8} \mathrm{M}_\odot/\mathrm{yr}$, meaning the system would fall in the regime of super-soft X-ray sources. In this case, the additional X-ray radiation may heat up the disc sufficiently to prevent the development of thermal instabilities. Furthermore, according to Townsley & Gänsicke (2009), a system with $\langle \dot{M} \rangle > 10^{-8} \mathrm{M}_\odot/\mathrm{yr}$ results in a WD primary temperature $T_1 > 25000$ K for $M_1 = 0.6 M_\odot$ or $T_1 > 50000$ K for $M_1 = 0.9 M_\odot$, which is inconsistent with the idea of a cool WD primary and disc. It is therefore unclear whether thermal-viscous instabilities actually occur in O-201843.

2.4.4 Comparison to DNe

Overall, the regular recurrence and shape of the outbursts of O-201843, along with their asymmetry, are reminiscent of long outside-in outbursts of U Gem type DNe: a fast rise followed by a decline that is slow at first and then accelerates. While the long timescale of the outbursts is analogous to superoutbursts (Rivera Sandoval et al., 2020), Mróz et al. (2015) did not find any secondary luminosity modulations that would correspond to superhumps. Besides, the shape of the outbursts does not resemble those of superoutbursts, they are more similar to normal DNe outbursts despite their long timescales. We conclude this study by comparing the photometry O-201843 to that of other known DNe in hope that it will help to draw a conclusion on the nature of the system.

An obvious divergence from DNe occurs during the quiescent state, which shows a slow 0.75 mag rise in brightness. Despite being a feature predicted by the DIM, we could not find any mention of the observation of such brightenings in the literature, although the SU UMa type DN V363 Lyr does show a small brightening before both outbursts and superoutburst (Kato, 2021). Interestingly, Smak (2000) notes that this transitional state is one of the weaknesses of the DIM since it has never been observed in other DNe despite being essential to occurrence of the outburst. This could mean some additional mechanism is involved in DNe outbursts that does not operate in O-201843. The lack of such mechanism could be linked to the unusually long recurrence time of the outbursts of O-201843.

Additionally, we do not find any records of the small recurring flares in quiescence mentioned in Section 2.3.3 in other DNe. They could be much more short-lived and harder to observe in the case of normal outburst cycle time. However consecutive flares were observed after superoutbursts in WZ Sge systems (Kato, 2015), which were successfully reproduced by Hameury & Lasota (2021) by adding several mechanisms to the DIM, such as variation of the mass transfer from the secondary, disc truncation and irradiation of the disc. In the case of O-201843, these flares could be small instabilities that fail to propagate far in the disc. Their symmetric shape are reminiscent of inside-out outbursts, which are triggered close to the inner edge of the disc and involve a much smaller portion of the disc than outside-in outbursts. Overall these flares are a very interesting feature and are most likely linked to disc instabilities.

In Figure 2.6, we compare the properties of O-201843 to the catalog of DNe compiled by Otulakowska-Hypka et al. (2016). Here, the cycle length should be interpreted carefully because the time elapsed between cycles can vary a lot for one DN. Since we do not have V band data for O-201843, we mark the outburst amplitude with a range set by the photographic amplitude from DASCH and I band data from OGLE. Additionally, some DNe in this catalog also display superoutbursts (SU UMa systems) and in this case we differentiate the parameters of cycles and supercycles with different symbols. The cycle length is the time elapsed between two normal outbursts and the length of supercycle is the time elapsed between two superoutbursts. The recurrence time of O-201843 is unusually long compared to that of DNe, where outbursts occur every few weeks or months. The length of the outburst itself is also generally much shorter, around a couple of days or weeks instead of almost a year in O-201843. From both left and middle panels in Figure 2.6 we can clearly see that O-201843 is an outlier. As shown in the middle panel, Otulakowska-Hypka et al. (2016) suggest there could exist a relation between the outburst length and the cycle length. In this case, O-201843 would actually follow this relation despite having such extreme

properties. The right panel shows that the amplitude of the outburst is relatively normal.

In Figure 2.7, we show the position of O-201843 in the Hertzprung-Russel (HR) diagram alongside a catalog of DNe obtained by merging the "Gold" sample of CVs from Inight et al. (2021b) with the CVs sample from Abril et al. (2020). Both samples were selected from Gaia DR2 (Gaia Collaboration, 2018) by considering objects with accurate parallax that were cross-matched with various CVs catalogues. We plot the HR diagram using similar criteria and compute distances as inverse parallax, which gives 2.35 ± 0.29 kpc for O-201843. We estimated the reddening $E(B-V)$ of O-201843 by measuring equivalent widths of Na I D lines in our high resolution spectra and using the relations of Poznanski et al. (2012). We obtained values of $E(B-V)$ between 0.1 and 0.45 mag and chose to indicate the effect of $E(B-V) = 0.5$ mag in the HR diagram. From Figure 2.7 we can see that the WD or accretion disc is dominant in most DNe. Only a couple of systems (mainly U Gem DNe) and O-201843 appear closer to the main sequence, meaning they are likely dominated by a main sequence secondary star. We also indicated the properties of two systems that are quite close to O-201843 in Figure 2.6, namely RU Peg and V1129 Cen. While RU Peg is quite ordinary, V1129 Cen has more extreme characteristics which were discussed in Section 2.4.1. Nonetheless, V1129 Cen has much shorter outburst and cycle length than O-201843. The similar luminosity and color between O-201843 and V1129 Cen gives further support to our hypothesis of a bright early F secondary star. We note that reddening corrections would make the secondary even brighter and bluer, as indicated by the arrow in Figure 2.7.

Altogether, the photometry of O-201843 shows strong similarities with DNe but also important differences. While these peculiarities have not been observed in other DNe, it is possible that O-201843 is an extreme U Gem DN, or at least is somehow linked to DNe.

2.5 Conclusion

To summarize, we have analysed optical photometry and spectroscopy of O-201843 and suggest that O-201843 is a U Gem type DN with extreme properties. The photometry shows clear features of an accretion disc from which the outbursts can originate. It also display two unusual features that, to our knowledge, are only rarely observed in other DNe. The slow brightening preceding the outbursts is a prediction of the DIM and its absence in regular DNe could indicate that some physical process usually suppresses it. The small flares with amplitude $\lesssim 0.2$ mag in I band detected during quiescence are another peculiar feature. We suggest that they might be small outbursts that fail to propagate far in the disc.

The analysis of the spectroscopy shows Balmer absorption that can either come from an early F secondary or the accretion disc. We however do not see the features of a WD and the usual features of an unstable accretion disc, i.e. no emission lines or cores in quiescence and no additional Balmer absorption in outburst. A possible explanation is that the disc is not or weakly irradiated by the primary WD, rendering it unusually cold. Additionally, the emission lines appearing during the outburst lack the double-peaked signal that one would expect from an accretion disc. As suggested by the orbital variability of the system, the inclination might just be low enough for the lines to be single-peaked. Obtaining time-resolved spectroscopy of this system could help to understand the lack of double-peaked lines as well as accurately constrain some

of the parameters of the system such as its mass ratio and inclination. It could also provide insights on how the system changes during the small flares appearing during quiescence. Additionally, such spectra would permit a similar analysis to what was done by Kára et al. (2021), who used Doppler tomography (Marsh & Horne, 1988) on the disc emission lines to obtain information on the velocity structure of the disc. Moreover, new spectra, especially in UV, could also help elucidate the nature of the primary and secondary.

Finally, the outburst duration and cycle length would be unprecedented among other U Gem type DNe. One potentially similar object to O-201843 is V1129 Cen, which has similar orbital period and location in the HR diagram, but its outburst and cycle length and amplitude are still significantly smaller than those of O-201843. If O-201843 is not a DN, it could be a new type of CVs that is tightly linked to DNe. Further study of this system should help understanding thermal-viscous instabilities and outbursts in accretion discs. Furthermore, the very long timescales of the system allows to see features that might not be possible to observe otherwise (e.g. flares) and it will be of great benefit to study them. The next outburst of O-201843 should begin in May 2023, peak around July 2023 and end in February 2024. The end of this outburst will not be visible due to conjunction with the Sun. The following outburst, starting in January 2026 and ending in October 2026 with a peak around March 2026, should be fully visible.

We thank Juna Kollmeier, Julio Chanamé and Doron Kushnir for contributing to the spectroscopic observations of OGLE-BLG504.12.201843 and Krzysztof Stanek for coordinating these observations. CL thanks Yuan-Sen Ting for his valuable insights and his help with The Payne. We thank the referee for their helpful comments. The work of CL and OP has been supported by INTER-EXCELLENCE grant LTAUSA18093 from the Ministry of Education, Youth, and Sports. The research of OP has been supported also by Horizon 2020 ERC Starting Grant 'Cat-In-hAT' (grant agreement no. 803158). MP is supported by the SONATINA grant 2020/36/C/ST9/00103 from the Polish National Science Center. Support for JLP is provided in part by ANID through the Fondecyt regular grant 1191038 and through the Millennium Science Initiative grant ICN12_009, awarded to The Millennium Institute of Astrophysics, MAS. JS was supported by the Packard Foundation. SD acknowledge support from the National Key R&D Program of China (No. 2019YFA0405100), the National Natural Science Foundation of China (grant No. 12133005) and the XPLORER PRIZE. We thank the support from Chilean Time Allocation Committee (CNTAC) through program ID CN2017B-85. The DASCH project at Harvard is grateful for partial support from NSF grants AST-0407380, AST-0909073, and AST-1313370.

OGLE data are available on a reasonable request to A. Udalski. DASCH data are publicly available. Spectroscopic data are available on a reasonable request to C. Landri.

Appendix A: Spectra

In Figure 2.8, we show the full spectrum of O-201843 during quiescence, indicate the interesting lines and compare it to the spectra of typical A0, G2 and F2 stars. In Figure 2.9, we show wider portions of our spectra and identify of interesting lines.

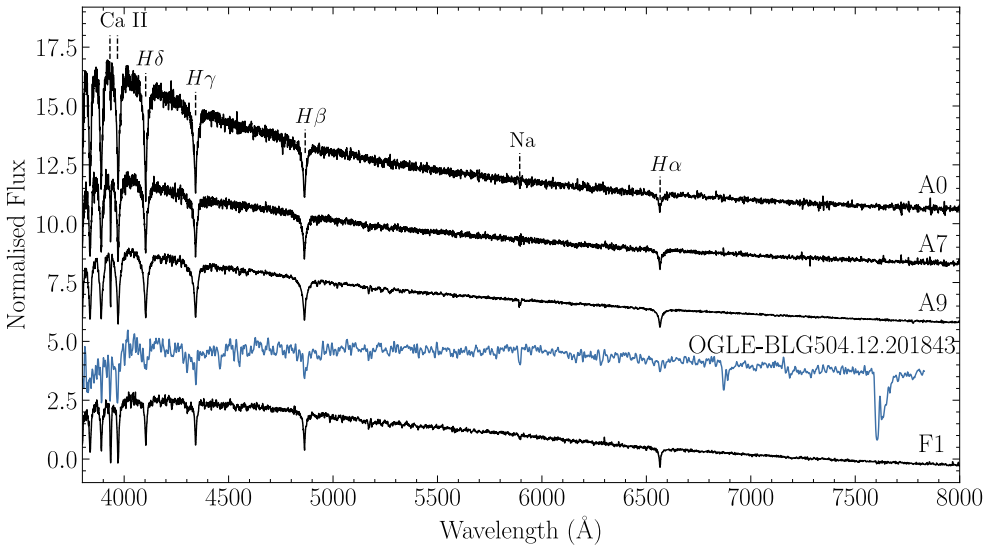

Figure 2.8: Full Spectra of O-201843 in quiescence (taken on 2017-10-24) with identification of interesting lines and template spectra from PyHammer (Kesseli et al., 2017; Roulston et al., 2020). Quantitative parameters of the lines are given in Table 2.2.

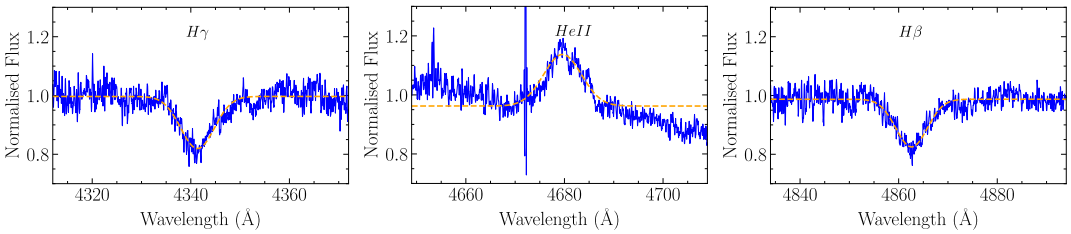

Figure 2.9: Portions of the spectrum of O-201843 during an outburst (taken on 2018-03-06) with identification of interesting lines. Quantitative parameters of the lines are given in Table 2.2.

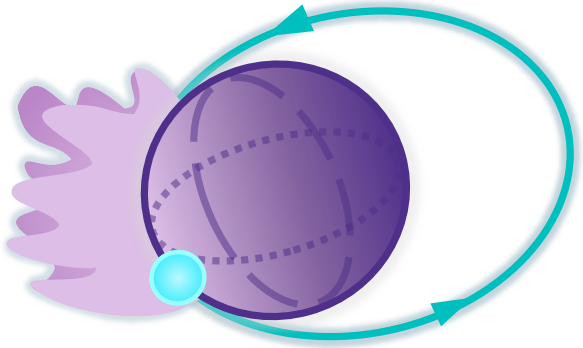

3. Driving asymmetric red supergiant winds with binary interactions [1]

Camille Landri and Ondřej Pejcha

Published in Monthly Notices of the Royal Astronomical Society,
Volume 531, Issue 3, July 2024, Pages 3391–3405

Abstract

Massive stars in the red supergiant (RSG) phase are known to undergo strong mass loss through winds and observations indicate that a substantial part of this mass loss could be driven by localised and episodic outflows. Various mechanisms have been considered to explain this type of mass loss in RSGs, but these models often focus on single-star evolution. However, massive stars commonly evolve in binary systems, potentially interacting with their companions. Motivated by observations of the highly asymmetric circumstellar ejecta around the RSG VY CMa, we investigate a scenario where a companion on an eccentric orbit grazes the surface of a red supergiant at periastron. The companion ejects part of the outer RSG envelope, which radiatively cools, reaching the proper conditions for dust condensation and eventually giving rise to dust-driven winds. Using simple treatments for radiative cooling and dust-driven winds, we perform 3D smoothed particle hydrodynamics simulations of this scenario with a 20 $M_\odot$ RSG and a 2 $M_\odot$ companion. We follow the evolution of the binary throughout a total of 14 orbits and observe that the orbit tightens after each interaction, in turn enhancing the mass loss of subsequent interactions. We show that one such grazing interaction yields outflows of 3×10^{-4} $M_\odot$, which later results in wide asymmetric dusty ejecta, carrying a total mass of 0.185 $M_\odot$ by the end of simulations. We discuss the implications for the evolution of the binary, potential observational signatures, as well as future improvements of the model required to provide sensible predictions for the evolution of massive binaries.

[1]This chapter is a pre-copyedited, author-produced version of an article accepted for publication in Monthly Notices of the Royal Astronomical Society following peer review. The version of record [Camille Landri, Ondřej Pejcha. Driving asymmetric red supergiants winds with binary interactions. MNRAS, Volume 531, Issue 3, July 2024, Pages 3391–3405] is available online at https://doi.org/10.1093/mnras/stae1379.

3.1 Introduction

The red supergiant (RSG) phase is an important part of the evolution of massive stars with initial masses between 8 and 25 $M_\odot$ (e.g., Ekström et al., 2012), during which they undergo substantial mass loss through winds. Observations show that a significant part of this mass loss can be driven by episodic outflows localised on the stellar surface (Humphreys et al., 2021), as is shown by the ejecta surrounding VY CMa. VY CMa is a RSG located at 1.2 kpc (Zhang et al., 2012) and is one of the largest and most massive RSGs observed to this date, with a current radius of $1420 \pm 120 R_\odot$, a luminosity of $(2.7 \pm 0.4) \times 10^5 L_\odot$, and an initial mass at the upper range for RSGs ($25 - 32\,M_\odot$, Wittkowski et al., 2012). Various observations of VY CMa show that it is embedded in asymmetric circumstellar ejecta with distinct and complex structures such as arcs, knots, and clumps (Smith et al., 2001; Humphreys et al., 2007; Jones et al., 2007; Kamiński et al., 2013; Richards et al., 2014; O'Gorman et al., 2015; Decin et al., 2016; Vlemmings et al., 2017; Gordon et al., 2019; Kaminski, 2019; Humphreys et al., 2021; Quintana-Lacaci et al., 2023; Humphreys et al., 2024). The clumps, in particular, are thought to be caused by highly localised mass-loss events that have been occurring for the past 1200 yrs (Shenoy et al., 2016), but their origin so far remains unexplained.

Various mechanisms have been considered to explain episodic mass loss in single RSGs, generally involving dust-driven winds launched by a disturbance of the stellar surface by magnetic activity, convection, or pulsations (e.g., Smith et al. 2001; Humphreys et al. 2007; O'Gorman et al. 2015; Vlemmings et al. 2017). However, quantitative prescriptions of these processes are scarce and often ambiguous, and stellar evolution models of cool supergiants continue to use time-averaged empirical mass loss formulations that do not take into account the episodic nature of RSG mass loss (e.g., de Jager et al., 1988; Nieuwenhuijzen & de Jager, 1990; van Loon et al., 2005). Since these localised outflows can represent a large fraction of the mass lost by the RSG, as is the case for VY CMa, our poor understanding of these mechanisms introduces large uncertainties in current massive star evolution models (e.g., Smith, 2014a) and serious discrepancies between theory and observations (e.g., Massey et al. 2023). Furthermore, a lot of important astrophysical processes, such as gravitational wave emission from compact binaries, chemical evolution of galaxies, and core-collapse supernovae (SNe), strongly depend on massive star evolution. It is therefore crucial to improve our understanding of episodic mass loss in RSGs and better constrain their fate.

An important aspect of RSG evolution is multiplicity. A significant fraction of massive stars are found in binary systems (e.g., Mason et al., 2009; Sana et al., 2012; Moe & Di Stefano, 2017), with a large variety of possible configurations, including some with short separation of the two stars which allow them to interact. A small but significant part of these systems are expected to remain bound and interact throughout their whole evolution, leading to the formation of objects such as X-ray binaries or gravitational wave events. For instance, common formation channels for double neutron star binaries show multiple evolution stages where one of the stars is a RSG interacting with its companion (e.g., Tauris et al., 2017). Therefore, scenarios where binary interaction and stellar winds interplay are likely to occur. While the impact of binarity on stellar winds has been investigated in the case of stars on the Asymptotic Giant Branch (AGB) (e.g., Chen et al., 2020; Bermúdez-Bustamante et al., 2020; Aydi & Mohamed, 2022; Esseldeurs et al., 2023), it remains widely unexplored for RSG stars.

In this paper, we investigate a scenario where binary interaction can drive anisotropic mass loss episodes in RSGs that can later turn into dust-driven winds. More specifically, we consider a RSG with a companion grazing the RSG envelope on a highly eccentric orbit. We illustrate this scenario in Fig. 3.1: the companion grazes the outer envelope at each periastron passage and the shocked gas is ejected from the envelope. As the ejected gas spreads outward, it cools and eventually reaches temperatures that are low enough to allow dust to condense. Radiative pressure then accelerates the newly formed dust grains, dragging the gas along and effectively driving an asymmetric wind. Eventually, the companion enters deep into the envelope of the RSG and commences a common envelope evolution (e.g., Paczynski, 1976; Fragos et al., 2019; Röpke & De Marco, 2023; Lau et al., 2022; Gagnier & Pejcha, 2023, 2024). This scenario resembles the grazing envelope evolution proposed by Soker (2015) except we do not involve accretion disk and jets around the companion and the resulting outflow morphology is different (Shiber et al., 2017). Our model makes use of radiation pressures on dust grains, which was suggested as important in the late stages of common envelope evolution by Glanz & Perets (2018b). Glanz & Perets (2021) also studied common envelope evolution in eccentric binaries but did not address anisotropic outflows during periastron passages.

We explore the proposed scenario through 3D hydrodynamics simulations, where we include a simplified treatment of dust formation and radiation pressure driving the RSG outflows. We note that the aim of this proof-of-concept study is not to reproduce the detailed properties and complicated morphology of the ejecta surrounding VY CMa or other RSGs, where in reality they likely arise from an interplay of many different processes. Instead, our goal is to illustrate that binary interactions can potentially explain some of the observed features. A more sophisticated treatment of dust formation and radiative processes can be added in follow-up studies to reach a better agreement with the observations. In Section 3.2, we describe the methods used to model our scenario, including how we simplified the different treatments of the physical processes involved. In Section 3.3, we present our results, including the evolution of the orbit, amounts of mass ejected, and the ejecta expansion. In Section 3.4, we discuss the possible formation channels for our system, the implications of our model for binary evolution, the possible observational signatures of such winds, and future improvements for our models.

3.2 Methods

We use the Smoothed Particle Hydrodynamics (SPH) code Phantom (Price et al., 2018) that solves the Lagrangian form of the equations of hydrodynamics by discretising the fluid as particles with mass m and local fluid velocity v (e.g., Lucy, 1977; Gingold & Monaghan, 1977; Price, 2012). Physical quantities are then computed by summing particle contributions weighted by a smoothing kernel W, for instance, the density around particle a is given by:

$$\rho_a = \sum_b m_b W\left(|\vec{r}_a - \vec{r}_b|, h_a\right), \tag{3.1}$$

where h_a is the smoothing length, which defines the neighbourhood of the particle a and is proportional to the local particle number density $h_a = h_{\rm fact} n_a^{-1/3}$, $h_{\rm fact}$ is a proportionality factor. The resolution of the simulations is therefore set by the total number of particles used, the choice of smoothing kernel and $h_{\rm fact}$.

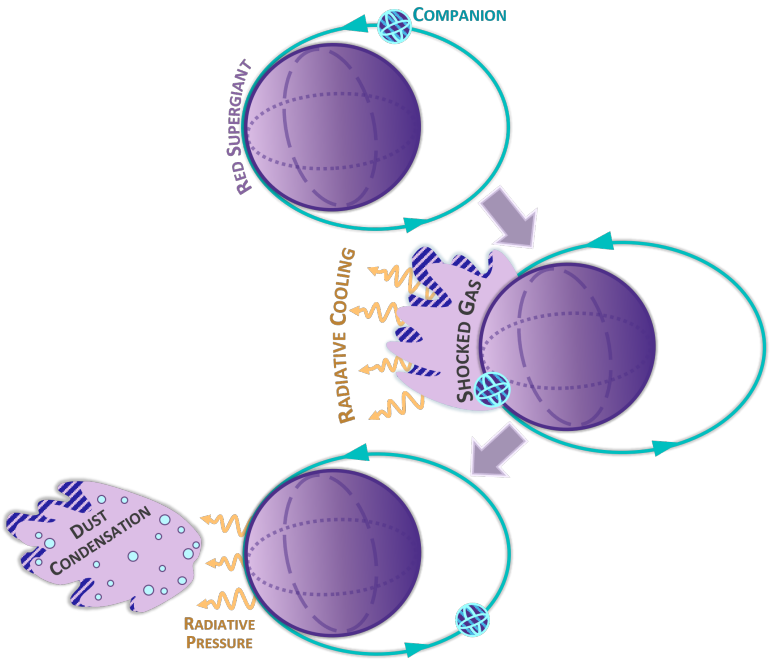

Figure 3.1: Schematics of the scenario explored with our simulations. A companion on an eccentric orbit grazes the envelope of the red supergiant and the resulting outflow radiatively cools, eventually reaching temperatures that permit dust formation. Radiation pressure then accelerates the dust grains, which drag the gas along, resulting in asymmetric dust-driven winds.

For this work, we set up PHANTOM is set up to solve the equations of hydrodynamics in the following form:

$$\frac{d\vec{v}}{dt} = -\frac{\nabla P}{\rho} + \Pi_{\rm shock} + \vec{a}_{\rm selfgrav} + \vec{a}_{\rm ext}, \tag{3.2}$$

$$\frac{du}{dt} = -\frac{P}{\rho}(\nabla \cdot \vec{v}) + \Psi_{\rm shock} - \frac{\Upsilon_{\rm cool}}{\rho}, \tag{3.3}$$

where P is the pressure, u is the internal energy, $\vec{a}_{\rm selfgrav}$ is the acceleration due to self-gravity, $\vec{a}_{\rm ext}$ represents the acceleration due to external forces such as sink particles or a radiative flux, $\Pi_{\rm shock}$ and $\Psi_{\rm shock}$ are viscous dissipation terms, and $\Upsilon_{\rm cool}$ is an optional cooling term. For W, we use the M_4 cubic spline kernel with $h_{\rm fact} = 1.2$, corresponding to an average of 58 neighbours.

Our scenario involves more than hydrodynamics and self-gravity. As shown in Fig 3.1, our simulations require a treatment of radiative cooling as the shocked gas is ejected from the RSG and a treatment of dust condensation and radiative pressure to accelerate the outflow. Since this work is meant to be a proof-of-principle, these treatments will remain simple, but we do plan on improving them in follow-up studies. For this study, we run a set of 4 simulations which are summarised in Tab. 3.1. In the rest of this section, we describe how we initialise the RSG and the binary system (Sec. 3.2.1), as well as how we treat dust-driven winds (Sec. 3.2.3) and radiative cooling (Sec. 3.2.2).

Table 3.1: Summary of the simulations performed for this study, showing the number of particles, minimum softening length h_a, and processes involved in the run.

Number of particles	min h_a	Physics involved
2.5×10^5	22 $R_\odot$	Hydro, self-gravity, cooling, dust-driven winds
1×10^6	14 $R_\odot$	Hydro, self-gravity, cooling, dust-driven winds
1×10^6	14 $R_\odot$	Hydro, self-gravity, adiabatic, no wind
2×10^6	11 $R_\odot$	Hydro, self-gravity, cooling, dust-driven winds

3.2.1 Initialisation of the system

We consider a binary of mass ratio $q = M_2/M_1 = 0.1$ with a $M_1 = 20\,M_\odot$ RSG similar to VY CMa, and a companion of $M_2 = 2\,M_\odot$, which could represent either a low-mass non-degenerate star or a fairly massive neutron star (NS) (e.g., Özel & Freire, 2016). We initialise this system in two steps, first, the 1D stellar profile of the RSG is mapped to 3D and relaxed in Phantom. During this phase, there are no external accelerations and no cooling. Then, after ensuring the stability of the 3D model, we add the companion and let the binary evolve for several orbital periods.

For the interior of the RSG, we create a 1D stellar profile with properties similar to VY CMa, which has mass and radius estimated to be $17 \pm 8\,M_\odot$ and $1420 \pm 120\,R_\odot$ respectively (Wittkowski et al., 2012). Since the companion mostly interacts with the outer layers of the RSG, it is unnecessary and computationally expensive to resolve the core and inner envelope of the giant. We therefore replace part of the stellar interior with a sink particle, a point mass that interacts with other particles only gravitationally through a potential smoothed with a cubic spline kernel. We excised about half of the envelope, which increases the number of particles at the stellar surface for a reasonable total number of particles as well as maintains a reasonable timestep during the simulations. For the rest of the envelope, we choose to use an artificial RSG profile that is convectively stable, since reproducing accurate convective motion requires resolving the inner envelope and we wish to avoid the decrease in timestep associated with these dense envelope layers. To create the model for the envelope, we follow the method provided in Appendix A of Lau et al. (2022) and solve the equations of hydrostatic equilibrium with an ideal gas equation of state assuming an adiabatic index of $\gamma = 5/3$, constant entropy, and accounting for the softened potential of the core. To solve these equations, we used boundary conditions from a realistic RSG profile obtained with Mesa (Paxton et al., 2011; Paxton et al., 2013a, 2015b, 2018b, 2019b; Jermyn et al., 2023) made to match the properties of VY CMa (for a detailed description of the process see Appendix 3.5).

Following this process, we created a 1D convectively stable profile of a $20\,M_\odot$ and $1500\,R_\odot$ RSG that is shown in Fig. 3.2. We initialised it in Phantom with a sink particle core of $13.75\,M_\odot$ and a potential smoothed with a cubic spline kernel. We define the

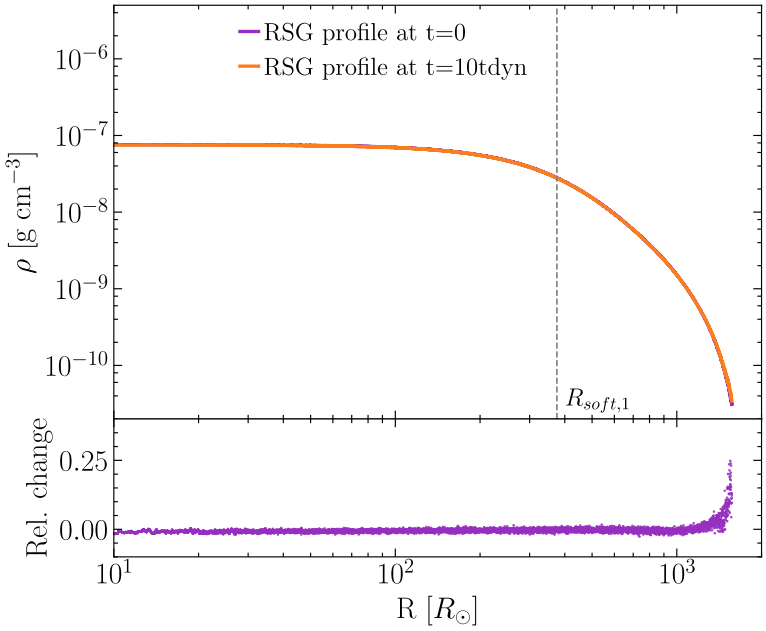

Figure 3.2: Density profile of the outer envelope of the RSG in our simulation at the end of the relaxation and 10 $\tau_{\rm dyn}$ later. Top: Density profiles, purple shows the initial profile and orange the profile after 10 $\tau_{\rm dyn}$, the grey dashed line shows the softening radius of the RSG numerical core. Bottom: Relative change in density computed as $(\rho_{\rm f} - \rho_{\rm i})/\rho_{\rm i}$. The envelope remains stable apart from a 25% increase in density at the surface.

smoothing length of this potential to be $R_{\rm soft,1} = 375\,R_\odot$, yielding an effective radius of 750 $R_\odot$ for the sink particle since the Newtonian potential is recovered at $2r_{\rm soft}$ with a cubic spline kernel. The 1D stellar profile of the RSG is mapped to a 3D distribution and then relaxed using the procedure implemented in Phantom by Lau et al. (2022). The giant is then evolved for 10 dynamical timescales ($\tau_{\rm dyn} = 241\,d$) to ensure the stability of the star. In Fig. 3.2, we show the density profile before and after relaxation: while the RSG remains stable, the relaxation and subsequent evolution yield a small change in stellar radius as the RSG has slightly expanded during the relaxation and then contracted. For the highest resolution simulation (2×10^6 particles) the RSG has expanded from 1500 $R_\odot$ to 1569 $R_\odot$.

Once the star is relaxed and stable, we add the neutron star companion by placing it at the apoastron of the orbit. Since a neutron star is much smaller than the minimum smoothing length in our simulations, we initialise it as a sink particle of mass $M_2 = 2\,M_\odot$ with smoothing length and accretion radius equal to the minimum resolved length, which is $R_{\rm soft,2} = 11\,R_\odot$ for our highest resolution simulations with 2×10^6 particles. The orbit of the system is set with a semi-major axis $A = 7500 R_\odot$ and eccentricity $e = 0.8$, so that the secondary grazes the envelope of the RSG at each periastron passage. We then evolve the system for several orbits until the companion has plunged deeply into the RSG envelope and the smoothed potential of the two sink particles overlap.

Table 3.2: Initial conditions of the high-resolution simulations (2×10^6 particles). $T_{\rm cond}$ and $p_{\rm dust}$ are the dust condensation parameters according to equations (3.4) and (3.5).

RSG primary	M_1	20.0 $M_\odot$
	R_1	1569 $R_\odot$
	$R_{\rm soft,1}$	375 $R_\odot$
	$M_{\rm core}$	13.75 $M_\odot$
	$M_{\rm env}$	6.25 $M_\odot$
	$T_{\rm eff}$	3500 K
Companion	M_2	2.0 $M_\odot$
	$R_{\rm soft,2}$	11 $R_\odot$
Binary	Eccentricity	0.8
	Semi-major axis	7500 $R_\odot$
	Period	43.91 yrs
Dust	$T_{\rm cond}$	1100 K
	$p_{\rm dust}$	-0.9

3.2.2 Cooling

As the companion goes through the envelope of the giant, the shocked gas that is ejected becomes optically thin and cools radiatively to the local equilibrium temperature $T_{\rm eq}$, where radiative cooling and irradiation from the RSG compensate each other. Under the assumptions of spherical symmetry and that the RSG radiative intensity dominated the local intensity, $T_{\rm eq}$ is given by (Lamers & Cassinelli, 1999):

$$T_{\rm eq} = T_{\rm eff,1} W(\tilde{r})^{1/(4+p_{\rm dust})}, W(\tilde{r}) = \frac{1}{2}\left(1 - \sqrt{1 - \left(\frac{R_1}{\tilde{r}}\right)^2}\right) \tag{3.4}$$

where $T_{\rm eff,1}$ and R_1 are the effective temperature and radius of the RSG, $\tilde{r}$ is the distance from the centre of mass of the RSG, and $W(\tilde{r})$ is the so-called geometrical dilution factor. Since we are primarily interested in situations where $T_{\rm eq}$ decreases below the dust condensation temperature$T_{\rm cond}$, equation (3.4) includes dust correction through the exponent $p_{\rm dust}$, which comes from approximating the wavelength-dependent part of the dust opacity with a power law,

$$\kappa_{\rm d} = \kappa_0 \left(\frac{\lambda}{\lambda_0}\right)^{-p_{\rm dust}} . \tag{3.5}$$

The dust properties are described in Section 3.2.3.

Since cooling impacts the kinematics of the ejected gas, it is important to take it into account in our simulations. The most natural way to handle this process would of course be to fully resolve radiative cooling and irradiation by imposing a cooling timescale over which the gas relaxes to $T_{\rm eq}$.

The cooling timescale $t_{\rm cool}$ over which a shocked gas radiates away its internal energy $U = 3/2 k_{\rm B} T$ can be estimated from a radiative cooling function (e.g., Fig. 22 of Ferland et al. 2017),

$$t_{\rm cool} = \frac{U m_{\rm p}}{\rho \Lambda(T)}. \tag{3.6}$$

Here, m_p is the proton mass, ρ is the density of the gas, and $\Lambda(T)$ is the usual cooling function. As the companion goes through the envelope of the giant, the shocked upper layers of the envelope reach temperatures up to 35000 K, for which the cooling rate is approximately 3.16×10^{-4} erg cm^3 s^{-1}. For a density of 10^{-10} g cm^{-3}, equation (3.6) yields $t_\mathrm{cool} \approx 3.2 \times 10^{-4}$ s. Considering the hydrodynamical timestep t_step of our simulations is of the order of hours, it is impossible to resolve such fast cooling in our simulations without making their cost unreasonably high.

We therefore have to resort to a simpler method to cool the ejected gas. Instead of imposing a timescale for the cooling process, the ejected particles are cooled so that they would exponentially reach T_eq on a timescale equal to the hydrodynamical timestep. This ensures that cooling does not become faster than the explicit timestep and should prevent the development of cooling instabilities. To do so, the equilibrium temperature at a particle location $T_\mathrm{eq,a}$ is calculated using equation (3.4), and the corresponding specific internal energy is obtained using the ideal gas equation of state:

$$u_{\mathrm{eq},a} = \frac{k_\mathrm{b} T_{\mathrm{eq},a}}{(\gamma - 1)\mu m_\mathrm{p}}, \tag{3.7}$$

where the adiabatic index is $\gamma = 5/3$ and the mean molecular weight is $\mu = 0.659$. The local cooling rate per unit volume is then calculated as:

$$\Upsilon_{\mathrm{cool},a} = \rho \frac{u_a - u_{\mathrm{eq},a}}{t_\mathrm{step}}, \tag{3.8}$$

where u_a is the specific internal energy of the particle before cooling is applied. This cooling rate is applied in equation (3.3) for any particle that is considered "ejected", i.e. is outside of the RSG envelope,

$$\Upsilon_\mathrm{cool} = \begin{cases} \Upsilon_{\mathrm{cool},a} & \text{if} \quad \tilde{r}_a > R_1, \\ 0 & \text{if} \quad \tilde{r}_a \leq R_1. \end{cases} \tag{3.9}$$

To avoid approaching too low temperatures, we apply an arbitrary floor temperature of 500 K. Overall, our treatment of the radiative cooling process is an oversimplification and will require more accurate treatment in follow-up studies.

3.2.3 Dust-driven winds

In our scenario, the wind is driven by the radiation pressure on the dust condensing in the ejecta lifted by the companion passage. As the dust grains are accelerated outward by the radiative flux, they drag the gas along by transferring momentum through collisions. Accurately reproducing the formation of such winds therefore requires resolving dust formation (and destruction), the radiative acceleration of dust grains, and dust-gas interactions. As this work aims to be a proof-of-concept, we will treat this problem with simple methods that should yield qualitatively similar outcomes to more complete physical treatments. We leave the improvement of the wind treatment for follow-up studies.

The radiative acceleration of the dust grains due to the radiative flux of the RSG is taken into account by setting $\vec{a}_\mathrm{ext}$ in equation (3.2) so that it depends on a local Eddington factor Γ_a,

$$\vec{a}_\mathrm{ext,rad} = \frac{G M_1}{r_1^2} \Gamma_\mathrm{a} \hat{r}_a, \tag{3.10}$$

where $\hat{r}_a$ is the unit vector connecting particle a to the RSG. The simplest treatment of stellar winds is the so-called free wind approximation (Theuns & Jorissen, 1993), which consists of setting $\Gamma_a = 1$ so that all particles escape the gravitational pull of the star. We apply this method to our simulations, adding the condition that only particles with properties fulfilling dust condensation criteria are accelerated. To find out whether dust can condense in a specific region, we compare the condensation temperature of the dust $T_{\rm cond}$ to the temperature of the particle T_a and set the value of Γ_a as

$$\Gamma_{\rm a} = \begin{cases} 1 & \text{if} \quad T_a < T_{\rm cond}, \\ 0 & \text{if} \quad T_a > T_{\rm cond}. \end{cases} \tag{3.11}$$

We set the dust properties following Bladh & Höfner (2012) who parameterised dust-driven winds for different types of dust grains to determine the main wind-drivers. Based on their results and the low C/O ratio of RSG stars, we consider silicate grains composed of Mg_2SiO_4, for which they derived $T_{\rm cond} = 1100\,K$ and $p_{\rm dust} = -0.9$. The dust parameters We note that with this formalism, we do not account for the interaction between the dust and gas, which are effectively fully coupled.

Overall, our method is similar to the procedure devised by Bowen (1988), which has been widely used to treat dust condensation in AGB stellar winds (e.g., Bermúdez-Bustamante et al., 2020; Chen et al., 2020; Aydi & Mohamed, 2022; Esseldeurs et al., 2023) and common envelope evolution (e.g., González-Bolívar et al., 2022; Bermúdez-Bustamante et al., 2024), but it differs in some aspects. Their simulations are always adiabatic, so they compare the local equilibrium temperature (calculated using equation [3.4]) to the condensation temperature, whereas in our simulations the gas cools as it is ejected, and we can directly use the gas temperature for the comparison. Additionally, they use this comparison to calculate a local Eddington factor Γ that depends on the temperature difference and assumptions on gas and dust opacities, while we simply apply $\Gamma = 1$ wherever dust condensation conditions are met.

3.3 Results

We performed a total of 4 simulations: 3 runs with cooling, dust driving and varying resolution (2.5×10^5, 1×10^6, and 2×10^6 particles), and one control adiabatic run without cooling and dust-driven winds with 1×10^6 particles. The parameters of the runs are summarised in Tables 3.1 and 3.2.

In Fig. 3.4, we show snapshots of the density cross-section in our highest-resolution simulation during the first grazing of the RSG envelope. As the companion grazes the outermost layers of the envelope, the shocked gas is ejected approximately perpendicularly to the stellar surface. However, it is then dragged by the companion as it leaves the vicinity of the RSG. Eventually, the outflow expands approximately radially in the $y < 0$ region while we observe no ejection of gas in the $y > 0$ region. The outflow expands and cools, reaching the dust condensation temperature $T_{\rm cond} = 1100\,{\rm K}$ for $r \gtrsim 4500\,R_\odot$, where the gas density is about 10^{-14} g cm^{-3}. Radiative pressure then starts to accelerate the dust grains, effectively supporting the radial expansion of the gas. During the following orbit, the outflow continues expanding while the RSG, which first expanded as a response to the perturbation from the companion, is restoring its hydrostatic equilibrium. After one full orbit (around 40 years), the outflow has extended to a rough semicircle of radius $r \sim 400\,{\rm au}$ in the xy plane with a thickness of

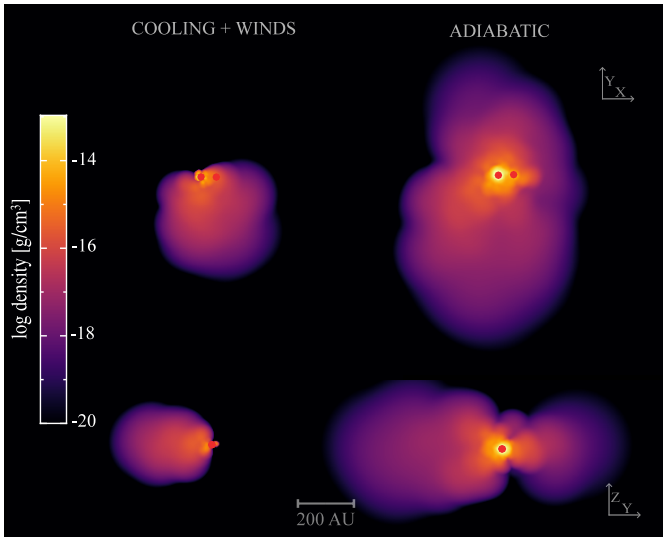

Figure 3.3: Comparison of the ejecta after one apastron passage of the companion for the adiabatic run (right panels) and a run with radiative cooling and dust-driven winds (left panels). The upper and lower panels show a cross-section of the density taken along the $z = 0$ and $x = 0$ planes, respectively. Both simulations were performed with 1×10^6 particles.

$z \sim 200$ au, reaching densities as low as 10^{-18} g cm^{-3} and terminal velocities of around 40 km s^{-1}. Besides producing these asymmetric winds, we also expect the interaction between the companion and the RSG envelope to impact the orbit of the system, which in turn impacts the conditions of each subsequent grazing.

To assess the relevance of the cooling and the dust-driven winds in supporting the asymmetric outflows, we performed a fully adiabatic simulation. In Fig. 3.3, we show the outflow resulting from one grazing interaction after the companion has passed the apastron in both the adiabatic and non-adiabatic simulations. We see that the ejecta in the adiabatic simulation is much more extended: it reaches $r \gtrsim 500$ au with a thickness of $\sim$300 au, while the radiatively cooled ejecta has only spread to $r \sim 200$ au with a thickness of $\sim$200 au. Additionally, the adiabatic outflow is denser, reaching up to 10^{-14} g cm^{-3} in the inner region, against $10^{-15} - 10^{-16}$ g cm^{-3} for the cooled outflow. Finally, the asymmetry of the ejecta with respect to the centre of mass of the system is much less pronounced in the adiabatic case: the adiabatic outflow broadly surrounds the RSG, while the gas is only ejected in a roughly semi-circular slab in the simulations with cooling and winds. This comparison shows that the cooling and wind prescriptions are essential to produce strongly asymmetric outflows.

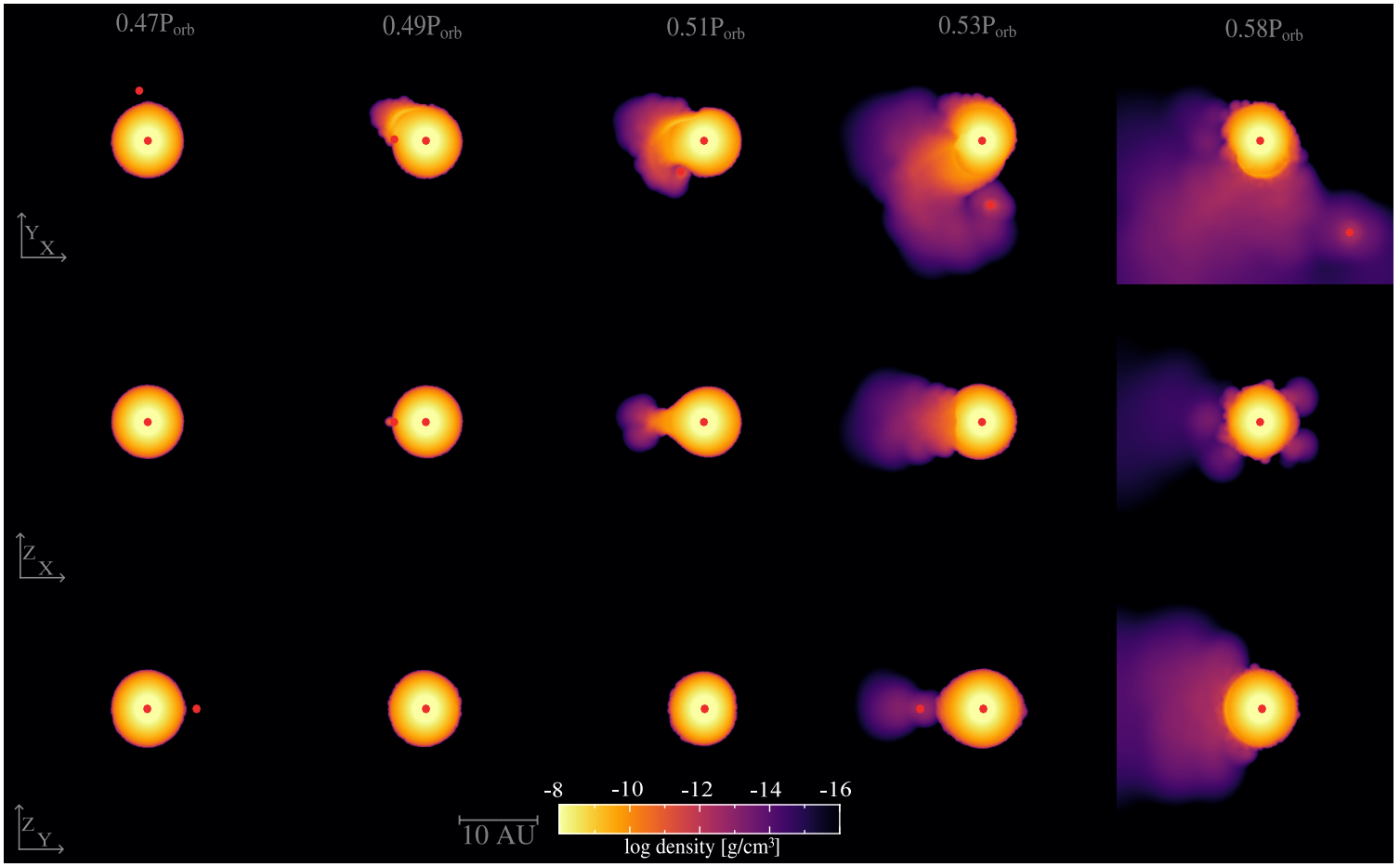

Figure 3.4: Snapshots of the density during the first periastron passage in our highest resolution run (2×10^6 particles). The upper, middle, and lower panels show cross-sections of density taken at $z = 0$, $y = 0$, and $x = 0$ planes, respectively. Sink particles are denoted as red circles. A full movie of the first interaction can be found at https://youtu.be/jcW0KyMayBE

.

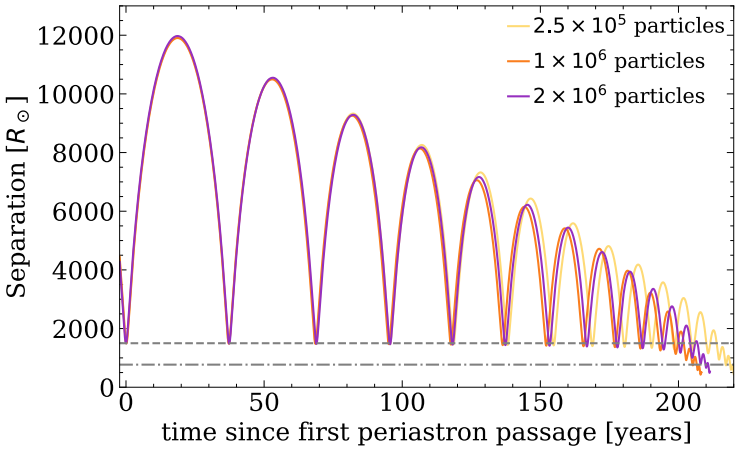

Figure 3.5: Evolution of the binary separation. The high, medium, and low-resolution runs are shown in purple, orange, and yellow, respectively. The upper and lower dashed lines show the RSG surface (1500 $R_\odot$) and the sum of the effective radii of the two sink particles for the high-resolution run (772 $R_\odot$).

3.3.1 Evolution of the orbit

As the companion grazes the RSG envelope, we expect the drag between the gas and the companion to considerably affect the orbit of the binary. In Fig. 3.5, we show the evolution of the separation of the binary. We see that during each subsequent periastron passage, the companion reaches deeper layers of the outer envelope and the orbit tightens while remaining eccentric. The binary starts with a ~40 yr period, which decreases on average by 3 – 4 years after each orbit, reaching a period of about 7 years on the 10$^{\text{th}}$ orbit. At this point, the companion is more than 250 $R_\odot$ beneath the RSG surface at periastron, driving more massive and less localised outflows, and decreasing the orbital period even faster.

After 13 orbits, the companion is fully engulfed by the RSG and starts spiralling in the envelope with a period of the order of one year, effectively starting a phase of common envelope evolution (CEE) (e.g., Paczynski, 1976; Röpke & De Marco, 2023). Unfortunately, we cannot resolve the inspiral of the companion in our simulations: the potential of the RSG sink core is smoothed up to 750 $R_\odot$, so we barely observe one full orbit of the inspiral before the smoothed potentials of the sink particles overlap, at the end of the 13$^{\text{th}}$ orbit. We expect that more mass will be ejected during CEE, and the outflow should retain some polar asymmetry until the CEE circularises the orbit. It is however not possible to determine the outcome of the CEE with our simulations.

Overall, the orbit of the binary tightens drastically throughout the simulation due to the grazing interaction, leading to CEE after only 200 years. We discuss implications and possible modifications to this timescale in Sec. 3.4.

3.3.2 Mass loss

We estimate the mass lost by the system after each periastron passage using the usual energy criteria: a particle is considered unbound if its kinetic energy is higher than its gravitational energy,

$$E_{\text{gr}} + E_{\text{kin}} > 0. \tag{3.12}$$

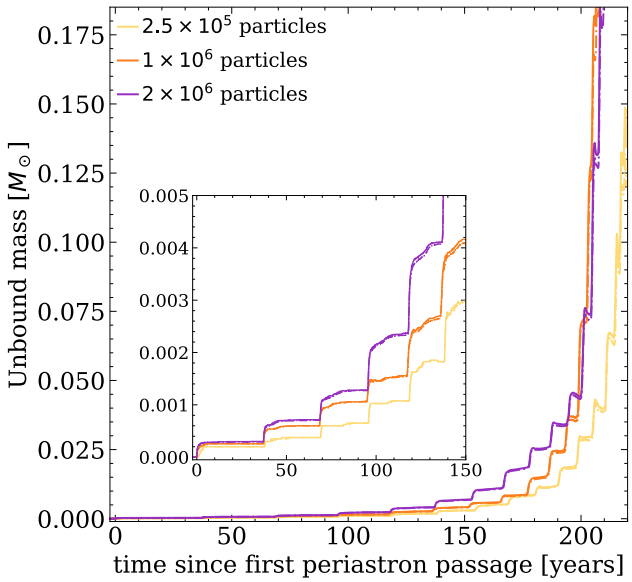

Figure 3.6: Evolution of the amount of unbound mass. The high, medium and low-resolution runs are shown in purple, orange and yellow respectively. Plain lines show the amount of unbound mass according to the energy criterion in equation (3.13), which includes the gas' internal energy, dashed lines show the amount of unbound mass using the more conservative energy criterion in equation (3.12), which does not include internal energy. The inner plot shows the mass loss during the first orbits.

Alternatively, a fraction of the internal energy of the gas, $\alpha E_{\rm int}$, can be converted into kinetic energy, and the amount of unbound particles is then determined as

$$E_{\rm gr} + E_{\rm kin} + \alpha E_{\rm int} > 0. \tag{3.13}$$

Since α is unconstrained, setting it to unity allows us to derive an upper limit on the mass loss of the binary, while the more conservative criteria set by equation (3.12) can serve as a lower limit. Using both criteria, we evaluate the evolution of the mass loss throughout the simulations, which we show in Fig. 3.6.

During the first three orbits, the mass loss is very episodic, with a sharp rise in the total unbound mass of $\sim 3 \times 10^{-4} M_\odot$ right after each grazing interaction. Between interactions, the amount of unbound mass stays essentially constant. Most of the ejected particles have been cooled, radiatively accelerated, and unbound within a year from the periastron passage of the companion. Then, from the fourth orbit onward, the sudden rise in mass loss becomes stronger and the unbound mass is rising continuously. Both of these features intensify after each subsequent interaction. Since the surface layers of the RSG expand in response to the grazing interaction, and the companion reaches deeper and denser layers of the envelope, it drives more massive episodic outflows at periastron, but also a low-intensity continuous outflow until the next interaction. About $10^{-3}\,M_\odot$ of mass is unbound $1-2$ years after the interaction, and about $10^{-4}\,M_\odot$ is lost continuously in between each periastron passage. After the $10^{\rm th}$ orbit, the system approaches CEE and episodically ejects $\gtrsim 10^{-2}\,M_\odot$ per interaction. The companion is completely engulfed by the envelope after the $13^{\rm th}$ orbit and ejects about $0.1\,M_\odot$ of matter in a continuous way. At the end of the simulation, which corresponds to a total of 14 orbits, the system has ejected a total of $0.185\,M_\odot$, 80% of which was ejected in

the last ten years of the evolution, during the onset of CEE.

We note that our estimation of the mass ejected during the late evolution of our system is flawed due to our simplified treatments of cooling and dust condensation. Our treatment of radiative cooling does not take gas opacities into account since it relies on the approximation that the ejected gas is optically thin. However, this assumption does not hold for the outflows launched when the system is close to the onset of CEE, which should be optically thicker considering their high density. The opacity of these outflows likely decreases as they expand, but they will become optically thin and start to radiatively cool at much larger distances from the system than earlier outflows. Therefore, our method underestimates the temperature of the late outflows, allowing dust to condense and radiation pressure to drive winds in regions where it is not likely to happen. This leads to an overestimation of the outflow velocities and possibly of the amount of unbound mass at late times.

Fig. 3.6 also shows that the differences between the two mass loss criteria are relatively insignificant, especially at early times when the two criteria yield practically the same result. This is expected, since the internal energy of the gas at the stellar surface is much lower than the kinetic energy imparted to the gas by the companion during the interaction and any extra thermal energy from shock interaction is quickly radiated. After five orbits, however, the companion starts to probe deeper layers of the envelope, with increasingly higher internal energy and where our cooling prescription is not active, so the two estimates deviate from one another. As the end of the simulation approaches, the gap between the two values deepens and we expect the difference between the two criteria to be similarly significant during the ensuing CEE phase.

3.3.3 Evolution of the ejecta

In Fig. 3.7, we track the evolution of the ejecta on longer timescales by showing density snapshots of our highest resolution simulation during subsequent orbits at the moment of apastron. Each successive periastron passage of the companion drives a new outflow, which first increases the density of the inner ejecta, then expands and merges with the less dense outer part of the ejecta. In this section, we use the term "ejecta" to qualify the entire body of ejected gas and the term "outflow" for the gas ejected due to one grazing interaction only.

The evolution of the ejecta can be broadly divided into two phases that mostly differ by the time elapsed between subsequent grazing interactions. For the first five orbits, the orbital period ranges from 40 to 20 years and the outflows can expand over large scales before the binary is at periastron again, which causes the broad spiral pattern in the ejecta appearing in the first row of Fig. 3.7. This slow evolution lasts for about 140 years, during which the ejecta expands to $r \gtrsim 1000\,\mathrm{au}$ as a roughly semi-circular slab of vertical thickness $\sim$500 au, with densities ranging from 10^{-15} g cm^{-3} in the innermost region to 10^{-19} g cm^{-3} in the outer ejecta.

As seen in Fig. 3.5, each interaction strengthens the orbital decay of the binary, which starts to strongly affect the outflows after the fifth orbit of the binary. At this point, the grazing interactions become more frequent, with a period $P_{\mathrm{orb}} \leq 20$ yrs, causing tighter spiral patterns in the inner ejecta while the ejecta continues spreading outwards. The companion also starts to dig deeper into the envelope of the RSG, significantly increasing the density of each subsequent outflow, reaching up to 10^{-13} g cm^{-3} in the innermost part of the ejecta. As the system approaches the onset of CEE, we also see

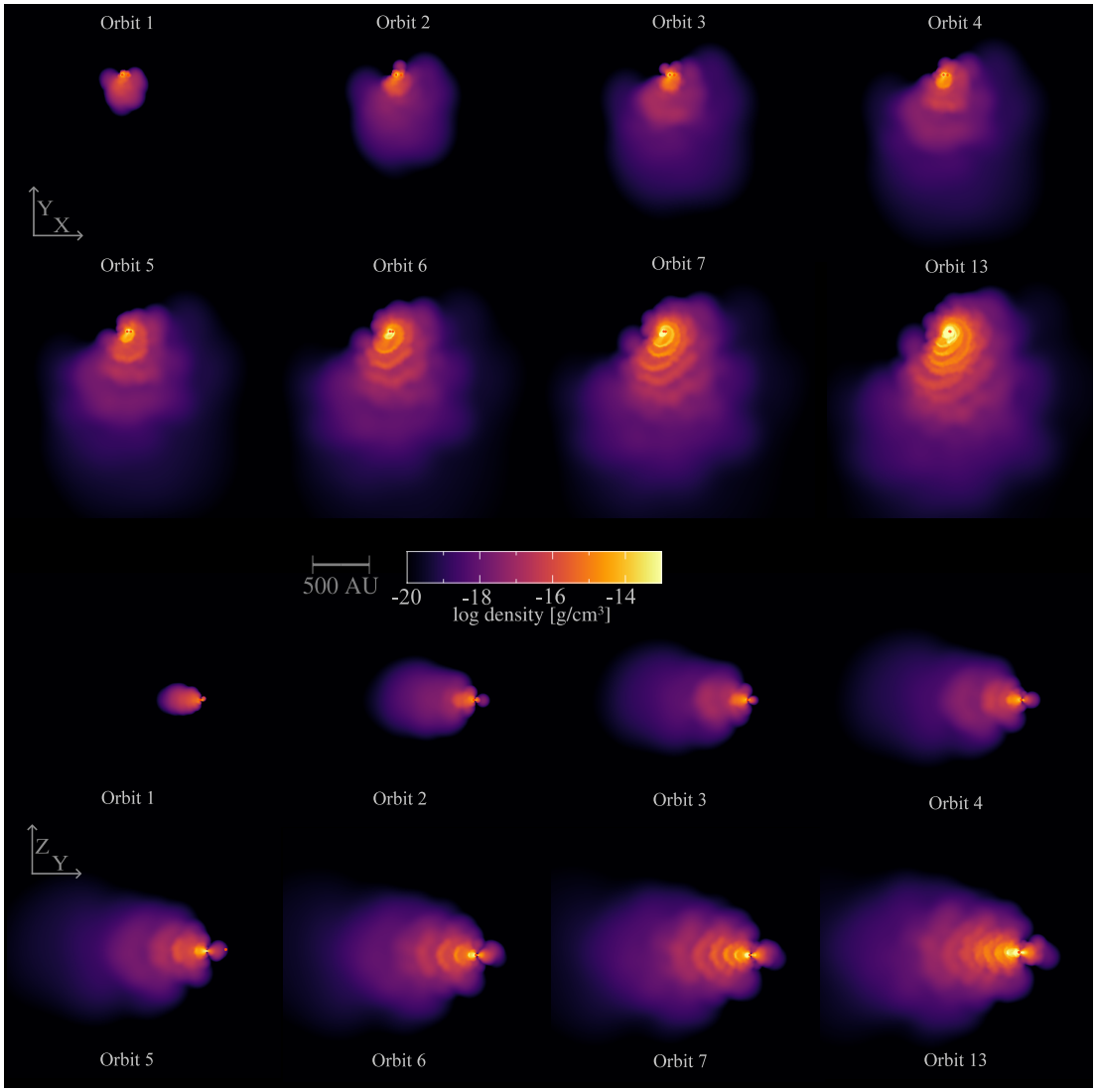

Figure 3.7: Density snapshots of the simulation with 2×10^6 particles taken when the companion is at apastron. The two upper rows show the density cross-section of the equatorial plane (slice along $z = 0$) and the two bottom rows show the meridional plane (slices along $x = 0$).

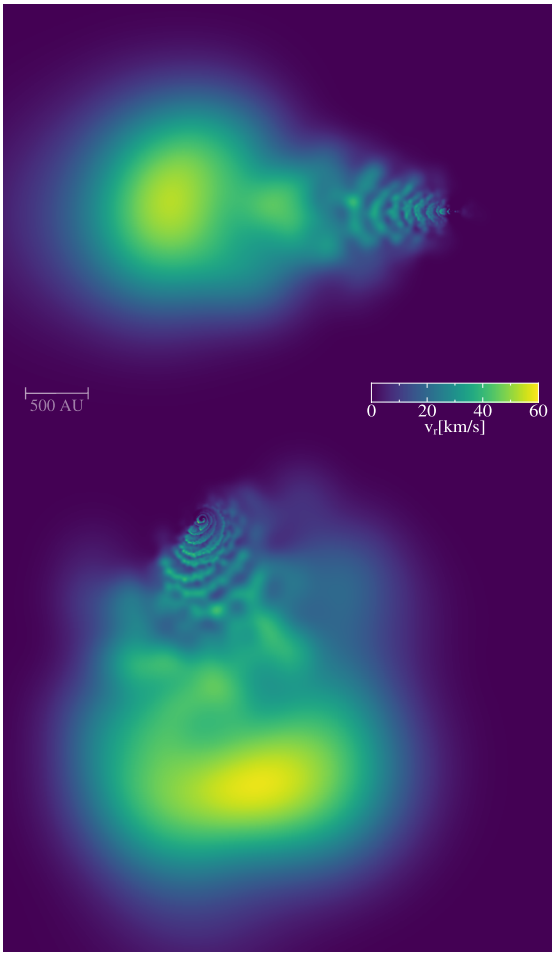

Figure 3.8: Snapshot of the radial velocity of the ejecta taken after 14 orbits. The upper and lower panels show radial velocities taken at $x = 0$ and $z = 0$ planes, respectively.

that matter is ejected more isotropically, and the densest part of the outflow spreads around the binary with a shape similar to a disc. We expect that the outflows will become even more isotropic as the system evolves through CEE since the orbit should circularise, but the already ejected material should retain its overall asymmetry.

At the end of the simulation, the dusty ejecta broadly resembles a cone and we can distinguish three main regions. First, the innermost region, directly surrounding the binary, results from the late time evolution during which the binary was close to the onset of CEE and the outflows are the most massive. With a total mass of about $0.15\,M_\odot$ extending up to ~100 au away from the binary in a roughly conical shape, it is by far the densest region of the ejecta. Since the time elapsed between grazing interactions has drastically decreased, the shell-like over-densities caused by the companion shocking the gas are closer to each other, yielding a tighter spiral pattern than in earlier stages of the simulation. Beyond the innermost ejecta, we identify a relatively dense region of $10^{-15} - 10^{-17}$ g cm^{-3} spreading up to ~500 au from the system, which we estimate to carry $\sim 3 \times 10^{-2}\,M_\odot$. This region is more asymmetric than the inner ejecta, it corresponds to where most of the outflows have merged and is thus made of the most extended parts of the late evolution outflows and the slowest regions of earlier outflows. Finally, a wide and less dense region extends to $r \gtrsim 2000$ au, with densities reaching very low values of $10^{-18} - 10^{-20}$ g cm^{-3}. This region carries roughly $5 \times 10^{-3}\,M_\odot$,

corresponding to the early outflows which have now spread far away from the binary.

In Fig. 3.8, we show the radial velocity of the gas at the end of the simulation. The late outflows can be traced in the spiral pattern by sharp velocity fronts, while the early outflows have softer velocity gradients as they merged a long time ago. The outermost ejecta, arising from the first outflows and spreading beyond $r \gtrsim 500\,\mathrm{au}$, show radial velocities of $v_\mathrm{r} \sim 50 - 60$ km s^{-1}. The rest of the ejecta has not reached such high velocities, the innermost part has on average $v_\mathrm{r} \lesssim 30$ km s^{-1} while the intermediate region reaches $v_\mathrm{r} \approx 40$ km s^{-1}. We, therefore, estimate the wind terminal velocity to be $v_\infty \approx 60$ km s^{-1}.

3.4 Discussions

Here, we discuss constraints on the evolutionary pathways that lead to the grazing by the companion (Sec. 3.4.1), statistics of binarity of RSGs (Sec. 3.4.2), the duration of the grazing phase (Sec. 3.4.3), what happens after the interaction (Sec. 3.4.4), observational signatures (Sec. 3.4.5), and possible future improvements of our model (Sec. 3.4.6).

3.4.1 Formation of the system

The evolutionary pathways leading to our configuration depend on whether the RSG companion is a compact object, such as a neutron star, or a low-mass non-degenerate companion. From the point of view of our simulations, both options are indistinguishable, because the gravitational potential of the companion must be smoothed on scales larger than its radius. If the companion is a low-mass main sequence (MS) star, the binary could have simply been born on this orbit and began interacting when the more massive star expanded to a RSG. Alternatively, the binary has such a low mass ratio that it may have formed in a wider more circular orbit and was subject to the Darwin and/or eccentric instability (e.g., Darwin, 1879b; Hut, 1980a; Eggleton & Kiseleva-Eggleton, 2001; Pešta & Pejcha, 2023), which would have reduced the binary separation and potentially increased its eccentricity. Considering that VY CMa is associated with but lies off of a cluster NGC 2362 (Lada & Reid, 1978; Mel'Nik & Dambis, 2009; Zhang et al., 2012), it is interesting to speculate about a scenario where a massive star in a binary explodes as a supernova, leaves behind a neutron star, and the explosion kick sets the neutron star on an eccentric orbit and the binary on a trajectory away from its birth cluster. While this scenario might not apply to VY CMa specifically, it is interesting to discuss it more generically.

We consider a common scenario for the formation of double neutron star binaries (Tauris et al., 2017), starting with two massive MS stars on a relatively close orbit. The more massive star eventually evolves and expands, and the binary experiences a phase of case B or C mass transfer. As the RSG transfers mass to its companion, it is gradually stripped of its envelope and eventually undergoes core collapse (CC). The collapsing star turns into a NS without fully disrupting the binary, which according to Renzo et al. (2019) should happen in about 14% of massive binaries. While the natal kick of the NS does not fully unbind the binary, it will increase its eccentricity (Brandt & Podsiadlowski, 1995; Kalogera, 1996) and widen the orbit to up to 4 times the pre-CC separation according to Kalogera (1996). The initially less massive star will expand to a RSG, eventually reaching radii large enough for the compact companion to graze the RSG envelope at periastron.

The timescale of the post-CC evolution depends on how close the initial masses of the two stars were and whether the accretion during the pre-CC mass transfer phase has increased the main sequence lifetime of the accretor (Neo et al., 1977). It is, however, strictly constrained by the tidal circularisation timescale of the binary (Zahn, 1977), since the star should reach the RSG phase before the eccentricity of the binary decreases significantly. If we consider that the initially less massive star is close to the onset of the RSG phase at the birth of the NS, and therefore has a significantly convective envelope, the circularisation timescale of the binary is highly dependent on the ratio of semi-major axis to stellar radius $\tau_{\rm circ} \propto (A/R_1)^8$. Using Eq. 2 of Verbunt & Phinney (1995), the circularisation timescale reaches a maximum estimate of $\tau_{\rm circ} \simeq 10^7$yrs for a $20\,M_\odot$, $1500\,R_\odot$ RSG. The binary should thus circularise on longer timescales than the timescale of the evolution and expansion of the future RSG, which should be at most of the order of 10^6 yrs if the star is still on the MS at the start of the post-CC evolution. Therefore, the binary should retain its large eccentricity by the time the compact companion can graze the envelope of the RSG.

3.4.2 Statistics of RSG binarity

Statistics of RSG binarity can serve as a clue as to whether our scenario occurs frequently. Neugent et al. (2018) devised some criteria to detect companions around RSGs from their contribution in the spectra of the binaries, however, they are mostly efficient for blue companions since their contamination is more easily distinguished from the red light of the RSG. A complementary way of determining the binarity of a RSG is to secure multi-epoch spectroscopy to look for periodic variations of radial velocities. However, due to the large radii of RSGs the minimum orbital period of their companion has to be of the order of hundreds of days, meaning that such spectroscopic studies have to be performed on timescales of years. Furthermore, the amplitude and timescale of these periodic variations are likely similar to the variability due to atmospheric convective motion in RSGs (Schwarzschild, 1975), which further complicates RSG multiplicity studies. Despite these difficulties, the binary fraction of cool supergiants in the Milky Way has been estimated to be around 35% (Burki & Mayor, 1983), and some X-ray binaries were found to have a RSG companion (e.g., Gottlieb et al., 2020; Hinkle et al., 2020). RSG multiplicity studies targeting the Local Group (e.g., Neugent et al. 2019; Patrick et al. 2019; Neugent et al. 2020; Dorda & Patrick 2021; Neugent 2021) generally find binary fractions around 30%, mostly with OB-type companions. Patrick et al. (2022) found 6 candidates for RSG + compact companion in the Small Milky Cloud, though they potentially are false positives, and Neugent (2021) estimated the fraction of RSG + compact companion in M31 and M33 to be about 4.73% using BPASS (Eldridge et al., 2017). While rates of binarity for RSGs inferred from observations are relatively low, especially for binaries with a compact companion, it is still non-negligible and therefore our grazing scenario seems plausible.

3.4.3 Duration of the grazing encounters

Our simulations cover only about 200 years or 13 orbits before the binary enters the CEE. Such a short duration would imply that our chances of finding a RSG undergoing this type of evolution are very slim given the RSG lifetime. However, the duration of our simulation is mostly driven by the constraints of available computing time and

resolution. If both can be increased, we could simulate the evolution for many more orbits before the CEE. This interaction is similar to a normal CEE, where Iaconi et al. (2018) and Reichardt et al. (2019) found that increasing simulation resolution leads to a longer duration of pre-CEE inspiral, mass transfer, and mass loss. The long duration of the pre-dynamical CEE phase is also seen in 1D binary evolution simulations (e.g., Klencki et al., 2021b; Marchant et al., 2021b). Observations of transients accompanying stellar mergers, the luminous red novae, also indicate the presence of pre-dynamical mass-loss lasting many hundreds and potentially thousands of binary orbits (e.g., Tylenda et al., 2011; Pejcha et al., 2016a,b, 2017; Blagorodnova et al., 2021).

Another aspect affecting the duration of the grazing phase is missing physics near the surface layers of the star. Real stars exhibit a complex interplay of convection, diffusion, and ionization in their surface layers, which affects the stability with respect to mass removal (e.g., Pavlovskii & Ivanova, 2015b). In RSGs specifically, the additional physical effects include the large size of convective cells, pulsations leading to in the outer atmosphere shocks, dust and molecule formation in the gas lifted off the surface by pulsations, and feedback from accretion onto the companion (e.g., Haubois et al., 2009; Shiber & Soker, 2018; Goldberg et al., 2022; Freytag & Höfner, 2023).

All of these effects could extend the duration of the grazing phase by making the conditions in the outer stellar layers different from what we assume in our adiabatic simulations. Furthermore, the mass ejections could happen intermittently depending on whether the periastron passage occurs during the maximum or minimum expansion of the RSG pulsation. Finally, a longer duration of the grazing phase could also facilitate precession and tilting of the companion orbit, for example, due to the action of tidal forces. The mass ejections would then still be oriented in one direction during each ejection or a series of subsequent ejections, but the orientation of the ejection could gradually change. All of these aspects would be interesting to investigate in future work.

3.4.4 Evolution and fate of the binary

Depending on the amount of envelope ejected during the CEE ensuing after the grazing and the nature of the companion, the system could evolve to a close binary with two compact objects (e.g., a double NS binary, Tauris et al. 2017), or the two stars could merge, possibly resulting in a Thorne-Żytkow object (TZO) (Thorne & Zytkow, 1977) if the companion is a NS, or an exotic supernova if the merger product explodes (e.g., Chevalier, 2012). It is, however, not possible to draw conclusions on the outcome of this process from our simulations, since properly simulating this phase of the evolution of the binary would require resolving the deep interior of the RSG.

We may broadly examine the outcome of the CEE using the energy formalism (e.g., Webbink, 1984):

$$-G\frac{M_1 M_{1,\mathrm{e}}}{\lambda R_1} = -\alpha_{\mathrm{C\,E}} G\left[\frac{M_{1,\mathrm{c}} M_2}{2A_\mathrm{f}} - \frac{M_1 M_2}{2A_\mathrm{i}}\right] \tag{3.14}$$

where $M_{1,\mathrm{e}}$ and $M_{1,\mathrm{c}}$ are the mass of the RSG envelope and core respectively, which are about 13.5 $M_\odot$ and 6.5 $M_\odot$ according to the MESA model used to set up our RSG. Parameter λ is defined by the mass distribution inside the star, A_i and A_f and the initial and final separation of the CEE. By setting α_{CE}, the envelope ejection efficiency, and

$\lambda \lesssim 0.1$ as appropriate for evolved red supergiants (Kruckow et al., 2016), we find that the CEE can unbind the whole envelope for final separation of $A_f \lesssim 4\,R_\odot$. Thus, it seems unlikely that the system ejects the whole envelope. This estimation is however too simple to reflect the reality since the efficiency of envelope ejection in CEE and the physical processes involved (e.g., recombination, dust formation) are still relatively unconstrained in current CEE models (see Röpke & De Marco 2023 for a detailed discussion). Therefore, we leave the fate of the binary as an open question.

We can, however, estimate the impact of our chosen initial conditions on the evolution of the system. We could consider a companion mass M_2 lower than $2\,M_\odot$, in which case we expect less massive outflows due to the grazing interaction. In our simulations, the efficiency of the radiative force to drive the winds would remain unchanged due to the very simple formulation of radiative pressure on dust grains, therefore we do not expect the wind velocities to change for a different companion mass. However, we note that in a realistic scenario, the efficiency of dust condensation does depend on the density of the gas, and since a lower mass companion yields less dense outflow, it would also likely change the wind properties. The decrease in companion mass would also cause the orbit to decay more slowly, as the dynamical friction between the outer envelope and the companion is lower during each periastron passage, which will result in a later plunge-in. We expect opposite effects for higher companion masses: more massive outflows and a faster evolution.

The choice of orbital parameters of the system should also have a significant influence on the evolution of the binary and the outflows. In our simulations, a is not freely chosen, it is set so that the binary separation at periastron is exactly equal to the radius of the RSG, $a = R_1/(1-e)$. For lower e, a is smaller and the less eccentric orbit will be overall closer to the RSG surface. As a result, the companion grazes a larger portion of the stellar surface and encounters higher densities. This leads to less asymmetric outflows, and the higher drag on the companion accelerates the orbital decay to CEE.

3.4.5 Observational signatures

Here, review various observations that can indicate that grazing encounters are ongoing or happened relatively recently: outflow emission, changes of the RSG, accretion onto companion, observable signatures of TZO, and supernova explosions. We also specifically discuss VY CMa.

Outflow emission

The most evident signature of this interaction is the emission from the cool asymmetric outflow, which we expect to be observable at millimetre/sub-millimetre and infrared wavelengths. As shown in Fig. 3.7 the dusty outflow could be angularly resolved with the ALMA interferometer if the distance to the system is small enough. Outside of the continuum emissions from the dust, the ejecta should also be traceable with molecular emissions, which arise from the various gas-phase chemistry across the outflow. Since we do not model the various phenomena occurring at the RSG surface, the morphology of the outflow in our simulations represents the simplest possible outcome. However, any complicated morphological feature in the outflow would likely be unresolvable, which includes the spiral features in the innermost ejecta, and traces of the common envelope phase would likely be hard to detect.

Changes of the RSG

Repeated close passages of a companion will affect the RSG by tidal dissipation. Our simulations are inadequate to study these processes, but we can speculate about some of the potential outcomes. First, the RSG could expand in response to the tidal heating. For our choice of companion mass, the orbital energy of a grazing orbit is much smaller than the RSG envelope binding energy (Klencki et al., 2021b) and no significant overall expansion is expected. However, the dissipated energy could still strengthen the processes that are already ongoing such as the more common dust-driven RSG wind, potentially leading to a tidally-enhanced wind (e.g., Tout & Eggleton, 1988; Chen et al., 2011). The intensity of this effect depends on the amount of tidal dissipation, the depth of deposition, and the ability of the star to quickly remove this excess energy by radiation.

Accretion onto companion

Before fully entering the envelope of the RSG, our system should also show X-ray emission from the accretion on the companion. Since the companion moves supersonically through the outflow of the RSG, we can approximate the accretion rate $\dot{M}_2$ of the companion using the approximation of spherical accretion onto a moving object (Bondi-Hoyle-Lyttleton accretion),

$$\dot{M}_2 = \frac{4\pi\rho(GM_2)^2}{(c_s^2 + v_2^2)^{3/2}}, \tag{3.15}$$

where ρ is the density of the surrounding outflow, c_s is the sound speed, M_2 the mass of the companion, and v_2 is the velocity of the companion relative to the surrounding gas. In our simulations, the average relative velocity of the companion is $20\ \mathrm{km\ s^{-1}}$, and the density of the surrounding ejecta is $10^{-15}\ \mathrm{g\ cm^{-3}}$, resulting in an accretion rate of $4 \times 10^{-6}\,M_\odot$. The corresponding accretion luminosity is $L_{\rm acc} = GM_2\dot{M}_2/R_2$ where R_2 is the radius of the companion. Inefficient accretion or radiative emission will decrease $L_{\rm acc}$. When considering a low mass MS companion of $R_2 \simeq 2R_\odot$, the accretion luminosity becomes $L_{\rm acc} \simeq 10^{35}\ \mathrm{erg\ s^{-1}}$, making it similar to X-ray bright T Tauri stars (Telleschi et al., 2007). For a NS companion of $R_2 = 10\,\mathrm{km\ s^{-1}}$, the accretion rate yields a very high luminosity of $L_{\rm acc} \simeq 10^{40}\ \mathrm{erg\ s^{-1}}$, which is a factor of ~50 higher that the Eddington limit for a $2\,M_\odot$ star. Given the super-Eddington accretion rate, the NS might look like an ultra-luminous X-ray source displaying super-Eddington flux only near the polar axis (e.g., King, 2009). If jets develop, our scenario reduces to the grazing envelope evolution developed by Soker (2015), Shiber et al. (2017), and Shiber & Soker (2018).

The high gas density in the vicinity of the RSG that gives rise to a high $\dot{M}_2$ also provides a large gas column that can absorb and scatter the X-rays. Considering a spherical constant-velocity outflow from the RSG with r^{-2} density profile, $\dot{M}_1 = 10^{-5}\,M_\odot\,\mathrm{yr^{-1}}$, velocity $20\,\mathrm{km\,s^{-1}}$, and inner edge at $1500\,R_\odot$, we obtain density $\approx 10^{-15}\ \mathrm{g\ cm^{-3}}$ and hydrogen column of $\sim 10^{23}$. Depending on the emission temperature and the detector properties, such a high gas column can reduce the expected flux by many orders of magnitude (e.g., Montez et al., 2015). Even with inefficient accretion and a high intervening gas column, we would still expect signatures of accretion such as highly ionized gas or feedback on the surrounding medium.

Observable signatures of TZO

The merger of the RSG core and the companion may also result in a supernova explosion, which could produce a black hole remnant if the companion is a compact object. Many Type IIn supernovae and other luminous transients show evidence for mass ejections preceding the terminal supernova explosion (e.g., Ofek et al., 2014; Margutti et al., 2014; Jacobson-Galán et al., 2022). It has been suggested that a strong binary interaction or a CEE is responsible for pre-supernova mass ejections leading to a formation of dense circumstellar medium (CSM, e.g., Smith, 2011; Chevalier, 2012; Metzger, 2022). This has motivated theoretical works investigating interactions of supernova explosions with various aspherical CSM distributions such as disks, oblate or prolate ellipsoids, and colliding winds shells (e.g., Vlasis et al., 2016; Suzuki et al., 2019; Kurfürst et al., 2020; Pejcha et al., 2022). Interestingly, none of these works has considered the type of aspherical CSM that we are predicting here: subtending only a small fraction of a solid angle with internal density variations corresponding to individual periastron passages. However, based on analogous works on different aspherical CSM distributions, we can predict that a supernova explosion colliding with the CSM predicted here would lead to a radiative shock that is quite likely embedded in the optically thick supernova ejecta and that initially reveals its presence only as an additional energy source. When the supernova ejecta becomes optically thin, the CSM distribution could manifest in profiles of nebular spectral lines.

Supernova explosions

Many Type IIn supernovae and other luminous transients show evidence for mass ejections preceding the terminal supernova explosion (e.g., Ofek et al., 2014; Margutti et al., 2014; Jacobson-Galán et al., 2022). It has been suggested that a strong binary interaction or a CEE is responsible for pre-supernova mass ejections leading to a formation of dense circumstellar medium (CSM, e.g., Smith, 2011; Chevalier, 2012; Metzger, 2022). This has motivated theoretical works investigating interactions of supernova explosions with various aspherical CSM distributions such as disks, oblate or prolate ellipsoids, and colliding winds shells (e.g., Vlasis et al., 2016; Suzuki et al., 2019; Kurfürst et al., 2020; Pejcha et al., 2022). Interestingly, none of these works have considered the type of aspherical CSM that we are predicting here: subtending only a small fraction of a solid angle with internal density variations corresponding to individual periastron passages. However, based on analogous works on different aspherical CSM distribution, we can predict that supernova explosion colliding with the CSM predicted here would lead to a radiative shock that is quite likely embedded in the optically-thick supernova ejecta and that initially reveals its presence only as an additional energy source. When the supernova ejecta becomes optically-thin, the CSM distribution could manifest in profiles of nebular spectral lines.

Application to VY CMa

We can compare these expected signatures to observations of VY CMa. We first note that no companion has been directly observed around VY CMa, suggesting that if our scenario was ever involved in the evolution of VY CMa, the companion is now either fully engulfed in the envelope of the supergiant or is orbiting too close to the stellar surface to be observable Decin et al. (2006) reconstructed the mass-loss

history of VY CMa and found that it underwent a phase of increased mass loss rate of $\simeq 3 \times 10^{-4}\, M_\odot\,.\mathrm{yr}^{-1}$ about 1000 years ago. This phase lasted about 100 years and was preceded by a phase with relatively low mass loss rate of $\simeq 10^{-6}\, M_\odot\,\mathrm{yr}^{-1}$ for about 800 years and succeeded by a phase of increased mass loss of $\simeq 10^{-4}\, M_\odot\,\mathrm{yr}^{-1}$ lasting until today. It would be natural to identify this event of increased mass loss with grazing interactions, which culminated with a stellar merger followed by an enhanced wind phase due to the energy deposition in the RSG envelope by the inspiralling companion (e.g., Clayton et al., 2017b; Glanz & Perets, 2018b).

Alternatively, the morphology of our asymmetric outflow seems to be consistent with the dusty clumps observed in the immediate vicinity of VY CMa (e.g., Kaminski, 2019). The mass of these clumps was estimated to be of the order of $10^{-3} - 10^{-2}\, M_\odot$ with velocities of $20 - 50$ km s^{-1}, and were likely ejected about 100 years ago (Humphreys et al., 2024), which is consistent with the total mass of the extended ejecta in our simulations and the velocities shown in Fig. 3.8. We note that our wind terminal velocities only depend on the Eddington factor, which is a free parameter set in equation (3.11), so they are a broad upper limit rather than a reliable estimate. Kaminski (2019) estimated the size of the clumps with 3D radiative transfer models, and found that the most elongated clump (clump B) could be up to 1000 au long, which is compatible with the size of our ejecta.

Concerning the companion accretion, Montez et al. (2015) obtained non-detections in X-rays that place an upper limit of $L_\mathrm{X} < 1.6 \times 10^{31}$ erg s^{-1}, which is far below the estimated L_acc 10^{35} erg s^{-1} we derived. However, the upper limit is highly contingent on the emission temperature and the sensitivity to softer radiation with $T \lesssim 10^6$ K is much worse given the expected intervening absorption column. Still, VY CMa does not prominently display highly ionized emission lines or other signs of an accretion process. So if VY CMa had a companion, it was probably already deep within the RSG envelope by the time the observations were made. If the companion is a NS then we might expect VY CMa to be a TZO, spectroscopic studies of the object do show Ca I and Rb I lines (Wallerstein, 1971; Dinh-V-Trung et al., 2022), however, no traces of other heavy elements have been found. The use of different tracers, such as the ones proposed by Farmer et al. (2023), could shed some light on this issue.

To summarize, VY CMa could have merged with a grazing companion about 1000 years ago, however, the complexity of its surrounding medium would require some modification to our model or combination with other physical processes. Increasing the realism of our model could allow to better determine whether this mechanism plays a role in the formation of some of the asymmetric outflows around VY CMa.

3.4.6 Improvements of the model

Our simulations use approximations and simple treatments of the involved physical processes to reduce their computational cost. Here, we discuss potential improvements for follow-up studies.

Firstly, we have made several assumptions regarding the initial conditions of our setup. We have assumed that when the simulations start, no interactions are taking place between the RSG and the companion. Considering how close the two stars are, there is a chance that the RSG overfills its Roche Lobe around the periastron of one or more orbits preceding the start of the simulations, resulting in potential mass transfer and/or outflows. However, any interaction during the previous orbits would

simply lead to smaller, possibly negligible, mass ejections. To assess the relevance of previous interactions, one could evolve the binary in 1D in MESA following the methods of Marchant et al. (2021b), and possibly obtain better initial conditions for our simulations.

Another approximation we made in this study is to model the RSG envelope as convectively stable, which prevents us from investigating the interplay between surface convection and the companion interaction, which would likely affect the morphology of the ejecta. However, resolving convective motion requires modelling the entire RSG envelope as well as including radiative transport in the envelope, to avoid a strong overestimation of the convective flux (e.g., Ricker et al. 2018). Both choices would dramatically increase the cost of the simulations, especially considering the long timescale of our simulations, therefore, incorporating convection in our simulations will likely be considered in later phases of improvements.

Furthermore, as mentioned in Sec. 3.2.2 and 3.2.3, our numerical treatment of dust-driven winds has been simplified and can be improved to various degrees. Dust formation and destruction can be more accurately treated by including a density and composition dependence, for instance by using the moment method (Gail et al., 1984; Gail & Sedlmayr, 1988; Gauger et al., 1990; Gail & Sedlmayr, 2013), which has been implemented for carbonaceous dust grains in Phantom by Siess et al. (2022). RSG stars have a low C/O ratio, so this method would need to be adapted to oxygen-rich dust condensation, which is significantly harder to model than carbon-rich dust formation. There are many more dust species to account for compared to the case of carbon-rich dust, and it is not completely known which particles serve as seed nuclei for oxygen dust growth (for more details, see Chapter 15.5.6 of Gail & Sedlmayr 2013). Implementing a complete condensation scheme for oxygen-rich dust in 3D hydrodynamics codes is therefore a challenging but important step towards improving dust treatment in simulations of evolved stars. It would also allow for a better estimation of local opacities and Eddington factor, which are essential for the proper treatment of radiation pressure on the dust-gas mixture.

We could further improve the realism by resolving the dust-gas interactions. Phantom already has several formalisms for dust-gas mixtures, either with a two-fluid approach (Laibe & Price, 2012) or a one-fluid method that keeps track of the composition of the mixture (Laibe & Price, 2014; Laibe, 2014; Price & Laibe, 2015). While the outcome of simulations with accurate treatments of dust-driven winds might be qualitatively similar to our results, it would also likely yield a more detailed structure in the winds, and lower outflow velocity and densities since our dust condensation criterion is relatively permissive.

Improvements regarding the formulation of the radiative force on dust grains would also likely impact the morphology of the wind. Esseldeurs et al. (2023) shows the difference in radiative pressure treatments for winds in binaries with an AGB star, and it is clear that more accurate approximations (e.g, Lucy 1971, 1976) yield more detailed wind structures than with a simple free-wind approximation, as well as better estimations of the wind velocities. However, such methods require the calculation of optical depth, which needs to be estimated along the line of sight of each particle and severely complicates the simulations if one wants to calculate it on the fly during an SPH simulation. This was implemented in Phantom by Esseldeurs et al. (2023) using a ray tracer algorithm, so we leave the possibility of adapting their method to our setup for follow-up studies.

3.5 Conclusions

The goal of this work was to investigate whether a companion grazing the envelope of a RSG can launch significant asymmetric episodic outflows that later expand through dust-driven winds. To do so, we performed 3D hydrodynamics simulations of a $2\,M_\odot$ star on a highly elliptical orbit around a $20\,M_\odot$ RSG with an envelope extending to $1500\,R_\odot$ (Fig. 3.1, Sec. 3.2). In our models, we see the companion grazing the RSG envelope at periastron and ejecting gas from the outermost envelope, which results in a dense semi-circular outflow (Fig. 3.4). The ejected gas becomes optically thin and cools, reaching conditions that are favourable for dust condensation. The radiative pressure on dust grains then accelerates the outflow outwards, effectively launching dust-driven winds that expand radially.

We investigated the evolution of the system through several successive grazing interactions and found that the orbit drastically tightens after each interaction (Fig. 3.5). The orbital period decreases by $\sim 3-4$ years per orbit, decreasing the periastron distance significantly and enhancing the mass loss during the grazing interaction. The outflows therefore become denser and more frequent as the system evolves, effectively altering the properties of the ejecta (Fig. 3.7). The mass ejected during each grazing interaction goes from $3 \times 10^{-4}\,M_\odot$ during to first orbit to $\sim 10^{-2}\,M_\odot$ before the onset of CEE (Fig. 3.6).

After 13 orbits (~200 years), the system enters CEE which dramatically enhances the orbital evolution and mass loss rate of the binary. Due to the large softening length of the numerical core of the RSG, we cannot resolve the CEE of the system with our simulations, therefore the outcome of the CEE remains unconstrained and could result in a short-period binary or a merger. Our simulations stop after 14 orbits, at which point the binary has ejected a total of $0.185\,M_\odot$ of gas spreading beyond $r \gtrsim 1000\,\mathrm{au}$, with 80% of this mass situated in the innermost part of the ejecta ($r \lesssim 100\,\mathrm{au}$). The final ejecta has a conical shape and shows a shell-like structure due to the shocks from each grazing by the companion.

While the initial conditions of our simulation seem relatively exotic, mostly due to the eccentricity of the system, we expect this grazing interaction to be relevant for the evolution of massive binary systems. For instance, this scenario applies to binaries with low mass MS companions with an orbit wide enough to retain a significant eccentricity, in which the stars evolve as effectively single until the massive star expands as a RSG or the orbit dramatically tightens due to the Darwin instability.

Although the duration of this phase is uncertain and depends on complicated physics near the RSG surface, it should still produce observable signatures. The dusty ejecta should be observable at millimetre/sub-millimetre wavelengths, as well as molecular lines due to the rich chemistry expected in the outflow.

Additionally, the companion should accrete matter from the outflows, which we expect to result in X-ray emission or highly ionized lines. However, their detectability is highly affected by the large intervening absorption column expected in such situations.

Lastly, the binary could evolve to a TZO after CEE if the companion is a NS, which is of interest since TZOs are hard to distinguish from RSG, and none have been unambiguously identified yet.

By comparing our results with observations of the ejecta around VY CMa, we speculate that such a grazing interaction could have been responsible for the increase in mass loss occurring about 1000 years ago (Decin et al., 2006) or more recent ejections

about 100 years ago (Humphreys et al., 2024). Some outflows around VY CMa resemble the results of our simulations, however, the observed morphology is much more complex and requires an interplay of multiple effects. Our simulations, which were only meant as a proof of concept, were performed using simple treatments of radiative cooling and winds in the outflows, and therefore require more accurate prescriptions in follow-up studies. Improving the accuracy of our simulations will allow us to study the morphology of the outflows in greater detail, as well as produce synthetic observables that can used for a better comparison with observations of VY CMa, providing a strong test for our hypothetical scenario.

We thank the anonymous referee whose comments helped to improve this work. CL thanks Shazrene Mohamed for the fruitful discussions and suggestions and Mike Lau for the help in generating stellar profiles. This research has been supported by Horizon 2020 ERC Starting Grant 'Cat-In-hAT' (grant agreement no. 803158). The work of CL has been supported by the Charles University Grant Agency project No 116324. The work of OP has been supported by the Charles University Research Program No. UNCE24/SCI/016. This work was supported by the Ministry of Education, Youth and Sports of the Czech Republic through the e-INFRA CZ (ID:90254). The simulations were performed using the Barbora cluster at IT4Innovations and the allocations provided by the projects OPEN-27-60 and OPEN-30-50.

Software: NumPy (Van Der Walt et al., 2011); Matplotlib (Hunter, 2007); Astropy (Astropy Collaboration et al., 2013); MESA (Paxton et al., 2011); Phantom (Price et al., 2018), Splash(Price, 2007).

The output files from our simulations will be shared on reasonable request to the corresponding author. The video of the snapshots of the first interaction is available at https://youtu.be/jcW0KyMayBE

Appendix A: Red supergiant profile

We need a realistic RSG profile to establish the boundary conditions (surface pressure and radius) and core size of our simple RSG interior. To obtain this stellar model, we use MESA v22.11.1 with the provided 20M_PRE_MS_TO_CORE_COLLAPSE test case to evolve a 20 $M_\odot$ zero-age main sequence star with metallicity Z=0.02 to the RSG phase without stellar winds. To produce a stellar model similar to VY CMa, we need to ensure that the stellar radius is large enough to reach very low densities in the outer envelope. As such, we looked for stellar evolution parameters for which the star expands as much as possible during the RSG phase. Similarly to Goldberg et al. (2022), we found that the largest envelopes result from a low mixing length coefficient in the H-rich envelope α_H, i.e. less efficient convection. More specifically, we found that a model with $\alpha_H = 1$ reaches about 1150 $R_\odot$ in the RSG phase while models with $\alpha_H = 3$ only expand to 1000 $R_\odot$.

We therefore choose to work with the model with the lowest mixing length and opt to analytically expand the stellar profile obtained to reach a radius of 1500 $R_\odot$. This expansion is done following homology scaling relations, which are obtained by estimating the equations of stellar structure by including the conservation of mass distribution:

$$\frac{r_\mathrm{i}(m)}{R_\mathrm{i}} = \frac{r_\mathrm{f}(m)}{R_\mathrm{f}}. \tag{3.16}$$

The new surface pressure of the star P_f scales as follows:

$$P_\mathrm{f} = P_\mathrm{i} \left(\frac{M_\mathrm{f}}{M_\mathrm{i}}\right)^2 \left(\frac{R_\mathrm{i}}{R_\mathrm{f}}\right)^4. \tag{3.17}$$

We take the effective radius of the excised core to be half of the total radius of the star, which corresponds to a softening length of $r_{\rm soft,i} = 287.5\,R_\odot$ and a core mass of $M_{\rm c} = 13.75\,M_\odot$ according to the MESA stellar profile. The radius of the core of the extended giant $r_{\rm c,f}$ is simply calculated using equation (3.16).

Following this procedure, we expand a $1150\,R_\odot$ star with $P_{\rm i} = 212$ dyn/cm^2 and $r_{\rm soft,i} = 287.5\,R_\odot$ to a $1500\,R_\odot$ star with $P_{\rm f} = 73$ dyn/cm^2 and $r_{\rm c,f} = 375\,R_\odot$. These boundary conditions are then used to solve the equations of hydrostatic equilibrium to obtain a convectively stable stellar interior model as explained in Appendix A of Lau et al. (2022). To construct this model we use an ideal gas equation of state with adiabatic index $\gamma = 5/3$ and a uniform mean molecular weight $\mu = 0.659$ (obtained from the average mean molecular weight in the envelope of the MESA model). In Fig. 3.9, we compare the detailed MESA model to the simple profiles obtained using initial conditions from MESA RSG and the extended initial conditions. Taken at face value, the density in the upper layers of the envelope is underestimated, and the density gradient is severely smoothed. This would lead to an underestimation of the outflow density and the impact of the grazing on the companion trajectory. However, the actual density profile near and above the photosphere is affected by pulsations and wind launching and likely significantly differs from a simple 1D stellar model.

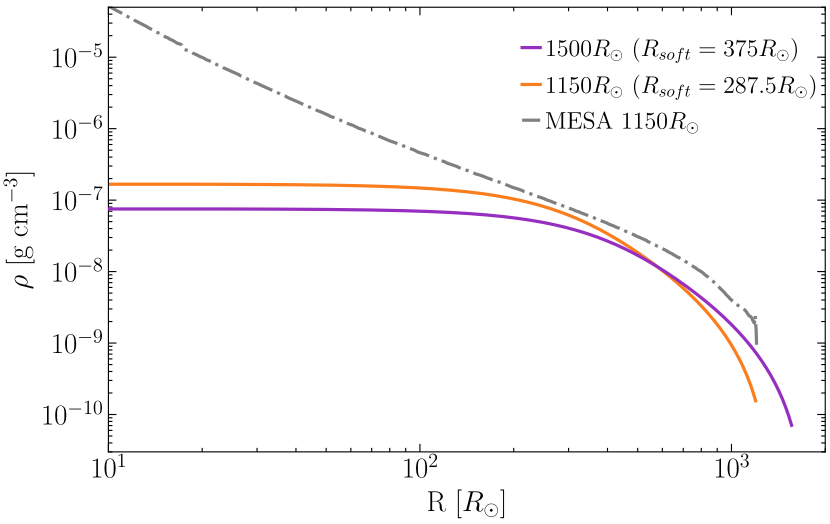

Figure 3.9: Comparison of the density profile of the RSG model obtained with MESA (grey line) with our simplified stellar profiles. The orange line shows the simplified profile calculated with the initial conditions from the MESA model, and the purple line shows the profile calculated with the expanded initial conditions.

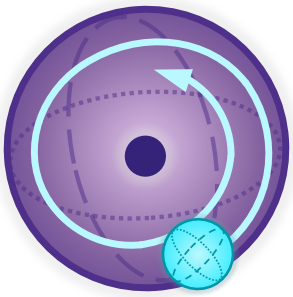

4. The Effect of Donor Star Rejuvenation on Common Envelope Evolution

Camille Landri, Paul Ricker, Mathieu Renzo,
and Alejandro Vigna-Gómez

To be submitted

Abstract

Common envelope evolution may appear as a late stage of the evolution of a binary, potentially allowing different phases of stellar interactions to occur beforehand. In particular, typical formation channels for double neutron star or black hole binaries suggest that the donor of common envelope evolution was the accretor of a previous phase stable of mass transfer, and the ensuing accretion and rejuvenation processes have substantially altered its stellar structure. The aim of this work is to study the common envelope evolution of a donor that underwent a previous phase of stable mass transfer as the accretor, and thus has a rejuvenated structure. To do so, we perform 3D hydrodynamics simulations of the common envelope evolution of a 18 $M_\odot$ supergiant and a 1.4 $M_\odot$ companion using rejuvenated and non-rejuvenated stellar models for the donor. We compare the two sets of simulations to characterise the effect of the rejuvenation on the outcome of the common envelope phase as well the shape of the ejecta. We find that accounting for a previous phase of mass transfer phase reduces the duration of the inspiral phase by a factor of two, likely due to a steeper density gradient in the outer layers of the donor. The simulations also show more equatorially concentrated and asymmetric ejecta in the rejuvenated case. The impact of rejuvenation on the unbinding of the envelope is unclear; we found that the change in unbound mass in the rejuvenated models may go from a 100% increase to 25% decrease depending on the energy criterion used.

4.1 Introduction

An important fraction of stars is found in binary systems (Abt & Levy, 1976; Bonnell et al., 2004; Duchêne & Kraus, 2013; Moe & Di Stefano, 2017), especially massive stars (Mason et al., 2009; Sana & Evans, 2010). These binary systems show a large variety of configurations, ranging from very wide systems with separation of thousands of AUs to binaries with periods of a few minutes. In the case of close binaries, with separation of $\lesssim 1$ AU, the proximity of the stars generally gives rise to interactions via mass transfer and their evolution will strongly diverge from that of a single star (Podsiadlowski et al., 1992; Sana et al., 2012; Langer, 2012; Smith, 2014b; De Marco & Izzard, 2017). In particular, close binaries commonly go through phases of stable mass transfer through Roche Lobe overflow (RLOF). During this phase, the donor star overfills its Roche Lobe, and material leaves the potential well of the donor to be accreted by the companion, altering its structure in various ways (Packet, 1981; Cantiello et al., 2007; Renzo & Götberg, 2021). In particular, A main sequence (MS) star accretor with a convective core is expected to undergo a rejuvenation process during which its core expands and increases its hydrogen content through convective mixing (Hellings, 1983). Besides increasing the lifetime of the accretor, this process also alters the structure of its core-envelope boundary (CEB) region. Recently, Renzo et al. (2023) found that the rejuvenation process lowers the binding energy of the CEB, which is of particular interest if the system later undergoes common envelope evolution (CEE) with the rejuvenated star as the donor.

CEE is a phase of binary evolution during which the secondary star plunges in the envelope of a giant primary and orbit its core (Paczynski, 1976; Ivanova et al., 2013a). The drag exerted on the companion by the envelope causes the orbit to decay as the companion transfers of energy and angular momentum to the envelope, potentially unbinding it. The outcomes of CEE are depend on the envelope ejection: a successfully ejected envelope should allow the orbit decay to slow down until the system stabilises to a short period binary, which may become a source of transient phenomena such as cataclysmic variables(Paczynski, 1976) or X-ray binaries(e.g., Kalogera & Webbink, 1998), or a double degenerate binary that may becomes a gravitational wave progenitors (e.g., Klencki et al., 2021a; Marchant et al., 2021a). On the other hand, if part of the envelope may remain bound the two stars should eventually merge. The merger may be observed as luminous red novae (Soker & Tylenda, 2006; Ivanova et al., 2013c; Pejcha et al., 2016a) or become a Thorne-Żytkow object Thorne & Zytkow (1977) if the companion is a neutron star. Thus, CEE is an important process of binary evolution that can form close binaries on relatively short timescales, and as such it has been extensively studied. It is however still unclear which physical processes are relevant during the inspiral phase of CEE (e.g. Nandez et al., 2015; Ohlmann et al., 2016; MacLeod et al., 2018; Reichardt et al., 2020; Sand et al., 2020; Lau et al., 2022).

Since the outcome of CEE strongly depends on the unbinding of the envelope, the fact that rejuvenation lowers the binding energy of the CEB is of particular interest when studying the outcome of CEE. The CEB is the region where most of the binding energy is stored, therefore a CEE with a rejuvenated donor might eject a larger part of the envelope and significantly influence the outcome of the CEE. This scenario is of interest for formation channels of binary black holes and neutron stars that expect a first phase of stable mass transfer where the accretor will later become the donor of a CEE phase (Tutukov & Yungelson, 1993; Belczynski et al., 2016; Tauris et al., 2017).

In such cases, the rejuvenation of the MS accretor during the first mass transfer phase could help unbinding its envelope when it takes the role of the donor during a later CEE.

In this paper, we aim to investigate how a past phase of mass transfer and the ensuing rejuvenation process of a CEE donor impacts the inspiral phase of CEE. To do so, we perform 3D hydrodynamics simulations of the inspiral phase of the CEE with rejuvenated and non-rejuvenated donor models of similar masses obtained by Renzo et al. (2023). We briefly describe the stellar models for the donor star as well as the setup of our hydrodynamics simulations in Section 4.2. We present the results of our simulations in Section 4.3, and discuss their implication in Section 4.4.

4.2 Numerical methods

Our simulations make use of FLASH 4.5 (Fryxell et al., 2000; Dubey et al., 2008), an adaptive mesh refinement (AMR) hydrodynamics code. We use the directionally split piecewise parabolic method (PPM) solver supplied with FLASH together with the Helmholtz equation of state, parallel FFT-based multigrid Poisson solver (Ricker, 2008; Daley et al., 2012), and a second-order leapfrog time integrator for particles. Simulations take place within a 3D Cartesian volume 72 AU on a side, with "diode" boundary conditions for hydrodynamics and isolated boundary conditions for the gravitational field.

To initialise each simulation, we begin with a 1D MESA model with mass $M_{\rm donor}$ and radius $R_{\rm donor}$ for the donor (described below). Since the star's actual core is very difficult to resolve, we replace it with a numerical core following a procedure similar to that described by Ohlmann et al. (2017). Given a choice of numerical core radius $R_{\rm core}$, to the MESA model at this radius we join a solution of the modified Lane-Emden equation representing a gaseous polytrope in the potential of a uniform-density spherical core of mass $M_{\rm core}$, which satisfies

$$\frac{d}{d\xi}\left(\xi^2\frac{d\theta}{d\xi}\right)+\xi^2(\theta^n+\theta_c^n)=0\ . \tag{4.1}$$

Here we adopt the customary definitions for the density and radius variables θ and ξ via

$$\rho\equiv\rho_0\theta^n\ ,\quad r\equiv\alpha\xi\ , \tag{4.2}$$

where ρ_0 is the central density, n is the polytropic index, and α is the scale height. This equation differs from the normal Lane-Emden equation by one term involving

$$\theta_c^n\equiv\frac{M_{\rm core}4\pi R_{\rm core}^3\rho_0}{}. \tag{4.3}$$

The density $\rho(R_{\rm core})$ and pressure $P(R_{\rm core})$ are used to determine the polytrope's specific entropy $K\equiv P/\rho^\gamma$ and thus also $\alpha^2=\frac{K(n+1)4\pi G}{\rho}^{1/n-1}_0$. The polytropic index n is set using the adiabatic index reported by the equation of state at $r=R_{\rm core}$ via $n=1/[\gamma(R_{\rm core})-1]$. Isotopic abundances are also matched and held constant throughout the polytrope. The core mass $M_{\rm core}$ and polytrope central density ρ_0 are varied in a nested pair of bisection loops until a solution that matches the density and enclosed mass at $R_{\rm core}$ is found. The part of the MESA model inside $R_{\rm core}$ is replaced by the

polytrope, and the derived core mass is used to initialise a collisionless particle at the centre of the star. The companion star is also initialised as a particle, but with mass $1.4 M_\odot$.

The particles representing the numerical donor core and the companion interact only gravitationally with the gas. The interaction is determined by computing the acceleration due to the two cores in each mesh zone and storing it as an AMR variable that is added to the finite-differenced gas potential found with the Poisson solver. The acceleration of each core due to the gas is summed during this loop in such a way as to ensure momentum conservation. The donor core and companion also experience a mutual gravitational interaction. This method differs from the technique used in previous FLASH common envelope simulations and yields greatly improved conservation properties, though because the gas gravitational acceleration is not conservatively differenced, and the time centring of the gas and particle update steps is not the same, we do not conserve momentum to within round-off error.

Once the core properties have been determined, we interpolate the modified MESA model onto the centre of the AMR grid and allow it to relax for 10 dynamical times. All the gas initialised on the grid, including the polytrope inside $R_{\rm core}$, is regarded as "envelope" material with total mass $M_{\rm env} = M_{\rm donor} - M_{\rm core}$. Outside the giant, the gas is initialised as a uniform "fluff" medium at rest with temperature and density set to approximately balance any outflow due to unresolved pressure gradients at the stellar boundary (25000 K and 10^{-12} g cm^{-3}). During this period, we damp the velocity field by multiplying all velocities by 0.9 at the end of each step. We then restart the simulation from a checkpoint file, turn off damping, and add the companion star, placing it on the x-axis at a separation $a_{\rm init}$ for which the Roche lobe radius (computed using the Eggleton (1983b) approximation) equals the MESA model's stellar radius $R_{\rm donor}$. These initial separations correspond to $843.9 R_\odot$ (period 654.6 d) and $838.5 R_\odot$ (period 641.1 d) for the rejuvenated and non-rejuvenated donors, respectively. The common envelope simulation is then run from this initial condition until the orbit stabilises; the core separation at this time ($t_{\rm final}$) is denoted by $a_{\rm final}$.

While the donor is not quite in equilibrium with the binary potential to begin with, because all runs begin with the same setup we expect the differences between them to be mainly due to the differences in the donor model.

The AMR grid is refined by applying the default FLASH second-derivative criterion to the density and pressure and by requiring refinement of blocks containing any zone whose centre is within $4 R_{\rm core}$ of a stellar core. We allow all blocks that contain a stellar core to refine to a higher maximum refinement level than those that do not. Convergence testing showed that, for the donor models considered in this paper, we required the numerical core radius to be at least 5 and preferably 10 times the smallest zone spacing $\Delta x_{\rm min}$ in order to stably relax the donor. To avoid excessive refinement of the volume, we force derefinement of blocks whose maximum density is smaller than 10^{-10} g cm^{-3} or which lie outside a distance of 18 AU from the centre of the computational volume. Each AMR block contains 8^3 zones, and the coarsest level of refinement contains 12^3 blocks.

The initial stellar profiles of the donor used in this study are part of the models computed by Renzo et al. (2023) using MESA (version 15140, Paxton et al. 2011; Paxton et al. 2013b; Paxton et al. 2015a, 2018a, 2019a). We use their non-rotating 17.84 $M_\odot$ single star for the non-rejuvenated donor and their 15 $M_\odot$ accretor that reaches 17.41 $M_\odot$ after case-B mass transfer for the rejuvenated donor. Both donors

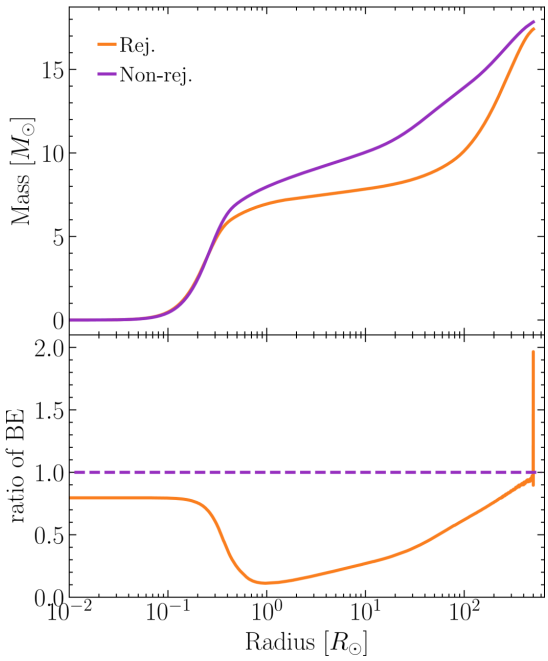

Figure 4.1: MESA stellar models for the rejuvenated (orange) and non-rejuvenated (purple) stars, assuming $\alpha_{th} = 1$. Top panel: Enclosed mass. Bottom panel: Ratio of the cumulative binding energy of the rejuvenated star to that of the non-rejuvenated star.

Table 4.1: Simulations performed for this study.

Donor	$R_{\rm core}$ ($R_\odot$)	$\Delta x_{\rm min}$ ($R_\odot$)	$M_{\rm core}$ ($M_\odot$)	$M_{\rm env}$ ($M_\odot$)
Rej.	25	5.0	7.91	9.50
	25	2.5	7.91	9.50
	12	1.26	7.68	9.64
Non-rej.	25	5.0	10.26	7.58
	25	2.5	10.26	7.58
	12	1.26	9.68	8.06

have a radius of 500 $R_\odot$, a metallicity of 0.10 $Z_\odot$, and have not started burning helium. In Figure 4.1 we show how the cumulative binding energy profiles of the two stellar models differ. The binding energy was calculated using

$$\mathrm{BE}(m, \alpha_{\rm th}) = -\int_m^M \left(-\frac{Gm'}{r(m')} + \alpha_{\rm th} u(m')\right) dm' \,, \tag{4.4}$$

where $\alpha_{\rm th}$ is the fraction of internal energy that can be used to unbind the envelope.

For each stellar model, we performed runs at several different resolutions, varying the maximum level of refinement and the number of finest-level zones per numerical core radius. Table 4.2 summarizes the different simulations, and Figure 4.2 shows the density profiles after the replacement of the core for different resolutions, as well as the initial MESA density and composition profiles.

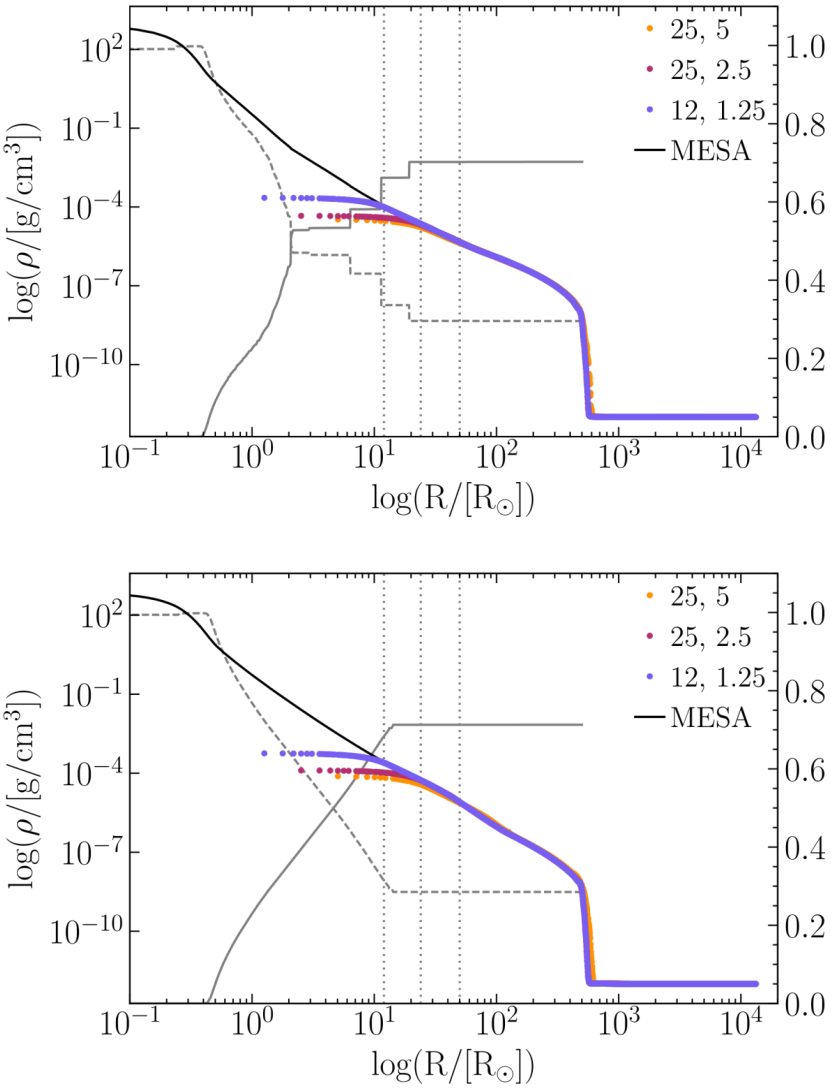

Figure 4.2: Density profiles of the donor at the start of the CEE. Runs are labelled using their numerical core radius and smallest cell size. Upper panel: rejuvenated donor. Lower panel: non-rejuvenated donor. Coloured dots represent the density profile for different resolutions, and black lines represent the initial MESA profile. The grey solid and dashed lines show the fractions of H and He, respectively. The grey dotted line shows the sum of the core radii $2R_{core} = 50R_\odot$, $2R_{core} = 24R_\odot$ and $2R_{core} = 12R_\odot$.

Model	M_{K+P} ($M_\odot$)	M_{K+P+Th} ($M_\odot$)	Time (t_{dyn})	final separation ($R_\odot$)
Rej.(25,5.0)	0.051	0.53	13.7	≤ 50
Rej.(25,2.5)	0.075	0.55	15.9	≤ 50
Rej.(12,1.26)	0.087	0.61	16.3	≤ 24
Non-rej.(25,5.0)	0.098	0.62	22.0	≤ 50
Non-rej.(25,2.5)	0.001	0.66	32.9	≤ 50
Non-Rej.(12,1.26)	0.001	0.71	31.8	≤ 24

Table 4.2: Summary of the results of the simulations. M_{K+P} and M_{K+P+Th} indicate the amount of unbound mass at the end of the simulations according to energy criteria excluding and including internal energy respectively. t_{final} is the time at which the simulation is stopped or when the cores coalesce if the orbit does not stabilise beforehand. a_{final} is the final separation of the cores, which is an upper limit if they have coalesced.

4.3 Results

We ran a total of 6 simulations, 3 for each donor model, which we summarise in three figures. First, an overview of the simulations is shown in Figure 4.3, where we show density snapshots of the Rej.(12, 1.26) and Non-rej.(12, 1.63) models at different phases of the evolution of the system. Then, we show the evolution of the binary orbit in each simulation in Figure 4.4, and finally the corresponding mass loss in Figure 4.7. In Table 4.3, we summarise the final state of each simulation at the time t_{final}, which corresponds to the time at which the orbit stabilises or the two cores coalesce.

4.3.1 Evolution of the orbit

We first examine the orbit of the binary during CEE by studying the evolution of the separation of the numerical cores, which is shown in Fig 4.4 for both rejuvenated and non-rejuvenated models. This evolution can be broadly divided into two phases. First, the orbit slowly loses stability as the companion grazes the outer envelope of the donor, and its eccentricity increases which gives rise to broad modulations of the separation after $\sim$ 1 year. When the companion plunges into the envelope of the donor, the orbital decay accelerates and the inspiral phase starts, yielding a much steeper evolution of the binary separation until the orbit stabilises. As indicated by the tighter orbital variations of the separation, the binary remains eccentric during the whole inspiral phase, even after the orbit regains its stability.

While we observe the same overall evolution for the two donor models, we note a change of pace in the inspiral between the two sets of simulations. The slow grazing of the orbit lasts around two years for rejuvenated donors, but it takes six years for the companion to start the fast inspiral in the envelope of the non-rejuvenated donor. This can be seen from the third row of Figure 4.3, where the companion is already inside the envelope of the rejuvenated donor and drives significant outflows, while the non-rejuvenated system is still in the grazing phase, with less gas ejected. The speed of the fast phase of inspiral is also slightly affected: it takes about two years for the companion to reach a stable orbit in the rejuvenated donor, against almost three years in the non-rejuvenated case. As a result, the binary with a rejuvenated donor reaches the minimum separation between cores after 4.5 years, while the non-rejuvenated inspiral

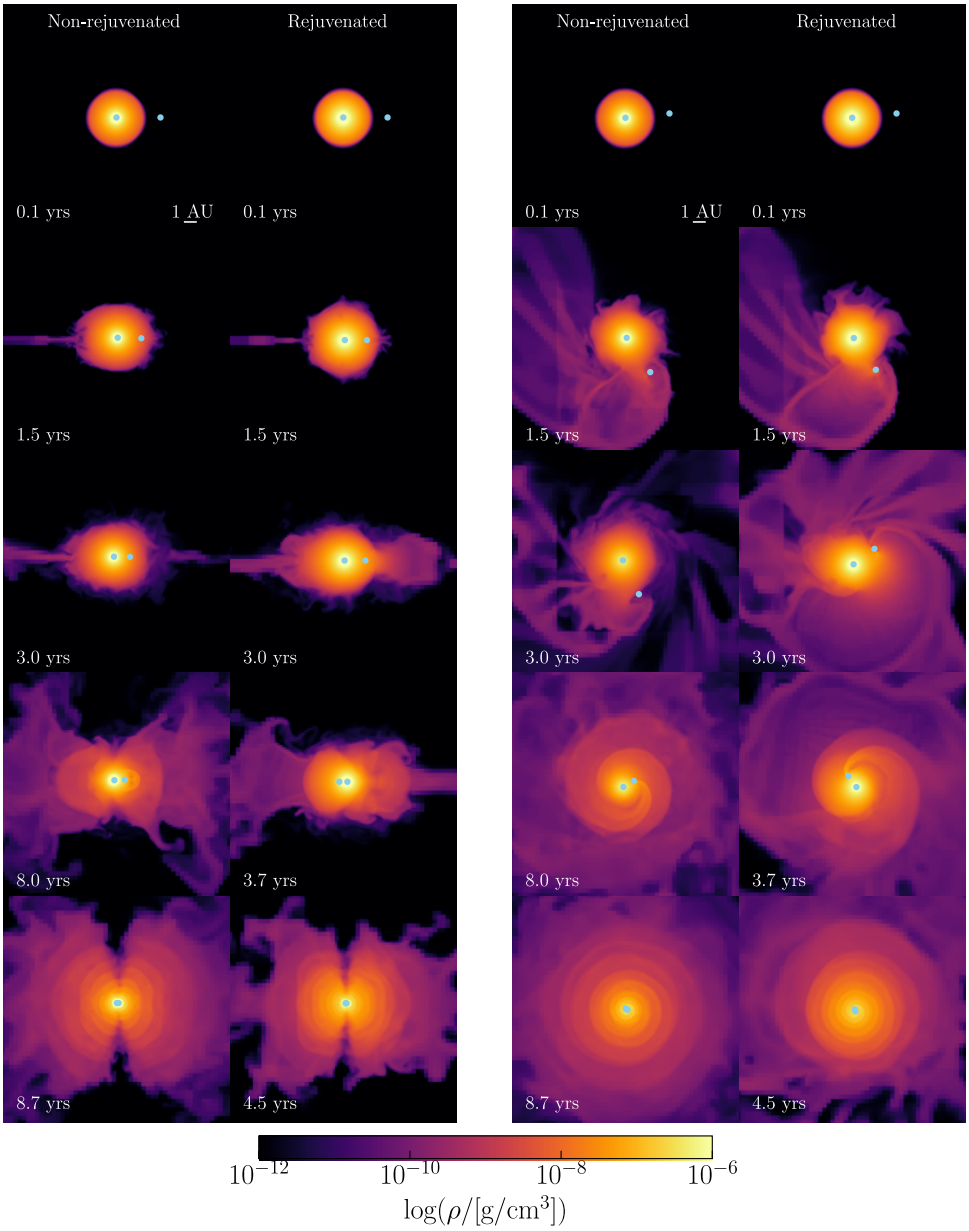

Figure 4.3: Snapshots of the Rej.(12, 1.26) and Non-rej.(12, 1.63) runs in the equatorial plane (left) and in the meridional plane (right). Each panel shows a density slice at z=0 and is 20 by 20 A.U. The donor core and companion are denoted as grey points. Left panels: run with non-rejuvenated donor Non-rej.(12, 1.26). Bottom panels: run with rejuvenated donor Rej.(12, 1.26). First row: start of the run. Second and third row: first grazing of the envelope of the donor by the companion. Fourth row: core-companion separation is around 1 A.U. Fifth row: core-companion separation is 2 R_{core}.

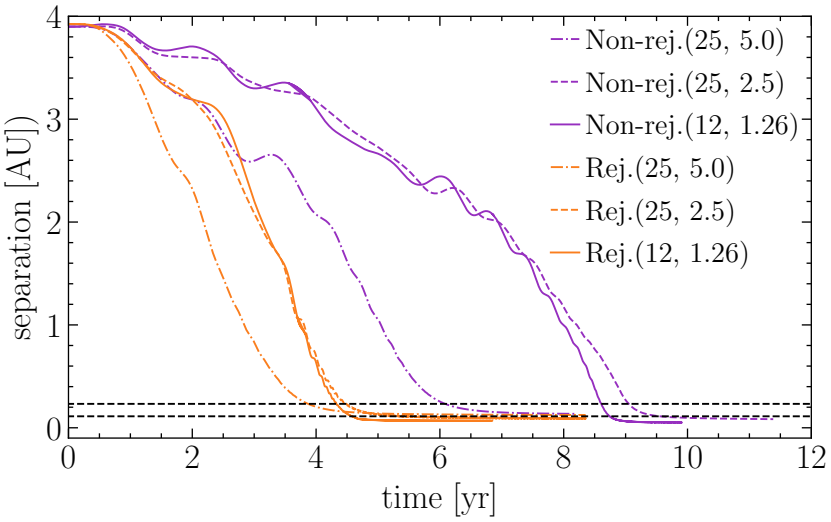

Figure 4.4: Evolution of the separation of the cores during the CEE for both rejuvenated (orange) and non-rejuvenated (purple) donors at different resolution. The black dashed lines denote where the separation is equal to the sum of the core radii $2R_{core} = 50R_{\odot}$, and $2R_{core} = 24R_{\odot}$.

takes almost 9 years.

Finally, we remark that while our simulations show stabilised orbits, the separation of the binaries has reached $2R_{\rm core}$ before the orbit has become stable. Considering the density of the gas inside the domain delimited by the numerical cores is much lower than the density in the stellar profiles, the gravitational drag and torques between the companion and the gas are very likely underestimated. As such, we do not take any results after the cores have coalesced as physically meaningful and consider that the orbit of the cores did not manage to stabilise in any of our simulations. It is thus impossible to conclude whether the stellar cores will merge or stabilise in a tight orbit by the end of the inspiral phase, and we can only derive an upper limit on the final separation of the binary.

4.3.2 Outflows

We show the evolution of the shape of the envelope during the simulation in Figure 4.3. In the final snapshots, taken before the cores coalesce, we see the expected over-densities due to the inspiral of the companion in both donor models, but the spirals appear slightly tighter and more concentrated towards the centre of the binary in the case of the rejuvenated donor. From the slices in both the equatorial and the meridional planes, we see that the non-rejuvenated envelope has spread further by the end of the simulation than the rejuvenated envelope. The outflow also appears more spherically symmetric in the non-rejuvenated case. Additionally, the slices of the meridional plane of the envelope show strong spherical asymmetries, with a large decrease in density around the polar axis of both models. In particular, the matter distribution in the rejuvenated envelope appears very asymmetric with respect to the z-axis of the grid.

We inspect the shape of the ejecta and the envelope at the end of the simulation in Figure 4.6 and Figure 4.5, in particular, we are interested in the sphericity of the

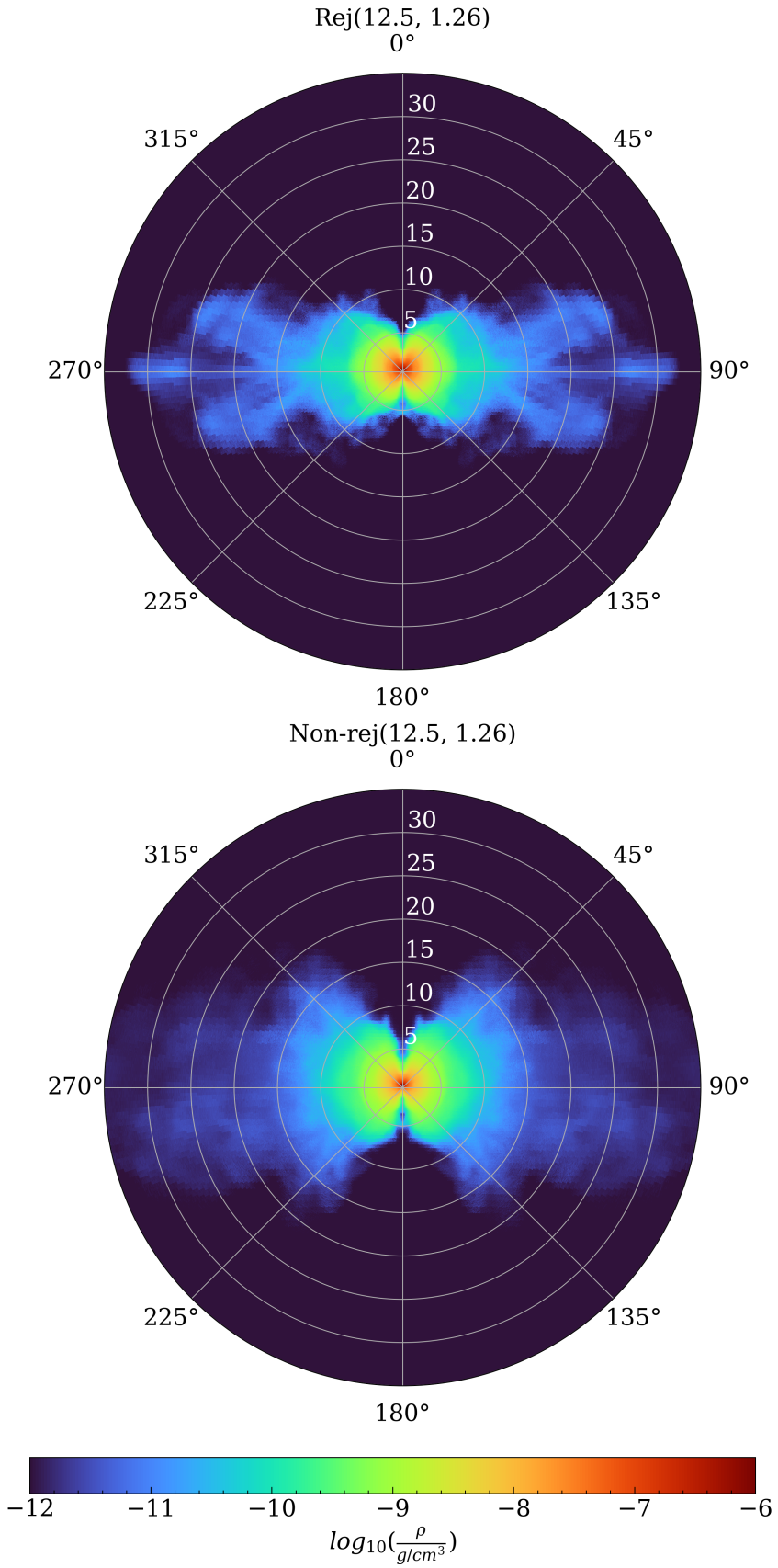

Figure 4.5: Azimuthally averaged density of the (12, 1.26) models. The top and bottom panels show the rejuvenated and non-rejuvenated models respectively.

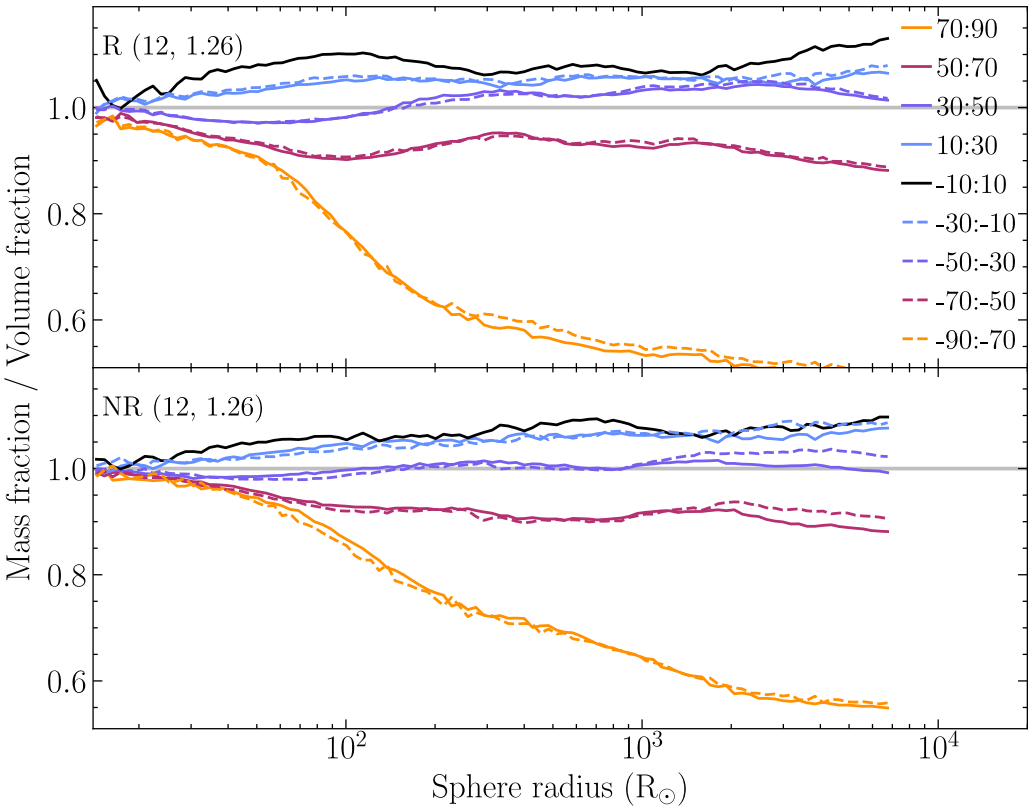

Figure 4.6: Mass distribution of the envelope at different radii when the cores coalesce for Rej.(12, 1.26) (top panel) and Non-rej(12, 1.26) (bottom panel). We investigate the mass distribution in spheres of different radii that are sectioned in bins of polar angle θ. To remove the issues due to fewer cells around the poles, we calculate the ratio of its mass fraction over its volume fraction for each section. The mass distribution within a sphere is spherical if this ratio is one for all polar bins. Each line shows a different polar angle bin and the radius of the spheres is the x-axis.

outflow. Figure 4.5 shows the azimuthally averaged density of the gas right before the cores coalesce in the case of the rejuvenated and non-rejuvenated (12, 1.26) models. Both models have non-spherical outflow with substantial under-densities in the polar regions, but the ejecta is much more equatorially concentrated in the case of the rejuvenated donor. To quantify how spherical the mass distribution is at different radii, we look at the ratio of enclosed mass in spheres of increasing radius to a spherical mass distribution. To assess the polar distribution of the gas, we section these spheres according to polar angle bins. Since our grid is cartesian, some polar bins will contain more cells than others, which introduces errors when calculating the mass fraction (mass of the sector over the total mass of the sphere) of a bin. To avoid this issue, we divide the mass fraction of the bin by its volume fraction (the volume of the sector over the total volume of the sphere). If this ratio is equal to one for all polar bins, then the mass distribution in the sphere is spherical. The result of this analysis, shown in Figure 4.6, indicates that most of the ejecta is concentrated in the range of polar angle $\theta = [-50°, 50°]$, leaving the polar regions mostly empty. In the case of the rejuvenated envelope, the asphericity of the gas is strong even in the inner regions of the ejecta ($R < 50R_\odot$), whereas the mass distribution of the inner non-rejuvenated envelope is closer to a spherical distribution.

4.3.3 Mass loss

In Fig 4.7 we show the amount of envelope mass lost in our simulations until the numerical cores coalesce. A parcel of gas is considered unbound if it exits the domain or if its kinetic energy is greater than its potential energy:

$$E_{\rm gr} + E_{\rm kin} > 0. \tag{4.5}$$

Alternatively, we can assume that part of the internal energy of the gas $\alpha E_{\rm int}$ is converted into kinetic energy, and the state of a gas element is determined by

$$E_{\rm gr} + E_{\rm kin} + \alpha_{\rm th} E_{\rm int} > 0. \tag{4.6}$$

$\alpha_{\rm th}$, the parameter describing how much internal energy is transferred, is generally unconstrained, and setting it to unity allows to obtain an upper limit on the ejected mass. Naturally, the more conservative criteria of equation (4.5) serves as a lower limit. We note that since all the binaries reach their minimum separation of $2R_{core}$ in our simulations, a part of the inspiral is not resolved. Therefore, we can only find a lower limit to the total mass lost by the envelope during the CEE of our systems.

We first notice that the rejuvenation of the donor does affect the amount of mass lost: the rejuvenated giant loses up to $0.06M_{\rm env}$ while the non-rejuvenated one loses up to $0.09M_{\rm env}$ when considering the less conservative criterion (Equation 4.6) for mass loss. Both donor models do not yield large mass loss, though the mass loss increases by 50% when considering the non-rejuvenated case.

Interestingly, this trend reverses when considering the more conservative criterion (Equation 4.5) for mass loss. The mass loss in the rejuvenated systems reaches $0.015M_{\rm env}$ against $0.01M_{\rm env}$ in the non-rejuvenated case, effectively showing a 50% increase when taking rejuvenation into account, which is likely due to the faster orbital decay and the overall lower binding energy of the inner layers of the envelope. The strong difference between the two energy criteria remains during the whole simulation,

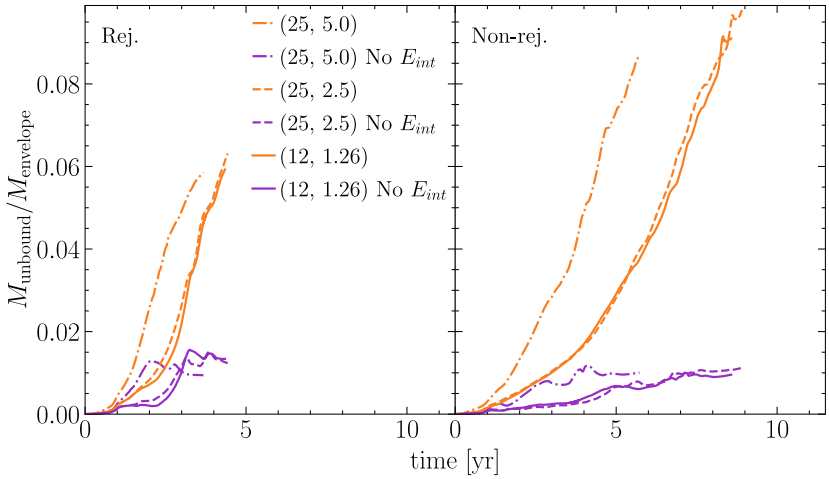

Figure 4.7: Evolution of the amount of unbound mass during the CEE for different resolutions and donor models. Orange lines show the unbound mass considering the total energy is calculated using only the potential and kinetic energy of each cell. Purple lines show the unbound mass considering the total energy is calculated using the potential, kinetic and internal energy of each cell. Mass is considered unbound if its total energy is positive or if it has left the domain. Left panel: Simulations with a rejuvenated donor. Right panel: Simulations with a non-rejuvenated donor.

suggesting that the internal energy of the gas is inefficiently converted to kinetic energy, but it is possible that this conversion of energy occurs later in the inspiral and we simply do not reach this point in our simulations.

Overall, the total mass unbound by the CEE in our simulations is low, which is consistent with the cores merging. However, the resolution of our simulation is too low to resolve the late phase of the inspiral, which could lead to a higher mass loss rate and potentially the stabilisation of the binary orbit.

4.4 Discussion

4.4.1 Orbital decay and unbinding efficiency

The main goal of this work was to investigate whether the significant difference in binding energy across the envelope of rejuvenated and non-rejuvenated donors, as shown in Figure 4.1, would affect the inspiral phase of CEE and change the outcome of the CEE.

The most significant difference between the two CEE simulations is the speed of the inspiral phase. As seen in Figure 4.4, the rejuvenated inspiral is about twice as fast as in the non-rejuvenated case. This is likely due to the abrupt increase in density and binding energy at the surface of the rejuvenated donor. The top panel of Figure 4.1 shows that a lot more mass is contained in the surface layers of the rejuvenated model compared to the non-rejuvenated case, which is a result of past accretion phases. These more massive outer layers exert a stronger gravitational drag on the companion as it grazes the envelope of the donor, which causes a stronger orbital decay and thus a much faster inspiral phase.

On the other hand, the difference in unbinding efficiency between the two donor models is less substantial. From Figure 4.7, we do find an increase in mass loss in the rejuvenated models when considering the conservative energy criteria. However, including the internal energy in the energy criteria of the models shows the opposite results: the non-rejuvenated envelope is more efficiently unbound due to a higher internal energy content of the non-rejuvenated models. Since the contribution of internal energy to envelope unbinding is unconstrained, it is unclear whether the non-rejuvenated CEE is actually more efficient than the rejuvenated case.

Overall, these results are severely limited by our resolution. Firstly, the largest difference in binding energy profiles in the two stellar models is situated in the innermost layers of the envelope ($r \sim 10^0 - 10^1\ R_\odot$, see Figure 4.1), which are not resolved with our current best resolution. Thus, simulating the CEE with lower core radii and minimum cell size is required to properly assess the impact of rejuvenation on envelope ejection. Furthermore, increasing the resolution would also result in a longer inspiral phase before the cores coalesce or stabilise, thus improving the prediction of the outcome of the inspiral. Additionally, correctly resolving the CEE on longer timescales may lead to an increase in mass loss due to a late conversion of internal energy to kinetic energy. Finally, since the mass loss in the systems considered in this study is very low it may be of interest to study the effect of rejuvenation in systems with binary parameters allowing larger unbinding efficiencies. For instance, considering a donor with lower initial mass can drastically increase the amount of mass lost during the inspiral, in which case the effect of previous rejuvenation may be much stronger.

4.4.2 Morphology of the ejecta

As seen in Figures 4.3, 4.5, and 4.6, one of the strong differences between our rejuvenated and non-rejuvenated simulations is the shape of the ejecta. While the ejecta is far from spherically symmetric in both cases, it is significantly more equatorially concentrated in the rejuvenated models. The differences in the symmetries and compactness of the ejecta are likely due to the different speeds at which the companion spirals in. In particular, a slower inspiral gives more time for the outflow to spread further out, which explains why the non-rejuvenated envelope is much more extended at the end of the simulation.

The ejecta asymmetries do not directly impact the CEE, however, they do have observational consequences as the ejected envelope expands and cools to the proper conditions for dust condensation. Thus, the resulting dusty CSM around the remnant of the CEE, which should be observable at least in infrared, has a significantly different geometry and mass distribution if rejuvenation is taken into account. This may also impact the observational signatures of later interactions with the CSM.

Since the companion is a neutron star, the merger may produce a Thorne-Żytkow object (TZO) (Thorne & Zytkow, 1977), or lead to collapse into a black hole accompanied by a strong supernova (SN) explosion (Chevalier, 1996; Fryer & Woosley, 1998). In the second case, the dense circumstellar medium resulting from the CEE ejection will interact with the SN explosion (e.g., Smith, 2011; Chevalier, 2012; Metzger, 2022), potentially yielding a type IIn SN or an ultraluminous SN. The different equatorial concentrations and asymmetries observed between the rejuvenated and non-rejuvenated will impact the interaction between the circumstellar medium and a future SN, which may in turn affect the observed properties of the interacting SN and the remnant.

4.4.3 Including other phases of binary evolution

Our simulations indicate that considering one previous phase of mass transfer significantly impacts CEE. However, there are other phases of binary evolution that may substantially impact the structure of a future CEE donor and thus the details of the CEE process. In particular, we found that the change in the mass distribution in the outer layers of the donor accelerated the inspiral phase, thus, any process that impacts these regions could be relevant.

We considered a system that evolved through a typical double NS binary formation channel (e.g., Tauris et al., 2017). This evolutionary process starts with two massive MS stars in a close orbit, such that the system undergoes a phase of case B stable mass transfer when the more massive star evolves out of its MS phase and expands. The donor is gradually stripped of its mass while the MS accretor gains mass and undergoes a rejuvenation process. Eventually, the stripped donor collapses and turns into a NS without disrupting the binary Renzo et al. (2019). The initially less massive star later expands when leaving its MS phase, eventually leading to a second phase of mass transfer that becomes unstable and leads to CEE.

While the first phase of mass transfer is accounted for in the stellar models used in this work (Renzo et al., 2023), the effects of the SN explosion and the second phase of mass transfer have been neglected. In particular, the ejecta due to the SN explosion may interact with the companion (e.g., Hirai et al., 2018; Ogata et al., 2021), injecting energy into its outer envelope, which would cause an expansion and possibly ablating part of the surface layers. Additionally, the phase of mass transfer directly preceding the onset of CEE should also affect the donor, in particular through the removal of its outer layers. These two processes may remove some of the dense outer layers of the donor that formed through the first phase of mass transfer, thus mitigating the increase in inspiral pace while maintaining a lower binding energy profile across the stellar envelope. Including these two other phases of the evolution of the binary may therefore yield different results than what we observed in our simulations.

4.5 Conclusion

In this work, we have performed 3D hydrodynamics simulations of CEE using donor models that account for a previous phase of mass transfer. This mass transfer phase induced a rejuvenation process in the future donor of the CEE phase, which greatly lowers its binding energy in the innermost envelope. We compare the outcome of the CEE process in our simulations by using rejuvenated and non-rejuvenated donor models and found that rejuvenation does impact the speed of the inspiral, the shape of the ejecta, and the amount of mass lost by the system during the inspiral.

The main difference observed when a past phase of mass transfer is accounted for is a twice-faster inspiral phase. This is likely due to the denser outer layers of the donor resulting from past accretion, which strengthens the drag on the companion when it starts to plunge into the envelope. In both rejuvenated and non-rejuvenated cases, we found that the orbit of the binary does not stabilise before the numerical cores coalesce, though this may change when increasing the resolution of the simulations.

On the other hand, the impact of donor rejuvenation on the mass loss of the system is less clear. We found a 100% increase in unbound mass with the rejuvenation when using the conservative energy criteria, but a 33% decrease when including the internal

energy of the gas. The unbinding efficiency of the system is overall very low, with up to 6% and 9% of the envelope mass ejected in the rejuvenated and non-rejuvenated case respectively. Therefore, it is complicated to assess the full impact of rejuvenation on mass ejection, and simulation of different mass ratios may help in that regard.

A side effect of using rejuvenated stellar models was a change in ejecta morphology: the rejuvenated ejecta is more equatorially concentrated and less spherically symmetrical than in our non-rejuvenated models. This difference mostly has observational consequences, especially if the inspiral ends in a merger. In particular, the ensuing LRN and a potential later SN explosion of the merger product may have different properties if the mass distribution of the CEE ejecta is different.

We note that due to numerical limitations, our simulations have relatively large core sizes that do not allow to resolve the innermost part of the inspiral, where the difference in binding energy is supposed to be the strongest. Therefore, simulations with smaller core sizes and higher resolution are needed to study the full impact of rejuvenation.

Our simulations only considered a specific phase of the typical binary evolution channel for double NS binaries, but the results indicate that any significant structural changes in the stars occurring during binary interactions are relevant for later CEE. Thus, taking into account the whole binary evolution before the onset of CEE, in particular a previous SN explosion and the mass transfer phase preceding CEE may change these results.

This project was initiated at the 2023 Kavli Summer Program in Astrophysics held at the Max Planck Institute for Astrophysics (MPA). We thank MPA and the Kavli Program for their support. The work of CL has been supported by Horizon 2020 ERC Starting Grant 'Cat-In-hAT' (grant agreement no. 803158) and the Charles University Grant Agency project No 116324. This work was supported by the Ministry of Education, Youth and Sports of the Czech Republic through the e-INFRA CZ (ID:90254). PR acknowledges support from the US National Science Foundation under AAG 20-09868. FLASH was developed and is maintained largely by the DOE-supported Flash Center for Computational Science at the University of Chicago (now at the University of Rochester). Simulations were performed using the Barbora cluster at IT4Innovations (projects OPEN-27-60 and OPEN-30-50), using Stampede2 at the Texas Advanced Computing Center (NSF ACCESS PHY230145), and using computational resources at MPA and Charles University.

Software: FLASH (Fryxell et al., 2000; Dubey et al., 2008), yt (Turk et al., 2011), Matplotlib (Hunter, 2007), NumPy (Harris et al., 2020)

Conclusion

In this thesis, we showed that stars evolving in close binaries are often strongly impacted by the stellar interactions they undergo. These interactions significantly affect stellar evolution and are at the root of many interesting astrophysical phenomena, such as mergers and cataclysmic variables. Furthermore, observations show that such interactions occur in a diverse range of binary systems, from long-lived low-mass systems to massive binaries evolving into gravitational wave sources. As such, binary interactions are a key aspect of stellar astrophysics and time-domain astronomy. While our understanding of binary evolution has advanced since the first observation of binary stars, the diversity of binary configurations and the ensuing evolutionary paths require detailed investigations of specific types of close binaries and their interactions. In this thesis, we carried out separate studies of different binary interactions to explore known issues in binary and stellar evolution, aiming to constrain existing and new types of interactions either by analysing observational data or carrying out hydrodynamics simulations.

We first investigated accreting binaries, specifically dwarf novae, a type of cataclysmic variable with thermally unstable accretion discs. While it is well known that these systems undergo periodic outbursts due to thermal instabilities propagating through the disc, there are persistent discrepancies between observations and modes of unstable accretion discs. In Chapter 2, we discussed the potential extreme dwarf nova O-201843, which shows very long outbursts that resemble those of dwarf novae, albeit on much longer timescales and with numerous peculiar features. Through the analysis of photometric and spectroscopic observations, we show that the outbursts originate from a relatively cold accretion disc undergoing thermal instabilities. Aside from the unusually young companion observed in the spectra and the small recurring flares, this system undergoes a slow brightening before each outburst, a feature predicted by disc instability models but never observed. Since these models have always been considered incomplete due to this discrepancy, O-201843 could help bridge the gap between current models and observations of thermal instabilities in accretion discs. A first step in this direction is to perform follow-up time-resolved spectroscopy and better constrain the characteristics of the system, including the primary and secondary, and possibly use Doppler tomography to characterise the velocity structure of the disc.

Another important issue we explored in this work is the mass loss phases experienced by red supergiants, of which the origin is still very unconstrained, resulting in large uncertainties in massive star evolution and many unexplained features in observations of red supergiants. While different processes, such as convection or magnetic activity, have been considered to explain asymmetric mass ejection in red supergiant stars, little attention has been given to the potential role of binarity and stellar interactions in driving these outflows. In Chapter 3, we performed 3D hydrodynamics simulations to investigate whether a $2\,M_{\odot}$ companion grazing the envelope of a $20\,M_{\odot}$ RSG at periastron can launch significant asymmetric episodic outflows that later expand through dust-driven winds. Our simulations show that each periastron passage decreases the orbital separation and increases the mass loss rate, yielding a broad asymmetric ejecta of $0.185\,M_{\odot}$ before the system enters common envelope evolution. The dusty ejecta should be observable at millimetre and sub-millimetre wavelengths,

and the similarities between our simulations and some of the outflows observed around the red supergiant VY CMa show that this grazing interaction may be relevant for the evolution of massive stars. This scenario applies to binaries with low-mass MS companions as well as systems that may become double neutron star binaries and thus require further investigation to constrain its impact on binary and stellar evolution. Our simulations are meant as proof-of-concept, and improving the treatment of the physical processes included will allow us to make more accurate predictions. Another necessary follow-up will be to study the interplay between this interaction and other potential outflow mechanisms, such as convective motion in the envelope, magnetic surface activity, and pulsations.

Finally, we studied common envelope evolution, a key phase of binary evolution where the binary orbit drastically tightens due to the drag of the shared envelope on the inspiralling companion. There remain many unknowns concerning this process, such as the physical processes relevant to the unbinding of the envelope, the initial conditions of the common envelope, or the conditions allowing for the total ejection of the envelope. In particular, an important aspect that is often neglected in simulations is the history of binary evolution, in particular its impact on the structure of the donor and thus on the outcome of common envelope evolution. In Chapter 4, we have performed 3D hydrodynamics simulations of the common envelope evolution of a $18\,M_\odot$ giant donor with a $1.4\,M_\odot$ companion, a system binary that has supposedly undergone at least one previous phase of mass transfer and may later result in a double neutron star system. We used a donor model that accounts for a previous phase of mass transfer and specifically the effect of the rejuvenation process. By comparing the results with a second set of simulations performed with a single star profile for the donor, we found that past rejuvenation increases the speed of the inspiral and the ejecta asymmetries and does impact the amount of mass lost during the inspiral. We mostly attribute this change to the larger density at the surface of rejuvenated stellar models due to previous accretion, which strengthens the drag on the companion during the early inspiral. While simulations of higher resolution are necessary to fully assess the impact of rejuvenation on the outcome of common envelope evolution, it is clear that the effect is not negligible. It will be interesting to study how other phases of binary evolution may alter this result, for instance, the phase of unstable mass transfer triggering the common envelope evolution or the supernova explosion of the companion. Moreover, it is of high importance to study this process for different binary parameters, e.g., stellar masses, to provide more accurate initial conditions for common envelope simulations.

Bibliography

Abramowicz M., Jaroszynski M., Sikora M., 1978, A&A, 63, 221

Abril J., Schmidtobreick L., Ederoclite A., López-Sanjuan C., 2020, MNRAS, 492, L40

Abt H. A., Levy S. G., 1976, The Astrophysical Journal Supplement Series, 30, 273

Abt H. A., Gomez A. E., Levy S. G., 1990, ApJS, 74, 551

Astropy Collaboration et al., 2013, Astronomy and Astrophysics, 558, A33

Aydi E., Mohamed S., 2022, MNRAS, 513, 4405

Bailey J., 1975, Journal of the British Astronomical Association, 86, 30

Balbus S. A., Hawley J. F., 1991, ApJ, 376, 214

Barnes J., Hut P., 1986, Nature, 324, 446

Belczynski K., Holz D. E., Bulik T., O'Shaughnessy R., 2016, Nature, 534, 512

Berger M. J., Colella P., 1989, Journal of Computational Physics, 82, 64

Berger M. J., Oliger J., 1984, Journal of Computational Physics, 53, 484

Bermúdez-Bustamante L. C., et al., 2024, arXiv e-prints, p. arXiv:2401.03644

Bermúdez-Bustamante L. C., García-Segura G., Steffen W., Sabin L., 2020, MNRAS, 493, 2606

Bermúdez-Bustamante L. C., et al., 2024, Dust formation in common envelope binary interactions – II: 3D simulations with self-consistent dust formation, `http://arxiv.org/abs/2401.03644`

Bladh S., Höfner S., 2012, A&A, 546, A76

Blagorodnova N., et al., 2021, A&A, 653, A134

Bobinger A., Barwig H., Fiedler H., Mantel K.-H., Šimić D., Wolf S., 1999, A&A, 348, 145

Bondi H., Hoyle F., 1944, MNRAS, 104, 273

Bonnell I. A., Vine S. G., Bate M. R., 2004, Monthly Notices of the Royal Astronomical Society, 349, 735

Bowen G. H., 1988, ApJ, 329, 299

Brackbill J. U., Barnes D. C., 1980, Journal of Computational Physics, 35, 426

Brandt N., Podsiadlowski P., 1995, MNRAS, 274, 461

Bruch A., 2017, New Astronomy, 57, 51

Burki G., Mayor M., 1983, A&A, 124, 256

Cannizzo J. K., Wheeler J. C., Ghosh P., 1982, NASA STI/Recon Technical Report N, 83, 23253

Cantiello M., Yoon S. C., Langer N., Livio M., 2007, Astronomy and Astrophysics, 465, L29

Chen X., Han Z., Tout C. A., 2011, ApJ, 735, L31

Chen Z., Ivanova N., Carroll-Nellenback J., 2020, ApJ, 892, 110

Chevalier R. A., 1996, ApJ, 459, 322

Chevalier R. A., 2012, ApJ, 752, L2

Choi J., Dotter A., Conroy C., Cantiello M., Paxton B., Johnson B. D., 2016, ApJ, 823, 102

Clayton M., Podsiadlowski P., Ivanova N., Justham S., 2017a, MNRAS, 470, 1788

Clayton M., Podsiadlowski P., Ivanova N., Justham S., 2017b, MNRAS, 470, 1788

Colella P., Woodward P. R., 1984, Journal of Computational Physics, 54, 174

Courant R., Friedrichs K., Lewy H., 1967, IBM Journal of Research and Development, 11, 215

Cropper M., 1990, Space Sci. Rev., 54, 195

Daley C., Vanella M., Dubey A., Weide K., Balaras E., 2012, Concurrency and Computation: Practice and Experience

Darwin G. H., 1879b, Proceedings of the Royal Society of London Series I, 29, 168

Darwin G. H., 1879a, Proceedings of the Royal Society of London Series I, 29, 168

De Marco O., Izzard R. G., 2017, Publications of the Astronomical Society of Australia, 34, e001

Decin L., Hony S., de Koter A., Justtanont K., Tielens A. G. G. M., Waters L. B. F. M., 2006, A&A, 456, 549

Decin L., et al., 2016, A&A, 592, A76

Dehnen W., Aly H., 2012, MNRAS, 425, 1068

Dhillon V. S., Smith D. A., Marsh T. R., 2013, Monthly Notices of the Royal Astronomical Society, 428, 3559

Dinh-V-Trung Bao N. T. T., Tien P. M., Hai B. V., Minh P. H., Khiem L. H., 2022, AJ, 164, 219

Dorda R., Patrick L. R., 2021, MNRAS, 502, 4890

Dotter A., 2016, ApJS, 222, 8

Drout M. R., Götberg Y., Ludwig B. A., Groh J. H., de Mink S. E., O'Grady A. J. G., Smith N., 2023, Science, 382, 1287

Dubey A., Reid L. B., Fisher R., 2008, Physica Scripta, T132, 014046

Dubus G., Otulakowska-Hypka M., Lasota J.-P., 2018, Astronomy and Astrophysics, 617, A26

Duchêne G., Kraus A., 2013, Annual Review of Astronomy and Astrophysics, 51, 269

Eggleton P. P., 1983b, The Astrophysical Journal, 268, 368

Eggleton P. P., 1983a, ApJ, 268, 368

Eggleton P. P., Kiseleva-Eggleton L., 2001, ApJ, 562, 1012

Ekström S., et al., 2012, A&A, 537, A146

El-Badry K., Seeburger R., Jayasinghe T., Rix H.-W., Almada S., Conroy C., Price-Whelan A. M., Burdge K., 2022, MNRAS, 512, 5620

El Mellah I., Sander A. A. C., Sundqvist J. O., Keppens R., 2019, A&A, 622, A189

Eldridge J. J., Fraser M., Smartt S. J., Maund J. R., Crockett R. M., 2013, MNRAS, 436, 774

Eldridge J. J., Stanway E. R., Xiao L., McClelland L. a. S., Taylor G., Ng M., Greis S. M. L., Bray J. C., 2017, Publ. Astron. Soc. Australia, 34, e058

Esseldeurs M., et al., 2023, A&A, 674, A122

Evans C. R., Hawley J. F., 1988, ApJ, 332, 659

Farmer R., Renzo M., Götberg Y., Bellinger E., Justham S., de Mink S. E., 2023, MNRAS, 524, 1692

Faulkner J., Lin D. N. C., Papaloizou J., 1983, Monthly Notices of the Royal Astronomical Society, 205, 359

Ferland G. J., et al., 2017, Rev. Mex. Astron. Astrofis., 53, 385

Fontaine G., Brassard P., Bergeron P., 2001, PASP, 113, 409

Fragos T., Andrews J. J., Ramirez-Ruiz E., Meynet G., Kalogera V., Taam R. E., Zezas A., 2019, ApJ, 883, L45

Freytag B., Höfner S., 2023, A&A, 669, A155

Fryer C. L., Woosley S. E., 1998, ApJ, 502, L9

Fryxell B., et al., 2000, The Astrophysical Journal Supplement Series, 131, 273

Gagnier D., Pejcha O., 2023, A&A, 674, A121

Gagnier D., Pejcha O., 2024, A&A, 683, A4

Gaia Collaboration 2018, Astronomy & Astrophysics, 616, A1

Gaia Collaboration 2021, Astronomy & Astrophysics, 650, C3

Gail H. P., Sedlmayr E., 1988, A&A, 206, 153

Gail H.-P., Sedlmayr E., 2013, Physics and Chemistry of Circumstellar Dust Shells. Cambridge University Press, https://ui.adsabs.harvard.edu/abs/2013pccd.book.....G

Gail H. P., Keller R., Sedlmayr E., 1984, A&A, 133, 320

Gauger A., Gail H. P., Sedlmayr E., 1990, A&A, 235, 345

Gingold R. A., Monaghan J. J., 1977, MNRAS, 181, 375

Glanz H., Perets H. B., 2018a, MNRAS, 478, L12

Glanz H., Perets H. B., 2018b, MNRAS, 478, L12

Glanz H., Perets H. B., 2021, MNRAS, 507, 2659

Gnedin N. Y., Abel T., 2001, New Astron., 6, 437

Godunov S. K., 1959, Mat. Sb., Nov. Ser., 47, 271

Goldberg J. A., Jiang Y.-F., Bildsten L., 2022, ApJ, 929, 156

Goliasch J., Nelson L., 2015, ApJ, 809, 80

González-Bolívar M., De Marco O., Lau M. Y. M., Hirai R., Price D. J., 2022, MNRAS, 517, 3181

González-Bolívar M., De Marco O., Lau M. Y. M., Hirai R., Price D. J., 2022, Monthly Notices of the Royal Astronomical Society, 517, 3181

Gordon M. S., et al., 2019, AJ, 157, 57

Götberg Y., et al., 2023, ApJ, 959, 125

Gottlieb A. M., Eikenberry S. S., Ackley K., DeWitt C., Marco A., 2020, ApJ, 896, 32

Hameury J.-M., 2020, Advances in Space Research, 66, 1004

Hameury J.-M., Lasota J.-P., 2021, Astronomy & Astrophysics, 650, A114

Han Z., Boonrucksar S., Qian S., Xiaohui F., Wang Q., Zhu L., Dong A., Zhi Q., 2020, PASJ, 72, 76

Harris C. R., et al., 2020, Nature, 585, 357

Haubois X., et al., 2009, A&A, 508, 923

Hayes J. C., Norman M. L., 2003, ApJS, 147, 197

Hellings P., 1983, Ap&SS, 96, 37

Hinkle K. H., Lebzelter T., Fekel F. C., Straniero O., Joyce R. R., Prato L., Karnath N., Habel N., 2020, ApJ, 904, 143

Hirai R., Podsiadlowski P., Yamada S., 2018, The Astrophysical Journal, 864, 119

Hirai R., Podsiadlowski P., Owocki S. P., Schneider F. R. N., Smith N., 2021, MNRAS, 503, 4276

Hjellming M. S., Webbink R. F., 1987, ApJ, 318, 794

Humphreys R. M., Helton L. A., Jones T. J., 2007, AJ, 133, 2716

Humphreys R. M., Davidson K., Richards A. M. S., Ziurys L. M., Jones T. J., Ishibashi K., 2021, AJ, 161, 98

Humphreys R. M., Richards A. M. S., Davidson K., Singh A. P., Decin L., Ziurys L. M., 2024, AJ, 167, 94

Hunter J. D., 2007, Computing in Science and Engineering, 9, 90

Hut P., 1980a, A&A, 92, 167

Hut P., 1980b, A&A, 92, 167

Iaconi R., De Marco O., Passy J.-C., Staff J., 2018, MNRAS, 477, 2349

Ichimaru S., 1977, ApJ, 214, 840

Idan I., Lasota J. P., Hameury J. M., Shaviv G., 2010, A&A, 519, A117

Inight K., et al., 2021a, arXiv e-prints, p. arXiv:2109.14514

Inight K., Gänsicke B. T., Breedt E., Marsh T. R., Pala A. F., Raddi R., 2021b, Monthly Notices of the Royal Astronomical Society, 504, 2420

Ivanova N., 2018, ApJ, 858, L24

Ivanova N., et al., 2013a, The Astronomy and Astrophysics Review, 21, 59

Ivanova N., Justham S., Avendano Nandez J. L., Lombardi J. C., 2013b, Science, 339, 433

Ivanova N., Justham S., Nandez J. L. A., Lombardi Jr J. C., 2013c, Science, 339, 433

Jacobson-Galán W. V., et al., 2022, ApJ, 924, 15

Jermyn A. S., et al., 2023, ApJS, 265, 15

Jones T. J., Humphreys R. M., Helton L. A., Gui C., Huang X., 2007, AJ, 133, 2730

Kalogera V., 1996, ApJ, 471, 352

Kalogera V., Webbink R. F., 1998, ApJ, 493, 351

Kalomeni B., Nelson L., Rappaport S., Molnar M., Quintin J., Yakut K., 2016, ApJ, 833, 83

Kaminski T., 2019, A&A, 627, A114

Kamiński T., Gottlieb C. A., Young K. H., Menten K. M., Patel N. A., 2013, ApJS, 209, 38

Kára J., Zharikov S., Wolf M., Kučáková H., Cagaš P., Medina Rodriguez A. L., Mašek M., 2021, A&A, 652, A49

Kato T., 2015, Publications of the Astronomical Society of Japan, 67

Kato T., 2021, arXiv e-prints, p. arXiv:2111.07237

Kesseli A. Y., West A. A., Veyette M., Harrison B., Feldman D., Bochanski J. J., 2017, ApJS, 230, 16

King A. R., 2009, MNRAS, 393, L41

Klencki J., Nelemans G., Istrate A. G., Chruslinska M., 2021a, A&A, 645, A54

Klencki J., Nelemans G., Istrate A. G., Chruslinska M., 2021b, A&A, 645, A54

Klencki J., Istrate A., Nelemans G., Pols O., 2022, A&A, 662, A56

Kopal Z., 1955, Annales d'Astrophysique, 18, 379

Kruckow M. U., Tauris T. M., Langer N., Szécsi D., Marchant P., Podsiadlowski P., 2016, A&A, 596, A58

Kuiper G. P., 1941, ApJ, 93, 133

Kukarkin B. V., Parenago P. P., 1934, Var. Star. Bull., 4, 44

Kurfürst P., Pejcha O., Krtička J., 2020, A&A, 642, A214

Lada C. J., Reid M. J., 1978, ApJ, 219, 95

Laibe G., 2014, MNRAS, 437, 3037

Laibe G., Price D. J., 2012, MNRAS, 420, 2345

Laibe G., Price D. J., 2014, MNRAS, 440, 2147

Lamers H. J. G. L. M., Cassinelli J. P., 1999, Introduction to Stellar Winds. Cambridge University Press, https://ui.adsabs.harvard.edu/abs/1999isw..book.....L

Langer N., 2012, Annual Review of Astronomy and Astrophysics, 50, 107

Lara F. E., Rieutord M., 2012, Astronomy & Astrophysics, 547, A32

Lasota J.-P., 2001, New Astronomy Reviews, 45, 449

Lau M. Y. M., Hirai R., González-Bolívar M., Price D. J., De Marco O., Mandel I., 2022, MNRAS, 512, 5462

Laycock S., Tang S., Grindlay J., Los E., Simcoe R., Mink D., 2010, AJ, 140, 1062

Levermore C. D., Pomraning G. C., 1981, ApJ, 248, 321

Lu W., Fuller J., Quataert E., Bonnerot C., 2023, MNRAS, 519, 1409

Lucy L. B., 1971, ApJ, 163, 95

Lucy L. B., 1976, ApJ, 205, 482

Lucy L. B., 1977, AJ, 82, 1013

Lucy L. B., 2005, A&A, 429, 19

MacLeod M., Ostriker E. C., Stone J. M., 2018, The Astrophysical Journal, 868, 136

Maeder A., 1987, A&A, 178, 159

Marchant P., Pappas K. M. W., Gallegos-Garcia M., Berry C. P. L., Taam R. E., Kalogera V., Podsiadlowski P., 2021a, Astronomy and Astrophysics, 650, A107

Marchant P., Pappas K. M. W., Gallegos-Garcia M., Berry C. P. L., Taam R. E., Kalogera V., Podsiadlowski P., 2021b, A&A, 650, A107

Margutti R., et al., 2014, ApJ, 780, 21

Marsh T. R., Horne K., 1988, MNRAS, 235, 269

Mason B. D., Hartkopf W. I., Gies D. R., Henry T. J., Helsel J. W., 2009, The Astronomical Journal, 137, 3358

Massey P., Neugent K. F., Ekström S., Georgy C., Meynet G., 2023, ApJ, 942, 69

Matthews J. H., Knigge C., Long K. S., Sim S. A., Higginbottom N., 2015, MNRAS, 450, 3331

Mel'Nik A. M., Dambis A. K., 2009, MNRAS, 400, 518

Metzger B. D., 2022, ApJ, 932, 84

Meyer F., Meyer-Hofmeister E., 1979, A&A, 78, 167

Meyer F., Meyer-Hofmeister E., 1981, A&A, 104, L10

Mignone A., Bodo G., Massaglia S., Matsakos T., Tesileanu O., Zanni C., Ferrari A., 2007, ApJS, 170, 228

Mineshige S., Osaki Y., 1983, PASJ, 35, 377

Moe M., Di Stefano R., 2017, ApJS, 230, 15

Mohamed S., Podsiadlowski P., 2007, in Napiwotzki R., Burleigh M. R., eds, Astronomical Society of the Pacific Conference Series Vol. 372, 15th European Workshop on White Dwarfs. p. 397

Monaghan J. J., Price D. J., 2006, MNRAS, 365, 991

Montez Jr. R., Kastner J. H., Humphreys R. M., Turok R. L., Davidson K., 2015, ApJ, 800, 4

Morales-Rueda L., Marsh T. R., 2002, MNRAS, 332, 814

Morris J. P., 1996, Publ. Astron. Soc. Australia, 13, 97

Mróz P., et al., 2015, Acta Astron., 65, 313

Nandez J. L. A., Ivanova N., Lombardi J. C. J., 2015, MNRAS, 450, L39

Nelemans G., Verbunt F., Yungelson L. R., Portegies Zwart S. F., 2000, A&A, 360, 1011

Neo S., Miyaji S., Nomoto K., Sugimoto D., 1977, PASJ, 29, 249

Neugent K. F., 2021, ApJ, 908, 87

Neugent K. F., Massey P., Morrell N. I., Skiff B., Georgy C., 2018, AJ, 155, 207

Neugent K. F., Levesque E. M., Massey P., Morrell N. I., 2019, ApJ, 875, 124

Neugent K. F., Levesque E. M., Massey P., Morrell N. I., Drout M. R., 2020, ApJ, 900, 118

Nicholson M., 2009, The Journal of the American Association of Variable Star Observers, 37, 40

Nieuwenhuijzen H., de Jager C., 1990, A&A, 231, 134

Novikov I. D., Thorne K. S., 1973, in Black Holes (Les Astres Occlus). pp 343–450

O'Gorman E., et al., 2015, A&A, 573, L1

Ofek E. O., et al., 2014, ApJ, 789, 104

Ogata M., Hirai R., Hijikawa K., 2021, MNRAS, 505, 2485

Ohlmann S. T., Röpke F. K., Pakmor R., Springel V., 2016, ApJ, 816, L9

Ohlmann S. T., Röpke F. K., Pakmor R., Springel V., 2017, Astronomy and Astrophysics, 599, A5

Otulakowska-Hypka M., Olech A., Patterson J., 2016, Monthly Notices of the Royal Astronomical Society, 460, 2526

Packet W., 1981, Astronomy and Astrophysics, 102, 17

Paczynski B., 1976, Proc. IAU Symp. 73, Structure and Evolution of Close Binary Systems, 73, 75

Passy J.-C., Herwig F., Paxton B., 2012, ApJ, 760, 90

Patrick L. R., et al., 2019, A&A, 624, A129

Patrick L. R., Thilker D., Lennon D. J., Bianchi L., Schootemeijer A., Dorda R., Langer N., Negueruela I., 2022, MNRAS, 513, 5847

Pavlovskii K., Ivanova N., 2015a, MNRAS, 449, 4415

Pavlovskii K., Ivanova N., 2015b, MNRAS, 449, 4415

Paxton B., Bildsten L., Dotter A., Herwig F., Lesaffre P., Timmes F., 2011, ApJS, 192, 3

Paxton B., et al., 2013a, ApJS, 208, 4

Paxton B., et al., 2013b, ApJS, 208, 4

Paxton B., et al., 2015a, The Astrophysical Journal Supplement Series, 220, 15

Paxton B., et al., 2015b, ApJS, 220, 15

Paxton B., et al., 2018a, The Astrophysical Journal Supplement Series, 234, 34

Paxton B., et al., 2018b, ApJS, 234, 34

Paxton B., et al., 2019a, The Astrophysical Journal Supplement Series, 243, 10

Paxton B., et al., 2019b, ApJS, 243, 10

Pejcha O., Metzger B. D., Tomida K., 2016a, MNRAS, 455, 4351

Pejcha O., Metzger B. D., Tomida K., 2016b, MNRAS, 461, 2527

Pejcha O., Metzger B. D., Tyles J. G., Tomida K., 2017, ApJ, 850, 59

Pejcha O., Calderón D., Kurfürst P., 2022, MNRAS, 510, 3276

Pešta M., Pejcha O., 2023, A&A, 672, A176

Podsiadlowski P., Joss P. C., Hsu J. J. L., 1992, The Astrophysical Journal, 391, 246

Powell K. G., 1994, Approximate Riemann solver for magnetohydrodynamics (that works in more than one dimension)

Poznanski D., Prochaska J. X., Bloom J. S., 2012, MNRAS, 426, 1465

Price D. J., 2007, Publ. Astron. Soc. Australia, 24, 159

Price D. J., 2012, Journal of Computational Physics, 231, 759

Price D. J., Laibe G., 2015, MNRAS, 451, 813

Price D. J., et al., 2018, Publ. Astron. Soc. Australia, 35, e031

Prša A., et al., 2016, ApJS, 227, 29

Quintana-Lacaci G., Velilla-Prieto L., Agúndez M., Fonfría J. P., Cernicharo J., Decin L., Castro-Carrizo A., 2023, A&A, 669, A56

Razoumov A. O., Scott D., 1999, MNRAS, 309, 287

Reichardt T. A., De Marco O., Iaconi R., Tout C. A., Price D. J., 2019, MNRAS, 484, 631

Reichardt T. A., De Marco O., Iaconi R., Chamandy L., Price D. J., 2020, MNRAS, 494, 5333

Renzo M., Götberg Y., 2021, The Astrophysical Journal, 923, 277

Renzo M., et al., 2019, A&A, 624, A66

Renzo M., Zapartas E., Justham S., Breivik K., Lau M., Farmer R., Cantiello M., Metzger B. D., 2023, The Astrophysical Journal, 942, L32

Richards A. M. S., et al., 2014, A&A, 572, L9

Ricker P. M., 2008, The Astrophysical Journal Supplement Series, 176, 293

Ricker P. M., Timmes F. X., Taam R. E., Webbink R. F., 2018, Proceedings of the International Astronomical Union, 14, 449

Rieutord M., Espinosa Lara F., Putigny B., 2016, Journal of Computational Physics, 318, 277

Rivera Sandoval L. E., Maccarone T. J., Pichardo Marcano M., 2020, ApJ, 900, L37

Rogers F. J., Swenson F. J., Iglesias C. A., 1996, ApJ, 456, 902

Roulston B. R., Green P. J., Kesseli A. Y., 2020, ApJS, 249, 34

Röpke F. K., De Marco O., 2023, Living Reviews in Computational Astrophysics, 9, 2

Sana H., Evans C. J., 2010, Proceedings of the International Astronomical Union, 6, 474

Sana H., et al., 2012, Science, 337, 444

Sand C., Ohlmann S. T., Schneider F. R. N., Pakmor R., Röpke F. K., 2020, A&A, 644, A60

Schaefer B. E., 2010, ApJS, 187, 275

Schneider F. R. N., Ohlmann S. T., Podsiadlowski P., Röpke F. K., Balbus S. A., Pakmor R., Springel V., 2019, Nature, 574, 211

Schoenberg I. J., 1946, Quarterly of Applied Mathematics, 4, 112

Schwarzschild M., 1975, ApJ, 195, 137

Shakura N. I., Sunyaev R. A., 1973, A&A, 500, 33

Shara M. M., Prialnik D., Hillman Y., Kovetz A., 2018, ApJ, 860, 110

Shenar T., et al., 2020, A&A, 639, L6

Shenoy D., et al., 2016, AJ, 151, 51

Shiber S., Soker N., 2018, MNRAS, 477, 2584

Shiber S., Kashi A., Soker N., 2017, MNRAS, 465, L54

Siess L., Homan W., Toupin S., Price D. J., 2022, A&A, 667, A75

Smak J., 1982, Acta Astron., 32, 199

Smak J., 1983, ApJ, 272, 234

Smak J., 2000, New Astron. Rev., 44, 171

Smith N., 2011, MNRAS, 415, 2020

Smith N., 2014a, ARA&A, 52, 487

Smith N., 2014b, ARA&A, 52, 487

Smith N., Humphreys R. M., Davidson K., Gehrz R. D., Schuster M. T., Krautter J., 2001, AJ, 121, 1111

Soberman G. E., Phinney E. S., van den Heuvel E. P. J., 1997, A&A, 327, 620

Soker N., 2015, ApJ, 800, 114

Soker N., Tylenda R., 2006, MNRAS, 373, 733

Soker N., Grichener A., Sabach E., 2018, ApJ, 863, L14

Springel V., 2010, ARA&A, 48, 391

Springel V., Pakmor R., Zier O., Reinecke M., 2021, MNRAS, 506, 2871

Starrfield S., Iliadis C., Hix W. R., 2016, PASP, 128, 051001

Stone J. M., Tomida K., White C. J., Felker K. G., 2020, ApJS, 249, 4

Suzuki A., Moriya T. J., Takiwaki T., 2019, ApJ, 887, 249

Tauris T. M., van den Heuvel E. P. J., 2006, in , Vol. 39, Compact stellar X-ray sources. Cambridge University Press, pp 623–665, doi:10.48550/arXiv.astro-ph/0303456

Tauris T. M., et al., 2017, ApJ, 846, 170

Telleschi A., Güdel M., Briggs K. R., Audard M., Palla F., 2007, A&A, 468, 425

Temmink K. D., Pols O. R., Justham S., Istrate A. G., Toonen S., 2023, A&A, 669, A45

Teyssier R., 2002, A&A, 385, 337

Theuns T., Jorissen A., 1993, MNRAS, 265, 946

Thorne K. S., 1974, ApJ, 191, 507

Thorne K. S., Zytkow A. N., 1977, ApJ, 212, 832

Timmes F. X., Swesty F. D., 2000, ApJS, 126, 501

Ting Y.-S., Conroy C., Rix H.-W., Cargile P., 2019, ApJ, 879, 69

Tout C. A., Eggleton P. P., 1988, MNRAS, 231, 823

Townsend R. H. D., 2009, ApJS, 181, 391

Townsley D. M., Gänsicke B. T., 2009, ApJ, 693, 1007

Tricco T. S., Price D. J., 2012, Journal of Computational Physics, 231, 7214

Turk M. J., Smith B. D., Oishi J. S., Skory S., Skillman S. W., Abel T., Norman M. L., 2011, The Astrophysical Journal Supplement Series, 192, 9

Tutukov A. V., Yungelson L. R., 1993, MNRAS, 260, 675

Tylenda R., et al., 2011, A&A, 528, A114

Udalski A., Szymański M. K., Szymański G., 2015, Acta Astron., 65, 1

Vacondio R., Rogers B. D., Stansby P. K., Mignosa P., 2016, Computer Methods in Applied Mechanics and Engineering, 300, 442

Van Der Walt S., Colbert S. C., Varoquaux G., 2011, Computing in Science & Engineering, 13, 22

Verbunt F., Phinney E. S., 1995, A&A, 296, 709

Vlasis A., Dessart L., Audit E., 2016, MNRAS, 458, 1253

Vlemmings W. H. T., et al., 2017, A&A, 603, A92

Wadsley J. W., Keller B. W., Quinn T. R., 2017, MNRAS, 471, 2357

Wallerstein G., 1971, ApJ, 169, 195

Walter F., Bond H. E., Pasten A., Otero S., 2006, IAU Circ., 8663, 1

Warner B., 2003a, Cataclysmic Variable Stars, by Brian Warner, pp. 592. ISBN 052154209X. Cambridge, UK: Cambridge University Press, September 2003.

Warner B., 2003b, Cataclysmic Variable Stars, by Brian Warner, pp. 592. ISBN 052154209X. Cambridge, UK: Cambridge University Press, September 2003.

Webbink R. F., 1984, ApJ, 277, 355

Wendland H., 1995, Advances in Computational Mathematics, 4, 389

Wittkowski M., Hauschildt P. H., Arroyo-Torres B., Marcaide J. M., 2012, A&A, 540, L12

Zahn J. P., 1977, A&A, 57, 383

Zhang B., Reid M. J., Menten K. M., Zheng X. W., 2012, ApJ, 744, 23

de Jager C., Nieuwenhuijzen H., van der Hucht K. A., 1988, A&AS, 72, 259

de Mink S. E., Langer N., Izzard R. G., Sana H., de Koter A., 2013, ApJ, 764, 166

van Loon J. T., Cioni M. R. L., Zijlstra A. A., Loup C., 2005, A&A, 438, 273

van den Heuvel E. P. J., 1976, in Structure and Evolution of Close Binary Systems. p. 35

Özel F., Freire P., 2016, ARA&A, 54, 401

List of Figures

List of Tables

List of Abbreviations

1D	One Dimension
3D	Three Dimensions
AGB	Asymptotic giant branch
AMR	Adaptive mesh refinement
AAVSO	American Association of Variable Star Observers
BH	Black hole
CEE	Common envelope evolution
CFL	Courant-Friedrichs-Lewy, stability criterion for timestepping schemes in hydrodynamics codes
CSM	Circumstellar medium
CVs	Cataclysmic variables
DN	Dwarf nova
EoS	Equation of state
FFT	Fast Fourier Transform, algorithm to rapidly compute Fourier transforms.
HE	Hydrostatic equilibrium
IRAF	Image Reduction and Analysis Facility, software for reduction and analysis of astronomical observations.
PHOEBE	PHysics Of Eclipsing BinariEs, eclipsing binary modeling code
JD	Julian Date
MS	Main sequence
MESA	Modules for Experiments in Stellar Astrophysics, 1D stellar evolution code
MHD	Magnetohydrodynamics
NS	Neutron star
PPM	Piecewise parabolic method, scheme for flux reconstruction at cells edges in finite-volume hydrodynamics methods
RHD	Radiative hydrodynamics
RLOF	Roche lobe overflow

RSG	Red supergiant
SED	Spectral Energy Distribution
SN	Supernova
SPH	Smoothed particle hydrodynamics
TE	Thermal equilibrium
UT	Universal time
UV	Ultraviolet
WD	White Dwarf
ZAMS	Zero-age main sequence

List of publications

In chronological order:

The complex dynamical past and future of double eclipsing binary CzeV343: Misaligned orbits and period resonance, Pejcha O., Cagaš P., **Landri C.**, Fausnaugh M., De Rosa G., Prieto J. L., Henzl Z., Pešta M., 2022, Astronomy & Astrophysics, Volume 667

OGLE-BLG504.12.201843: A possible extreme dwarf nova, **Landri C.**, Pejcha O., Pawlak M., Udalski A., Prieto J.L., Barrientos M., Strader J. and Dong S., 2022, MNRAS, Volume 517, Issue 2

Driving asymmetric red supergiants winds with binary interactions, **Landri C.**, Pejcha O., 2024, MNRAS